

Search for Heavy Neutral Leptons with IceCube DeepCore

Dissertation
zur Erlangung des akademischen Grades
doctor rerum naturalium
(Dr. rer. nat.)

im Fach: Physik
Spezialisierung: Experimentalphysik

eingereicht an der
Mathematisch-Naturwissenschaftlichen Fakultät
der Humboldt-Universität zu Berlin

von
Leander Fischer M. Sc.
geboren am 24. Oktober 1992
in Heidelberg

Präsidentin der Humboldt-Universität zu Berlin
Prof. Dr. Julia von Blumenthal

Dekanin der Mathematisch-Naturwissenschaftlichen Fakultät
Prof. Dr. Caren Tischendorf

Copyright Notice

This book is released into the public domain using the CC-BY-4.0 code.

To view a copy of the CC-BY-4.0 code, visit:

<https://creativecommons.org/licenses/by/4.0/>

Colophon

This document was typeset with the help of KOMA-Script and L^AT_EX using the open-source kaobook template class.

The source code of this thesis is available at:

https://github.com/LeanderFischer/phd_thesis

Zusammenfassung

Zusammenfassung ...

Abstract

Abstract ...

Todo list

(Re-)write introduction for PhD thesis (just copy paste from M.Sc.)	1
Also cite this? Didn't find a good reference, only the press releases.	3
Introduce SM EW NC/CC Lagrangian to build upon in the next chapter	5
Plot is missing + for W and 0 for Z boson.	5
Cite and/or sidenote this.	5
cite this	6
cite neutrino oscillations/flavor conversions	6
namedrop RH=sterile=HNL and why they are called like this based on the SM EW Lagrangian introduced above	6
write some interlude to motivate atm. neutrinos as source for HNL searches/production etc.	8
Say something about atmospheric atmospheric neutrino flux uncertainties, based on recent JP/Anatoli papers.	9
SB: It seems that you have some double counting of information here . I suggest to move some of the information in this "intro" paragraph to the appropriate subsections	10
Explain momenta and momentum transfer (p, q) in these figures.	10
SB: formatting/margins also I don't think you defined $\rho_{1,2}$	11
Re-write/re-formulate this section (copied from HNL technote).	12
Produce similar styled plot for these limits	13
This section really needs to be re-written to motivate the search for HNLs from a more generic point of view (e.g. to explain neutrino masses)	13
This section definitely needs to be elaborated in a little more detail	13
Not adding information about the case where the neutrinos have Dirac or pseudo-Dirac masses	14
add fancy icecube picture	17
SB: there are more properties than just these. Somehow need a half sentence that explains why these are particularly important to single out (see ice papers for inspiration)	18
CL: maybe define that absorption and scattering lengths are? they are defined differently so this invites a comparison that is not so obvious	18
Add reference for the dust layer!	18
exchange for figure with scattering (check abs/sca is correct)	18
mention/cite dust logger paper/procedure?	18
Add accuracy of the efficiency calibration here.	19
Maybe throw the coordinate system in a box on the side?	19
Blow up this image a bit, so it's better readable as marginfigure.	19
CL: value?	20

SB: this needs revision. the energy range you mention is particular for oscillations already (atmopsheric neutrinos are plentiful outside of this range you mentioned). If you rewrite the first part you'll have to revisit the second part. Also in general I'd suggest not to rank analyses like Main and Other - DeepCore was orginally intended as a dark matter detector, and there are probably more DM analyses unblinded / year than oscillations. Just keep it general, no need to rank.	20
Cite n and θ_c	20
SB: you already mentioned that Cher. Rad. doesn't lead to significant energy loss. I suggest to clean up the text a bit, you dont' need to emphasize that so many times. Pick one place (probably here) and eliminate it elsewhere	21
Add reference (PDG or find original)	21
SB: i like that you give a benchmark value here, for rule of thumb or so, but it should be related to the detector geometry somehow or else it feels too out of place. Give it some context	21
Add reference for these processes.	22
cite em shower distribution	22
Add angular profile plot (Summer agrees!) (create one based on Leif Rädel as Alex did)	22
SB: rephrase gamma (from equation) is not defined	22
SB: Explain	23
Make sure I have this defined in the SM interaction chapter!	24
SB: Since your analysis depends on the ability to reconstruct cascade directions, it seems odd to emphasize that the light is nearly isotropically emitted. Of course that is true, but the emphasis should rather be on the fact that there remains some assymetry to the light profile	24
Adapt to reflect switched chapter order	25
Make my own DC string positions/distances plot version.	25
Re-make plot with all energies (cascades and total, both sets (they are the same))	26
Re-make plot with all decay lengths (both sets)	26
Re-make plot with 3 target masses and better labels	30
Add comparions of SM cross-sections between NuXSSplMkr and genie?	30
add varied total cross-section for a few background HNL events (for QE/RES variations?!?)	30
Calculate max BRs	30
JVS: consider also writing down the (trivial) 2-body decay kinematics for completeness and consistency. This transition is a bit jarring as it is	31
add table with number of gen level files? mention the event number is smaller becasue of kinematic condition?	33
maybe increase main text width? (read in kao docu)	35
Adapt to reflect switched chapter order	35
put a number on this significant increase?	39
put a number on the tilt angle?	40
Add SPE distribuiton plot	41

AT: Das klingt so, als würde die MC Simulation ein analoges Signal erzeugen, was auch digitalisiert wird. Vllt kann man das nochmal nachforschen, aber zumindest in meiner Arbeit habe ich geschrieben, dass die MCPEs direkt in ATWD und fADC Readouts umgewandelt werden.	41
add example plots (?) for L3 cut variables and applied cuts	43
add some figure showing the corridors?	44
add table with rates per level (split in flavor) - maybe better in analysis chapter to also show signal? . .	44
add image with selected strings used for flercnn IC and DC	45
add some performance plots of the FLERCNN reconstruction	45
There is more information on pre-processing the samples and preparing the input features, and training each cnn, but I'm not sure if that might be too much detail?	45
add reference for flercnn analysis internal note	46
add final sample composition, but maybe also in analysis chapter to show signal and background? . .	47
at some place I will want a selection efficiency plot for SM BG and HNL signal, but I'm not sure where to put it yet	47
add figure with Barr blocks?	48
which experiments measure the axial mass?	49
cite this?	51
add information about the matter profile used	55
add information about the oscillation probability calculation and the software used for it	55
Should I adapt the total numbers to match the sum of the rounded individual parts?	55
add 3D expectation and/or S/sqrt(B) plots	56
Add fractions of the different particle types in the bins for benchmark mass/mixing (another table?) .	56
Do I want/need to include the description of the KDE muon estimation?	57
Add table with all systematic uncertainties used in this analysis (in the analysis chapter).	57
add final level effects of varying the axial mass parameters (or example of one)	57
add final level effects of varying the DIS parameter (or example of one)	57
Do I want additional plots for this (fit diff, LLH distr, minim. stats, param. fits)?	58
Add bin-wise TS distribution? Add 3D TS maps?	59
Write conclusion	63
Re-make plot with x,y for horizontal set one plot!	67
Re-make plot with x, y, z for both cascades in one.	67
Re-arrange plots in a more sensible way.	67

Contents

Abstract	iii
Contents	ix
1 Introduction	1
2 Standard Model Neutrinos and Beyond	3
2.1 The Standard Model	3
2.1.1 Fundamental Fields	3
2.1.2 Electroweak Symmetry Breaking	4
2.1.3 Fermion Masses	5
2.1.4 Weak Interactions after Symmetry-Breaking	5
2.2 Beyond the Standard Model	5
2.2.1 Mass Mechanisms	6
2.2.2 Observational Avenues for right-handed neutrinos	7
2.2.3 Existing Constraints on Heavy Neutral Leptons	7
2.3 Atmospheric Neutrinos as Source of Heavy Neutral Leptons	8
2.3.1 Production of Neutrinos in the Atmosphere	8
2.3.2 Interactions with Nuclei	9
2.3.3 Oscillations	11
2.3.4 Testing Heavy Neutral Leptons with Atmospheric Neutrinos	12
3 The IceCube Neutrino Observatory	17
3.1 Detector Components	17
3.1.1 Digital Optical Modules and the Antarctic Ice	18
3.1.2 IceCube	19
3.1.3 DeepCore	19
3.2 Particle Propagation in Ice	20
3.2.1 Cherenkov Effect	20
3.2.2 Energy Losses	21
3.3 Event Morphologies	23
4 Heavy Neutral Lepton Signal Simulation	25
4.1 Model Independent Simulation	25
4.1.1 Simplistic Sets	25
4.1.2 Realistic Set	26
4.2 Model Dependent Simulation	28
4.2.1 Custom LeptonInjector	28
4.2.2 Sampling Distributions	32
4.2.3 Weighting Scheme	32
4.2.4 Generation Level Distributions	33
5 Standard Model Background Simulation and Data Processing	37
5.1 Event Generation	37
5.1.1 Neutrinos	38
5.1.2 Muons	39
5.2 Detector Simulation	39
5.2.1 Photon Propagation	40
5.2.2 Detector Responses	40
5.3 Processing	41
5.3.1 Trigger and Filter	41

5.3.2	Event Selection	43
5.4	Reconstruction	45
5.4.1	Fast Low Energy Reconstruction using Convolutional Neural Networks	45
5.4.2	Analysis Selection	46
5.5	Systematic Uncertainties	47
5.5.1	Atmospheric Flux Uncertainties	48
5.5.2	Cross-Section Uncertainties	48
5.5.3	Detector Calibration Uncertainties	49
5.5.4	Muon Uncertainties	50
6	Detecting Low Energetic Double Cascades	53
6.1	Reconstruction	53
6.1.1	Table-Based Minimum Likelihood Algorithms	53
6.1.2	Double Cascade Hypothesis	53
6.1.3	Modification to Low Energy Events	53
6.2	Cross Checks	53
6.2.1	Simplistic Sets	53
6.3	Performance	54
6.3.1	Energy/Decay Length Resolution	54
6.3.2	Double Cascade Classification	54
7	Search for an Excess of Heavy Neutral Lepton Events	55
7.1	Final Level Sample	55
7.1.1	Expected Rates/Events	55
7.1.2	Analysis Binning	56
7.2	Statistical Analysis	57
7.2.1	Low Energy Analysis Framework	57
7.2.2	Test Statistic	57
7.2.3	Systematic Uncertainties	57
7.3	Analysis Checks	57
7.3.1	Minimization Robustness	58
7.3.2	Ensemble Tests	58
7.4	Results	59
7.4.1	Best Fit Parameters	59
7.4.2	Upper Limits	59
7.4.3	Post-Fit Data/MC Agreement	59
7.4.4	Likelihood Coverage	59
8	Summary and Outlook	61
8.1	Summary	61
8.1.1	Three-Flavor Oscillation Measurement	61
8.1.2	Heavy Neutral Lepton Search	61
8.2	Outlook	61
8.2.1	Shape Analysis Improvements	61
8.2.2	Test Coupling to Electron/Muon Flavor	61
8.2.3	IceCube Upgrade	61
9	Conclusion	63
APPENDIX		65
A	Heavy Neutral Lepton Signal Simulation	67
A.1	Model Independent Simulation Distributions	67
A.2	Model Dependent Simulation Distributions	68

B Analysis Checks	69
B.1 Minimization Robustness	69
B.1.1 Ensemble Tests	69
Bibliography	71

List of Figures

2.1	Feynman diagrams of neutrino weak interactions	5
2.2	HNL decay widths	8
2.3	Atmospheric neutrino fluxes	8
2.4	Total inclusive neutrino-nucleon cross-sections	9
2.5	Neutrino-nucleon deep inelastic scattering	10
2.6	Current $ U_{\tau 4}^2 - m_4$ limits	12
2.7	Feynman diagram of HNL up-scattering process	14
2.8	Feynman diagram of HNL decay	15
2.9	HNL branching ratios	15
3.1	IceCube overview	17
3.2	IceCube sideview	18
3.3	Digital Optical Module (DOM)	19
3.4	IceCube top view	19
3.5	Cherenkov light front	20
4.1	DeepCore string spacing	26
4.2	Simplified model independent simulation generation level distributions	27
4.3	Realistic model independent simulation generation level distributions	28
4.4	HNL branching ratios	29
4.5	Custom HNL total cross-sections for the four target masses compared to the total ($\nu_\tau/\bar{\nu}_\tau$ NC) cross-section used for SM neutrino simulation production with GENIE.	30
4.6	Model dependent simulation generation level distributions	34
5.1	Depth dependent scattering and absorption lengths	40
5.2	IceCube trigger efficiencies	42
5.3	Level 4 classifier outputs (muon and noise)	44
5.4	FLERCNN architecture	46
5.5	FLERCNN muon classifier probability distributions	47
5.6	Inclusive total neutrino-nucleon cross-sections	50
5.7	Hole ice angular acceptance modification	51
7.1	Asimov inject/recover test (0.6 GeV)	58
7.2	Pseudo-data trials TS distribution (0.6 GeV)	59
A.1	Simplified model independent simulation generation level distributions	67
A.2	Realistic model independent simulation generation level distributions	68
A.3	Model dependent simulation generation level distributions	68
B.1	Asimov inject/recover test (0.3 GeV, 1.0 GeV)	69
B.2	Pseudo-data trials TS distribution (0.3 GeV, 1.0 GeV)	69

List of Tables

2.1 Standard model fermions	4
3.1 IceCube low energy event signatures and underlying interactions	23
4.1 Simplified model independent simulation sampling distributions	27
4.2 Realistic model independent simulation sampling distributions	28
4.3 HNL mass dependent decay channels	30
4.4 Model dependent simulation sampling distributions	32
5.1 GENIE generation cylinder volumes	38
5.2 Vuvuzela noise simulation parameters	41
5.3 Final analysis cuts	47
7.1 Final level background event/rate expectation	55
7.2 Final level signal event/rate expectation	56
7.3 Analysis binning	56
7.4 Staged minimization routine settings	58

1

Introduction

notes for the introduction

- ▶ unexplained origin of neutrino masses
- ▶ novel neutrino mass

The neutrino was postulated by Wolfgang Pauli [1] in 1930 to explain the continuous energy spectrum of electrons originating from beta decay. Cowan and Reines confirmed this prediction of a light, neutral particle in 1956 when they discovered the electron neutrino using inverse beta decay [2]. Two additional neutrino flavors were found in the following years, and with the discovery of the muon neutrino in 1962 [3] and the tau neutrino in 2001 [4], the current theory of neutrinos in the standard model (SM) was established.

Although neutrinos were first believed to be massless, experimental evidence showing the existence of mixed neutrino states started to appear in the 1960s [5]. Mixing between different physical representations of neutrinos is proof for differences in their masses. The resulting phenomenon of neutrino oscillations can be incorporated into the standard model by extending it to include massive neutrinos. How massive they are and how strong is the mixing between neutrino states has to be obtained from measurement. Today there are a variety of precision oscillation experiments using solar, reactor and atmospheric neutrinos to tighten the constraints on the neutrino oscillation parameters. IceCube is one of those leading experiments probing the oscillation theory with atmospheric neutrinos.

The IceCube Neutrino Observatory [6] was constructed between 2004 and 2010 at the geographic South Pole. It is the first cubic kilometer Cherenkov neutrino detector and consists of 5160 optical sensors attached to 86 strings, drilled down to a maximum depth of ~ 2500 m into the Antarctic ice. Neutrinos are detected by the Cherenkov light that is emitted by secondary particles produced in neutrino-nucleon scattering interactions in the ice. With DeepCore, a more densely instrumented sub-array of IceCube, the neutrino detection energy threshold can be lowered to approximately 5 GeV.

At these energies, the similarity in event signatures poses difficulties in identifying different neutrino flavor interactions. Muon neutrino charged-current interactions produce light tracks as opposed to charged-current interactions of electron and tau neutrinos as well as neutral-current interactions of all neutrinos that produce light cascades. The sparse instrumentation of IceCube makes it more challenging to separate track- and cascade-like events. In this thesis, a novel method to distinguish those two event types is developed. In contrast to previously used univariate separation techniques, the multivariate machine learning method applied here maximizes the use of information from the detector response. Through the use of a Gradient Tree Boosting algorithm the separation of events in track and cascade is improved. As a result of

(Re-)write introduction for
PhD thesis (just copy paste
from M.Sc.).

[1]: Pauli (1978), "Dear radioactive ladies and gentlemen"

[2]: Cowan et al. (1956), "Detection of the Free Neutrino: a Confirmation"

[3]: Danby et al. (1962), "Observation of High-Energy Neutrino Reactions and the Existence of Two Kinds of Neutrinos"

[4]: Kodama et al. (2001), "Observation of tau neutrino interactions"

[5]: Davis et al. (1972), *Proceedings of the Neutrino '72 Europhysics Conference*

[6]: Aartsen et al. (2017), "The IceCube Neutrino Observatory: instrumentation and online systems"

the improved separation, the uncertainty to the atmospheric neutrino oscillation parameters Δm_{32}^2 and θ_{23} is significantly reduced.

This thesis is structured as follows.

Standard Model Neutrinos and Beyond

2

2.1 The Standard Model

The *Standard Model (SM)* of particle physics is a Yang-Mills theory [7] providing very accurate predictions of weak, strong, and *electromagnetic (EM)* interactions. It is a relativistic quantum field theory that relies on gauge invariance, where all matter is made up of fermions, which are divided into quarks and leptons, and bosons describe the interactions between the fermions that have to fulfil the overall symmetry of the theory. Leptons are excitations of Dirac-type fermion fields.

The initial idea of the theory is associated with the works of Weinberg [8], Glashow [9], and Salam [10], that proposed a unified description of EM and weak interactions as a theory of a spontaneously broken $SU(2) \times U(1)$ symmetry for leptons, predicting a neutral massive vector boson Z^0 , a massive charged vector boson W^\pm , and a massless photon γ as the gauge bosons. The Higgs mechanism [11], describing the breaking of the symmetry, predicts the existence of an additional scalar particle, the Higgs boson, giving the W^\pm and Z^0 bosons their mass. The Higgs boson was discovered in 2012 at the LHC.

Gell-Mann and Zweig proposed the quark model in 1964 [12, 13], which was completed by the discovery of non-abelian gauge theories [14] to form the $SU(3)$ symmetry of the strong interaction called *quantum chromodynamics (QCD)*. QCD describes the interaction between quarks and gluons which completed the full picture of the SM in the mid-1970s. Together with the electroweak theory, the SM is a $SU(3)_C \times SU(2)_L \times U(1)_Y$ local gauge symmetry, with the conserved quantities C , *color*, L , *left-handed chirality*, and Y , *weak hypercharge*.

In the following, the basic properties of the SM are described, following the derivations of [15, 16].

2.1.1 Fundamental Fields

Fermions in the SM are Weyl fields with either *left-handed (LH)* or *right-handed (RH)* chirality, meaning they are eigenvectors of the chirality operator γ_5 with $\gamma_5 \psi_{R/L} = \pm \psi_{R/L}$. Only LH particles transform under $SU(2)_L$. The Higgs field is a complex scalar field, a doublet of $SU(2)_L$, which is responsible for the spontaneous symmetry breaking of $SU(2)_L \times U(1)_Y$ to $U(1)_{\text{EM}}$. Local gauge transformations of the fields are given by

$$\psi \rightarrow e^{ig\theta^a(x)T^a} \psi , \quad (2.1)$$

where g is the coupling constant, $\theta^a(x)$ are the parameters of the transformation, and T^a are the generators of the group, with a counting them. The number of bosons is dependent on the generators of the symmetry groups, while the strength is defined by the coupling constants. There are eight massless gluons corresponding to the generators of the $SU(3)_C$

2.1 The Standard Model	3
2.2 Beyond the Standard Model	5
2.3 Atmospheric Neutrinos as Source of Heavy Neutral Leptons	8

[7]: Yang et al. (1954), "Conservation of Isotopic Spin and Isotopic Gauge Invariance"

[8]: Weinberg (1967), "A Model of Leptons"

[9]: Glashow (1961), "Partial-symmetries of weak interactions"

[11]: Higgs (1964), "Broken symmetries, massless particles and gauge fields"

Also cite this? Didn't find a good reference, only the press releases.

[12]: Gell-Mann (1964), "A Schematic Model of Baryons and Mesons"

[13]: Zweig (1964), "An $SU(3)$ model for strong interaction symmetry and its breaking. Version 2"

[15]: Giunti et al. (2007), *Fundamentals of Neutrino Physics and Astrophysics*

[16]: Schwartz (2013), *Quantum Field Theory and the Standard Model*

group. These mediate the strong force which conserves color charge. The W_1, W_2, W_3 , and B boson fields of the $SU(2)_L \times U(1)_Y$ group are mixed into the massive bosons through spontaneous symmetry breaking as

$$W^\pm = \frac{1}{\sqrt{2}}(W_1 \mp iW_2) \quad (2.2)$$

and

$$Z^0 = \cos \theta_W W_3 - \sin \theta_W B, \quad (2.3)$$

with θ_W being the *Weinberg angle*. The massless photon field is given by

$$A = \sin \theta_W W_3 + \cos \theta_W B \quad (2.4)$$

and its conserved quantity is the EM charge Q , which depends on the weak hypercharge, Y , and the third component of the weak isospin, T_3 , as $Q = T_3 + Y/2$.

	Type			Q
quarks	u	c	t	+2/3
	d	s	b	-1/3
leptons	ν_e	ν_μ	ν_τ	0
	e	μ	τ	-1

Table 2.1: Fermions in the Standard Model. Shown are all three generations of quarks and leptons with their electric charge Q .

Fermions are divided into six quarks and six leptons. Weak, strong, and EM force act on the quarks, and they are always found in bound form as baryons or mesons. Leptons do not participate in the strong interaction and only the electrically charged leptons are massive and are effected by the EM force, while neutrinos are massless and only interact via the weak force. Each charged lepton has an associated neutrino, which it interacts with in *charged-current (CC)* weak interactions, that will be explained in more detail in Section 2.1.4. The fermions are listed in Table 2.1.

2.1.2 Electroweak Symmetry Breaking

To elaborate the process of spontaneous symmetry breaking through which the gauge bosons of the weak interaction acquire their masses, the Lagrangian of the Higgs field is considered as

$$\mathcal{L}_{\text{Higgs}} = (D_\mu \Phi^\dagger)(D^\mu \Phi) - \lambda \left(\Phi^\dagger \Phi - \frac{v^2}{2} \right)^2, \quad (2.5)$$

with parameters λ and v , where λ is assumed to be positive. Φ is the Higgs doublet, which is defined as

$$\Phi = \begin{pmatrix} \Phi^+ \\ \Phi^0 \end{pmatrix}, \quad (2.6)$$

with the charged component Φ^+ and the neutral component Φ^0 . The covariant derivative is given by

$$D_\mu = \partial_\mu - ig_2 \frac{\sigma^i}{2} W_\mu^i - \frac{1}{2}ig_1 B_\mu, \quad (2.7)$$

with the Pauli matrices σ^i and the gauge boson fields W_μ^i and B_μ of the $SU(2)_L$ and $U(1)_Y$ groups, respectively. The coupling constants g_2 and g_1 are the respective coupling constants which are related to the Weinberg angle as $\tan \theta_W = \frac{g_1}{g_2}$. The Higgs potential has a non-zero *vacuum expectation value (vev)* at the minimum of the potential at $\Phi^\dagger \Phi = \frac{v^2}{2}$. Since the vacuum is electrically neutral, it can only come from a neutral

component of the Higgs doublet as

$$\Phi_{\text{vev}} = \frac{1}{\sqrt{2}} \begin{pmatrix} 0 \\ v \end{pmatrix}. \quad (2.8)$$

2.1.3 Fermion Masses

The mass term for charged fermions with spin-1/2 is given by

$$\mathcal{L}_{\text{Dirac}} = m(\bar{\Psi}_R \Psi_L - \bar{\Psi}_L \Psi_R), \quad (2.9)$$

composed of the product of left- and RH Weyl spinors $\Psi_{L/R}$. This term is not invariant under $SU(2)_L \times U(1)_Y$ gauge transformations, but adding a Yukawa term

$$\mathcal{L}_{\text{Yukawa}} = -y \bar{L}_L \Phi e_R + h.c., \quad (2.10)$$

coupling the fermion fields to the Higgs field, recovers the invariance and gives the fermions their masses. Here, y is the Yukawa coupling constant and \bar{L}_L is the $SU(2)_L$ doublet. With the vev, this results in the mass term for the charged leptons and down-type quarks of $-m_e(\bar{e}_L e_R + \bar{e}_R e_L)$ with $m_e = \frac{yv}{\sqrt{2}}$. With $\tilde{\Phi} = i\sigma_2 \Phi^*$, a similar Yukawa term can be written as $-y \bar{L}_L \tilde{\Phi} u_R + h.c.$, which leads to the masses of the up-type quarks.

2.1.4 Weak Interactions after Symmetry-Breaking

Stuff from my MSc thesis to re-write:

In the SM, weak interactions are mediated by the three massive bosons W^+ , W^- , and Z^0 [18]. The large boson masses ($m_W \sim 80 \text{ GeV}$, $m_Z \sim 90 \text{ GeV}$) result in a short range of the force of about $10 \times 10^{-18} \text{ m}$. Weak interactions carried by W^\pm bosons are called CC interactions, because charge is transferred between the interacting particles. In CC interactions, a neutrino is converted into its corresponding charged lepton or vice versa. Neutral current (NC) interactions are those mediated by Z^0 bosons. Here no charge is transferred. The Feynman diagrams for CC and NC interactions are shown in Figure 2.1.

The observed phenomenon of neutrino oscillations (see Section 2.3.3) is based on the fact that there is a mass difference between the three neutrino mass eigenstates.

Introduce SM EW NC/CC Lagrangian to build upon in the next chapter

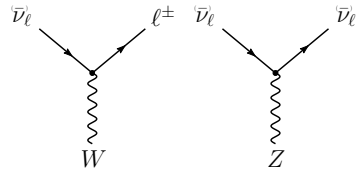


Figure 2.1: Feynman diagrams of charged-current (left) and neutral-current (right) neutrino weak interactions, taken from [17].

Plot is missing + for W and 0 for Z boson.

[18]: Thomson (2013), *Modern particle physics*

2.2 Beyond the Standard Model

Are the fundamentals of the SM described above enough to explain *all* observed phenomena? Gravity cannot be explained by the SM, as it is incompatible with general relativity. Neither can the SM explain some cosmological observations like dark matter, and the matter-antimatter asymmetry, and it does not predict neutrinos to have mass, which is experimentally proven by neutrino oscillations, so some extensions to the SM is needed in order to explain them.

Standard cosmology (Λ CDM) assumes that equal amounts of matter and anti-matter were produced in the early universe. However, the universe

Cite and/or sidenote this.

today is dominantly made up of matter. This so-called *baryon asymmetry* can be measured by the difference between the number densities of baryons and anti-baryons normalized to the number density of photons as

$$\eta_B = \frac{n_B - n_{\bar{B}}}{n_\gamma} , \quad (2.11)$$

where n_B , $n_{\bar{B}}$, and n_γ are the number densities of baryons, anti-baryons, and photons, respectively. Baryons are the dominant component with η_B being observed to be around 6×10^{-10} . Leptogenesis and EW baryogenesis are scenarios that could explain this phenomenon, where the former could be realized by the existence of heavy RH neutrinos.

cite this

cite neutrino oscillations/flavor conversions

The observation of neutrino flavor conversions and neutrino oscillations in a multitude of experiments is the strongest evidence for physics beyond the SM. The observation that neutrinos change their flavor while they propagate through space can only be explained, if at least two neutrinos have a non-zero mass. From the measurements and cosmological observations, we know that the masses are very small as compared to the lepton masses. Neither their existence, nor their smallness is not predicted by the SM, but adding additional RH neutrinos states to the theory could explain the origin of the observed non-zero neutrino masses and could be tested for by searching for corresponding signatures in experiments. But the addition of RH neutrino fields is not the only possible explanation for neutrino masses. Radiative neutrino mass mechanisms could also explain their origin and their smallness, but those would need the introduction of additional symmetries to the theory.

Maybe also add this somehow: "From neutrino oscillation measurements the absolute mass scale cannot be determined, since they only depend on the mass differences, but there are upper limits on the sum of all neutrino masses from cosmological observations. These upper limits are typically between 0.3 and 1.3 eV [19]."

[19]: Tanabashi et al. (2018), "Review of Particle Physics"

namedrop RH=sterile=HNL and why they are called like this based on the SM EW Lagrangian introduced above

2.2.1 Mass Mechanisms

There are no RH neutrinos in the SM and therefore the mass mechanism described in Section 2.1.3, which couples the Higgs field to LH and RH Weyl fields, predicts them to be massless. From experimental observations it is known that at least two of the three neutrino generations need to have a non-zero mass. Assuming the existence of RH neutrino fields ν_R , one way of producing the neutrino masses is by adding a Yukawa coupling term similar to the one for up-type quarks mentioned in Section 2.1.3, to write the full Yukawa Lagrangian as

$$\mathcal{L}_{\text{Yukawa}} = -Y_{ij}^e \bar{L}_L^i \Phi e_R^j - Y_{ij}^\nu \bar{L}_L^i \tilde{\Phi} \nu_R^j + h.c. , \quad (2.12)$$

with i, j running over the three generations of leptons e , μ , and τ , and Y^e and Y^ν being the Yukawa coupling matrices. Diagonalizing the Yukawa coupling matrices through unitary transformations U^e and U^ν leads to the **Dirac mass term** in the mass basis as

$$\mathcal{L}_{\text{Dirac}}^{\text{mass}} = \frac{v}{\sqrt{2}} (\bar{e}_L M_e e_R - \bar{\nu}_L M_\nu \nu_R) , \quad (2.13)$$

where M_e and M_ν are the diagonal mass matrices of leptons and neutrinos, respectively. A purely Dirac mass term would not explain the smallness of the neutrino masses in a straightforward way. Only fine-tuning the Yukawa coupling constants to small values would lead to small neutrino masses.

An additional way of generating neutrino masses is by adding a Majorana mass term of the form

$$\mathcal{L}_{\text{Majorana}} = -\frac{1}{2} M_{ij} (\nu_R^i)^c \nu_R^j + h.c. , \quad (2.14)$$

with M_{ij} being the Majorana mass matrix and the indices i, j running over all N_R RH neutrino generations. The superscript c denotes the charge conjugate field. Combining the charge conjugated RH neutrino fields with the LH neutrino fields as

$$\mathbf{N} = \begin{pmatrix} \boldsymbol{\nu}_L \\ \boldsymbol{\nu}_R^c \end{pmatrix} , \quad (2.15)$$

with $\boldsymbol{\nu}_R$ containing the N_R RH fields. The full neutrino mass Lagrangian is then given by the combined **Dirac and Majorana mass term** as

$$\mathcal{L}_{\text{Dirac+Majorana}}^{\text{mass},\nu} = \frac{1}{2} \mathbf{N}^T \hat{C} M^{\text{D+M}} \mathbf{N} + h.c. , \quad (2.16)$$

and the mass matrix is given by

$$M^{\text{D+M}} = \begin{pmatrix} 0 & (M^D)^T \\ M^D & M^R \end{pmatrix} . \quad (2.17)$$

On top of explaining the origin of neutrino masses itself, a combined Dirac and Majorana mass term could also solve the question of their smallness. If the mass of the RH neutrinos is very large, the masses of the active neutrino flavors is suppressed, which is known as *see-saw mechanism*.

2.2.2 Observational Avenues for right-handed neutrinos

- ▶ oscillations searches for light steriles
- ▶ potential searches for heavy steriles

2.2.3 Existing Constraints on Heavy Neutral Leptons

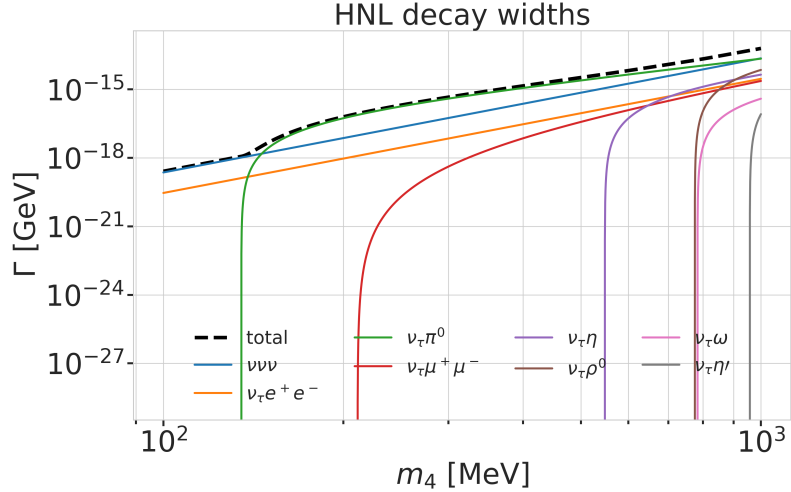


Figure 2.2: Decay widths of the HNL within the mass range considered, calculated based on the results from [20]. Given the existing constraints on $|U_{e4}|^2$ and $|U_{\mu 4}|^2$, we consider that the corresponding decay modes are negligible.

2.3 Atmospheric Neutrinos as Source of Heavy Neutral Leptons

write some interlude to motivate atm. neutrinos as source for HNL searches/production etc.

[19]: Tanabashi et al. (2018), “Review of Particle Physics”

2.3.1 Production of Neutrinos in the Atmosphere

The analysis performed in this work is based on the sample of neutrinos observed in IceCube DeepCore at energies below 100 GeV. At these energies, the flux exclusively originates in the Earth’s atmosphere. Highly relativistic cosmic rays (protons and heavier nuclei [19]) interact in the upper atmosphere, producing showers of secondary particles. Neutrinos are produced in decays of charged pions and kaons (π and K mesons) present in those showers, where the dominant contribution comes from the decay chain

$$\begin{aligned} \pi^\pm &\rightarrow \mu^\pm + \nu_\mu (\bar{\nu}_\mu) , \\ \mu^\pm &\rightarrow e^\pm + \bar{\nu}_\mu (\nu_\mu) + \nu_e (\bar{\nu}_e) , \end{aligned} \quad (2.18)$$

where muon neutrinos ν_μ and muons μ^\pm are produced in the first decay and both electron and muon neutrinos $\nu_{e/\mu}$ are produced in the second decay. Atmospheric muons, which are also produced in these decays, are the main background component for IceCube DeepCore analyses.

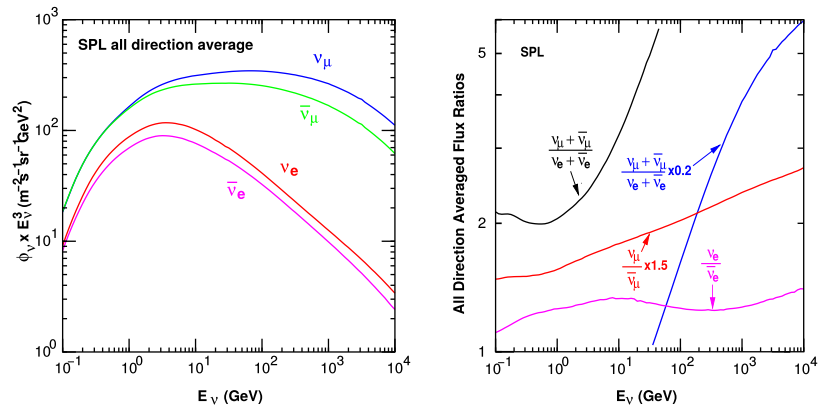


Figure 2.3: The atmospheric fluxes of different neutrino flavors as a function of energy (left) and the ratios between muon neutrinos and electron neutrinos as well as the ratios between neutrinos and antineutrinos for both those flavors (right). Results from the calculations performed for the geographic South Pole, taken from [21].

The different atmospheric flux components are shown in Figure 2.3 (left), for a much broader energy range than relevant for this work. Both neutrinos and antineutrino fluxes are shown for electron and muon neutrinos and all fluxes are the directionally averaged expectation calculated at the South Pole. Muon neutrinos are dominating the flux and from Equation 2.18 the naive assumption would be that the ratio between muon and electron neutrinos is $(\nu_\mu + \bar{\nu}_\mu)/(\nu_e + \bar{\nu}_e) = 2$. This is roughly true at energies below 1 GeV, where all muons decay in flight, but at larger energies muons can reach the detector before decaying, which increases the ratio to approximately 10:1 at around 100 GeV. Additionally, kaon decays start to contribute which also increases the number of muons and muon neutrinos. The increasing ratio can be seen in Figure 2.3 (right), which also shows the ratio between neutrinos and antineutrinos for both flavors.

Charged mesons or tau particles can also be produced in cosmic ray interactions. Their decays lead to the production of tau neutrinos. At the energies relevant for this work however, the resulting tau neutrino flux is negligible as compared to the muon neutrino flux [22] and is not considered in the analysis. This is because both charged mesons and tau particles are much heavier than pions and kaons and therefore their production is suppressed at high energies.

2.3.2 Interactions with Nuclei

To describe the neutrino detection principle of IceCube explained in Chapter 3 we need to understand the weak interaction processes that occur at the energies relevant for this work 10 GeV-100 GeV. The cross-sections are dominated by the following neutrino-nucleon interactions: quasi-elastic scattering (QE), resonant scattering (RES), and deep inelastic scattering (DIS). The relative importance of the different processes depends on energy as can be seen in Figure 2.4.

[22]: Fedynitch et al. (2015), "Calculation of conventional and prompt lepton fluxes at very high energy"

Say something about atmospheric atmospheric neutrino flux uncertainties, based on recent JP/Anatoli papers.

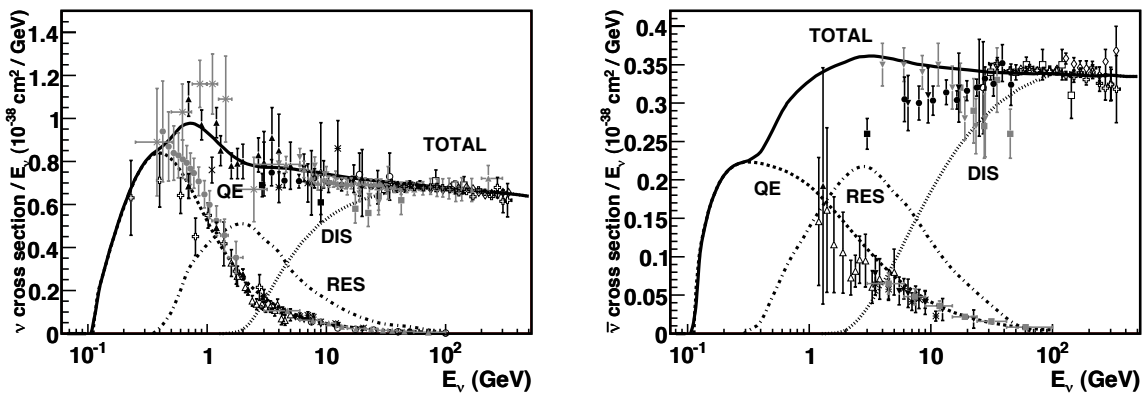


Figure 2.4: Total neutrino(left) and antineutrino(right) per nucleon cross-section divided by neutrino energy plotted against energy. The three main scattering processes quasi-elastic scattering (QE), resonant scattering (RES), and deep-inelastic scattering (DIS) are depicted. Taken from [23].

At energies below 5 GeV, QE and RES occur and the neutrinos interact with approximately point-like protons and neutrons. The cross-sections of these processes are not linear in energy and the transition region to higher energies is poorly understood. At higher energies, the interactions are dominated solely by DIS which has a linear dependence on energy

SB: It seems that you have some double counting of information here . I suggest to move some of the information in this "intro" paragraph to the appropriate subsections

above ~ 20 GeV. For a given neutrino energy, it is possible to predict the cross-section in this region. Here neutrinos interact with a single quark, breaking apart the nucleus and producing a shower of relativistic secondary particles. Neutrino DIS is the primary detection channel of IceCube. From Figure 2.4 it can be seen that the interaction cross-sections are very small of the order of 10^{-38} cm 2 . Because of the small interaction cross-section, very large volume detectors are required to capture a sufficiently large sample of neutrinos to use for precision studies of their properties. For example, the interaction length of a neutrino with $E_\nu = 10$ GeV is of $\mathcal{O}(10^{10})$ km.

Quasi-elastic scattering (QE) with nucleons is the main process below 1 GeV. Protons are converted to neutrons in antineutrino interactions and vice-versa for neutrino interactions. Additionally, a charged lepton corresponding to the neutrino/antineutrino flavor is produced.

Resonant scattering (RES) describes the process of a neutrino scattering off a nucleon producing an excited state of the nucleon in addition to a charged lepton. RES is the leading process at 1.5×10^{-5} GeV for neutrinos and 1.5×10^{-8} GeV for antineutrinos.

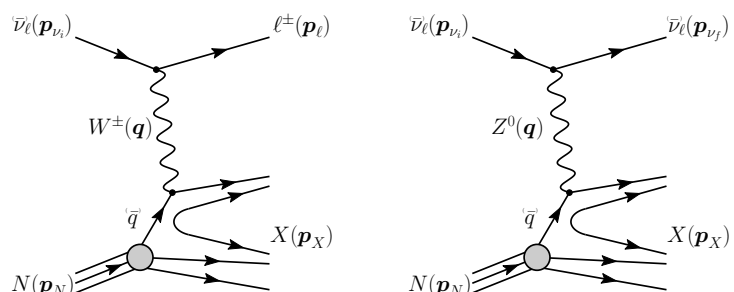
Deep inelastic scattering (DIS) occurs if a neutrino carries sufficient energy to resolve the underlying structure of the nucleon and interacts with one of the composing quarks. DIS is the dominant process above 10 GeV. The nucleon breaks up and a lepton accompanied by a set of hadronic final states is produced. Whether the lepton is the charged lepton corresponding to the interacting neutrino type, or the neutrino itself depends on the type of DIS interaction. DIS happens via CC as in

$$\begin{aligned} \nu_l + N &\rightarrow l^- + X, \\ \bar{\nu}_l + N &\rightarrow l^+ + X, \end{aligned} \quad (2.19)$$

or NC interactions as

$$\nu_l + N \rightarrow \nu_l + X. \quad (2.20)$$

Here, X stands for any set of final state hadrons and N for the nucleon. The Feynman diagrams for the processes in Equation 2.19 and Equation 2.20 are shown in Figure 2.5.



Explain momenta and momentum transfer (q^2) in these figures; charged-current (left) and neutral current (right) interactions.
Taken from [17].

2.3.3 Oscillations

There are two ways to describe neutrino wave functions based on their Hamiltonian eigenvalues [24], as mass eigenstates or as flavor eigenstates. When applying a plane wave approach to explain the propagation of neutrinos in vacuum, their mass eigenstates evolve as

$$|\nu_k(t)\rangle = e^{-iE_k t/\hbar} |\nu_k\rangle, \quad (2.21)$$

where $E_k = \sqrt{\vec{p}^2 c^2 + m_k^2 c^4}$ is the energy of the mass eigenstate $|\nu_k\rangle$, with momentum \vec{p} and mass m_k . Alternatively, they can be described in terms of their flavor eigenstates, which relate the neutrinos to the charged leptons they interact with in weak CC interactions. The flavor eigenstates are ν_e , ν_μ , and ν_τ , whereas the mass eigenstates are called ν_1 , ν_2 , and ν_3 in the standard three-neutrino model. To understand the propagation of distinct neutrino flavors in time we need to relate the flavor eigenstates to the mass eigenstates. For massive neutrinos, each flavor eigenstate is a superposition of mass eigenstates [19]

$$|\nu_\alpha\rangle = \sum_k U_{\alpha k}^* |\nu_k\rangle, \quad (2.22)$$

where $|\nu_\alpha\rangle$ are the weak flavor states with $\alpha = e, \mu, \tau$ and $|\nu_k\rangle$ the mass states with $k = 1, 2, 3$. $U_{\alpha k}$ is the Pontecorvo-Maki-Nakagawa-Sakata (PMNS) matrix defining the mixing between mass and flavor eigenstates. The mixing matrix can be parameterized as [19]

$$U = \begin{pmatrix} 1 & 0 & 0 \\ 0 & c_{23} & s_{23} \\ 0 & -s_{23} & c_{23} \end{pmatrix} \begin{pmatrix} c_{13} & 0 & s_{13} e^{-i\delta_{CP}} \\ 0 & 1 & 0 \\ -s_{13} e^{i\delta_{CP}} & 0 & c_{13} \end{pmatrix} \begin{pmatrix} c_{12} & s_{12} & 0 \\ -s_{12} & c_{12} & 0 \\ 0 & 0 & 1 \end{pmatrix} \text{diag}(e^{i\rho_1}, e^{i\rho_2}, 1), \quad (2.23)$$

where $c_{ij} = \cos \theta_{ij}$ and $s_{ij} = \sin \theta_{ij}$ are cosine and sine of the mixing angle θ_{ij} , that defines the strength of the mixing between the mass eigenstates i and j and δ_{CP} is the neutrino CP-violating phase. Nonzero, non-equal neutrino masses and the neutrino mixing relation in Equation 2.22 lead to the observed phenomenon of neutrino oscillations. Oscillation means that a neutrino changes from its initial flavor to another flavor and back after traveling a certain distance. A produced flavor eigenstate $|\nu_\alpha\rangle$ propagates through space as a superposition of mass eigenstates. To find the probability that the initial flavor state $|\nu_\alpha\rangle$ ends up as the final flavor state $|\nu_\beta\rangle$ after the time t we calculate

$$P_{\nu_\alpha \rightarrow \nu_\beta}(t) = |\langle \nu_\beta | \nu_\alpha(t) | \nu_\beta \rangle|^2, \quad (2.24)$$

where P is the probability calculated by applying Fermi's Golden Rule [25]. Fermi's Golden Rule explains the transition rate from one energy eigenstate to another depending on the strength of the coupling between the two. The strength of the coupling is described by the square of the matrix element. Using the unitarity of the mixing matrix $U^{-1} = U^\dagger$ to reverse the relation Equation 2.22 and then time evolve the mass eigenstates with Equation 2.21 we get the time evolution of the flavor state $|\nu_\alpha(t)\rangle$. Inserting this result into Equation 2.24 yields

$$P_{\nu_\alpha \rightarrow \nu_\beta}(t) = \sum_{j,k} U_{\beta j}^* U_{\alpha j} U_{\beta k} U_{\alpha k}^* e^{-i(E_k - E_j)t/\hbar}, \quad (2.25)$$

[24]: Bilenky et al. (1978), "Lepton mixing and neutrino oscillations"

[19]: Tanabashi et al. (2018), "Review of Particle Physics"

[19]: Tanabashi et al. (2018), "Review of Particle Physics"

SB: formatting/margins also
I don't think you defined
rho1,2

[25]: Dirac (1927), "The Quantum Theory of the Emission and Absorption of Radiation"

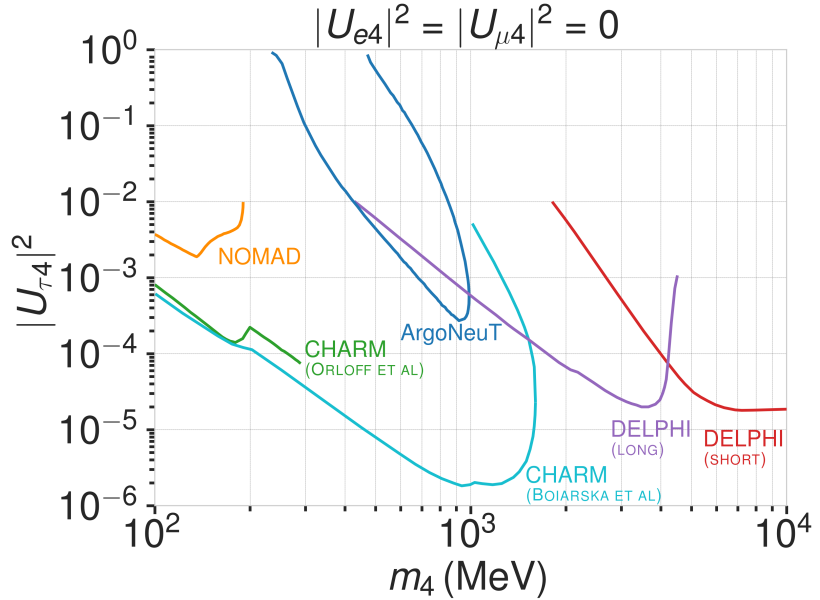


Figure 2.6: Current $|U_{\tau 4}^2| - m_4$ limits from NOMAD [27], ArgoNeut [28], CHARM [29, 30], and DELPHI [31].

where the indices j and k run over the mass eigenstates. For small neutrino masses compared to their kinetic energy, we can approximate the energy as

$$E_k \approx E + \frac{c^4 m_k^2}{2E} \quad \rightarrow \quad E_k - E_j \approx \frac{c^4 \Delta m_{kj}^2}{2E}, \quad (2.26)$$

where $\Delta m_{kj}^2 = m_k^2 - m_j^2$ is the mass-squared splitting between states k and j . If we now replace the time in Equation 2.25 by the distance traveled by the relativistic neutrinos $t \approx L/c$ we get

$$\begin{aligned} P_{\nu_\alpha \rightarrow \nu_\beta}(t) &= \delta_{\alpha\beta} - 4 \sum_{j>k} \text{Re}(U_{\beta j}^* U_{\alpha j} U_{\beta k} U_{\alpha k}^*) \sin^2 \left(\frac{c^3 \Delta m_{kj}^2}{4E\hbar} L \right) \\ &\quad + 2 \sum_{j>k} \text{Im}(U_{\beta j}^* U_{\alpha j} U_{\beta k} U_{\alpha k}^*) \sin^2 \left(\frac{c^3 \Delta m_{kj}^2}{4E\hbar} L \right), \end{aligned} \quad (2.27)$$

which is referred to as the survival probability if $\alpha = \beta$ and the transition probability if $\alpha \neq \beta$. The probability in Equation 2.27 is only nonzero if there are neutrino mass eigenstates with masses greater than zero. Additionally, there must be a mass-squared difference Δm^2 and nonzero mixing between the states. Since we assumed propagation in vacuum in Equation 2.21, the transition and survival probabilities correspond to vacuum mixing.

2.3.4 Testing Heavy Neutral Leptons with Atmospheric Neutrinos

The Minimal Standard Model Extension

Re-write/re-formulate this section (copied from HNL technote).

Extensions to the Standard Model (SM) that add *Heavy Neutral Leptons* (*HNLs*) provide a good explanation for the origin of neutrino masses through different seesaw mechanisms [26]. While the mixing with $\nu_{e/\mu}$ is

[26]: Yanagida (1980), “Horizontal Symmetry and Masses of Neutrinos”

strongly constrained ($|U_{\alpha 4}^2| \lesssim 10^{-5} - 10^{-8}$, $\alpha = e, \mu$), the mixing with ν_τ is much harder to probe due to the difficulty of producing and detecting ν_τ . Figure 2.6 shows the current limits on the τ -sterile mixing space for HNL masses between 0.1 GeV-10 GeV. As was first pointed out in [32], the atmospheric neutrino flux observed in IceCube offers a way to constrain the neutrino-HNL mixing parameters. By using the large fraction of atmospheric ν_μ events that oscillate into ν_τ before they reach the detector, the less constrained τ -sterile mixing space can be explored. In this document, we present the methodology and strategy of a search for HNLs with IceCube DeepCore. These additional RH neutrinos can be included in the Standard Model (SM) by extending the PMNS matrix to at least a 3x4 matrix as

$$\begin{pmatrix} \nu_e \\ \nu_\mu \\ \nu_\tau \\ \nu_s \end{pmatrix} = \begin{pmatrix} U_{e1} & U_{e2} & U_{e3} & U_{e4} \\ U_{\mu 1} & U_{\mu 2} & U_{\mu 3} & U_{\mu 4} \\ U_{\tau 1} & U_{\tau 2} & U_{\tau 3} & U_{\tau 4} \\ U_{s1} & U_{s2} & U_{s3} & U_{s4} \end{pmatrix} \begin{pmatrix} \nu_1 \\ \nu_2 \\ \nu_3 \\ \nu_4 \end{pmatrix}, \quad (2.28)$$

where the components with index 4 define the mixing between the flavor states and the fourth sterile mass state, respectively. Note here that this is not a theoretically fully consistent picture, but rather the phenomenologically minimal model to be tested by this analysis. This can hopefully be put into the larger context of several fully consistent models, later. Due to the singlet nature of the RH neutrinos, they only interact weakly, inheriting these interactions from their LH neutrino counterparts via mixing. This mixing of the HNLs with the electron, muon, and tau neutrinos can be probed and constrained as a function of the HNL mass by searching for their production and decay. In [32, 33] this search is mainly motivated through two experimental arguments. Secondly, IceCube is ideally placed to explore the yet unconstrained $|U_{\tau 4}|^2 - m_4$ phase-space that is not easily accessible by accelerator-based experiments.

In order to probe the τ -sterile mixing parameter, it is required to look at interactions involving τ neutrinos. However, most neutrinos produced in cosmic ray interactions with the atmosphere are ν_e or ν_μ . Therefore, we need these neutrinos to oscillate to the τ flavor before reaching the detector. For this to happen at the considered energies a traveled distance of the order of the earth diameter is necessary. This is why our signal is mostly up-going and passing through the whole earth.

To explain the signature we can observe in IceCube we first have to revisit the weak interactions that the HNL inherits from its LH counterpart through mixing. We will be following the derivation in [20]. Extending the SM by n additional RH neutrinos, ν_i ($i = 3 + n$), leads to the mass Lagrangian

$$\mathcal{L}_v^{\text{mass}} \supset - \sum_{\alpha=e,\mu,\tau} \sum_{i=4}^{3+n} Y_{\nu,\alpha i} \bar{L}_{L,\alpha} \tilde{\phi} \nu_i - \frac{1}{2} \sum_{i=4}^{3+n} M_i \bar{\nu}_i \nu_i^c + h.c., \quad (2.29)$$

in a basis where the Majorana mass terms are diagonal. $Y_{\nu,\alpha i}$ are the Yukawa couplings to the lepton doublets and M the Majorana masses for the heavy singlets. $L_{L,\alpha}$ stands for the SM LH lepton doublet of flavor α while ϕ is the Higgs field, and $\tilde{\phi} = i\sigma_2 \phi^*$ and $\nu_i^c \equiv C \bar{\nu}_i^t$, with $C = i\gamma_0 \gamma_2$ in the Weyl representation. The full neutrino mass matrix with the Higgs

Produce similar styled plot for these limits

[32]: Coloma et al. (2017), "Double-Cascade Events from New Physics in Icecube"

[32]: Coloma et al. (2017), "Double-Cascade Events from New Physics in Icecube"

[33]: Coloma (2019), "Icecube/DeepCore tests for novel explanations of the Mini-BooNE anomaly"

This section really needs to be re-written to motivate the search for HNLs from a more generic point of view (e.g. to explain neutrino masses)

This section definitely needs to be elaborated in a little more detail

[20]: Coloma et al. (2021), "GeV-scale neutrinos: interactions with mesons and DUNE sensitivity"

Not adding information about the case where the neutrinos have Dirac or pseudo-Dirac masses

vacuum expectation value $v/\sqrt{2}$ reads

$$\mathcal{M} = \begin{pmatrix} 0_{3 \times 3} & Y_\nu v/\sqrt{2} \\ Y_\nu^t v/\sqrt{2} & M \end{pmatrix}, \quad (2.30)$$

and can be diagonalized by a $(3+n) \times (3+n)$ full unitary rotation U , that itself leads to neutrino masses upon diagonalization, additionally manifesting the mixing between active neutrinos and heavy states. The resulting model consists of 3 light SM neutrino mass eigenstates ν_i ($i = 1, 2, 3$) and n heavier states, as introduced above. The flavor states will now consist of a combination of light and heavy states

$$\nu_\alpha = \sum_{i=1}^{3+n} U_{\alpha i} \nu_i, \quad (2.31)$$

and the leptonic part of the EW Lagrangian can be written as

$$\begin{aligned} \mathcal{L}_{\text{EW}}^\ell = & \frac{g}{\sqrt{2}} W_\mu^+ \sum_\alpha \sum_i U_{\alpha i}^* \bar{\nu}_i \gamma^\mu P_L \ell_\alpha + \frac{g}{4c_w} Z_\mu \\ & \times \left\{ \sum_{i,j} C_{ij} \bar{\nu}_i \gamma^\mu P_L \nu_j + \sum_\alpha \bar{\ell}_\alpha \gamma^\mu [2s_w^2 P_R - (1-2s_w^2) P_L] \ell_\alpha \right\} + h.c., \end{aligned}$$

where $c_w \equiv \cos \theta_w$, $s_w \equiv \sin \theta_w$, and θ_w the SM weak mixing angle. P_L and P_R are the left and right projectors, respectively, while

$$C_{ij} \equiv \sum_\alpha U_{\alpha i}^* U_{\alpha j}. \quad (2.32)$$

The indices now sum over all $(3+n)$ flavor and mass states.

Based on this formulation and assuming that only the mixing with the tau sector is open ($|U_{\alpha 4}^2| = 0$, $\alpha = e, \mu$), the relevant production diagram of the HNL can be drawn as shown in Figure 2.7. Alongside the fourth heavy mass state, a Hadronic cascade is produced. The heavy mass state will travel for some distance (dependent on mass and mixing) before it decays. The subsequent decay processes are depicted in Figure 2.8. It can be a CC or NC decay and both leptonic and mesonic modes are possible (dependent on the mass). This will produce a tau or a tau neutrino and another cascade that can be EM or Hadronic. The branching ratios corresponding to the decay modes of the HNL for the mass range of interest (i.e. between 100 MeV and 1 GeV) are shown in Figure 2.9a as a function of the HNL mass.

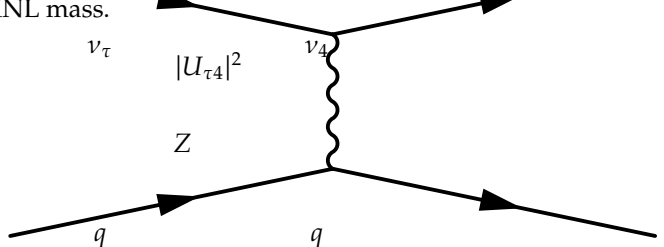


Figure 2.7: Production of a sterile neutrino in the up-scattering of a tau neutrino.

Production and Decay in IceCube DeepCore

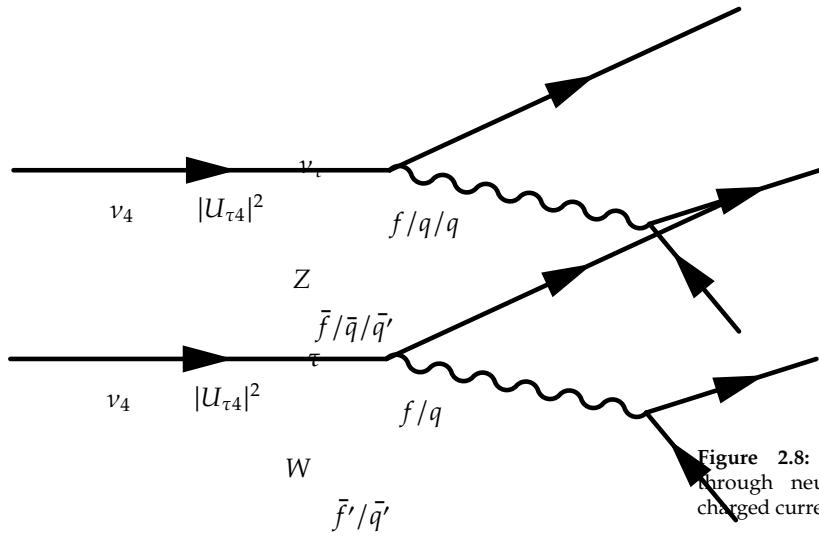


Figure 2.8: Sterile neutrino decay through neutral current (left) and charged current (right).

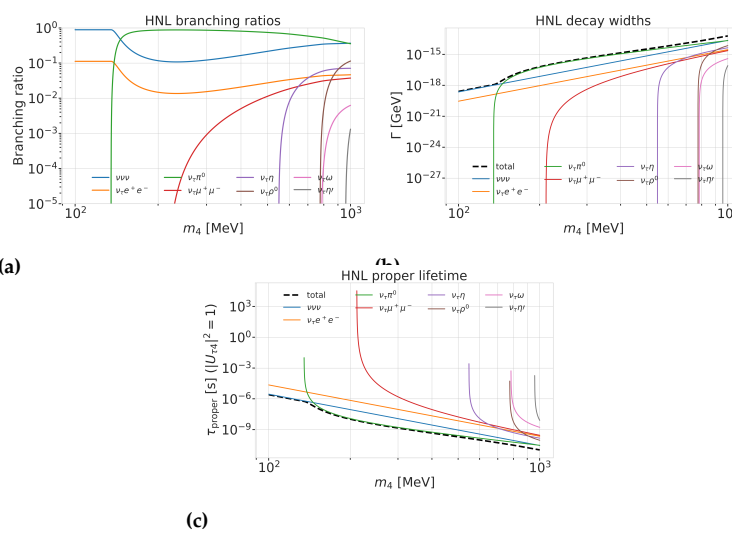


Figure 2.9: Branching ratios, decay widths, and proper lifetime of the HNL within the mass range considered, calculated based on the results from [20].

The IceCube Neutrino Observatory

3

The IceCube Neutrino Observatory [6] is a cubic-kilometer, ice-Cherenkov detector located at the geographic South Pole. IceCube utilizes the Antarctic glacial ice as detector medium to observe neutrinos by measuring the Cherenkov light produced from secondary charged particles. It was deployed between 2006 and 2011 and has been taking data since the installation of the first modules. The primary goal of IceCube is the observation of astrophysical neutrinos as a telescope, but it can also be used to study fundamental particle physics properties by measuring atmospheric neutrinos as well as studying cosmic rays.

This chapter first describes the main- and sub-array of the detector and its detection module in Section 3.1, the propagation of particles through ice is explained in Section 3.2, and finally, the signatures that IceCube can observe of the different particles are introduced in Section 3.3.

add fancy icecube picture

3.1 Detector Components . . . 17

3.2 Particle Propagation in Ice 20

3.3 Event Morphologies . . . 23

[6]: Aartsen et al. (2017), “The IceCube Neutrino Observatory: instrumentation and online systems”

3.1 Detector Components

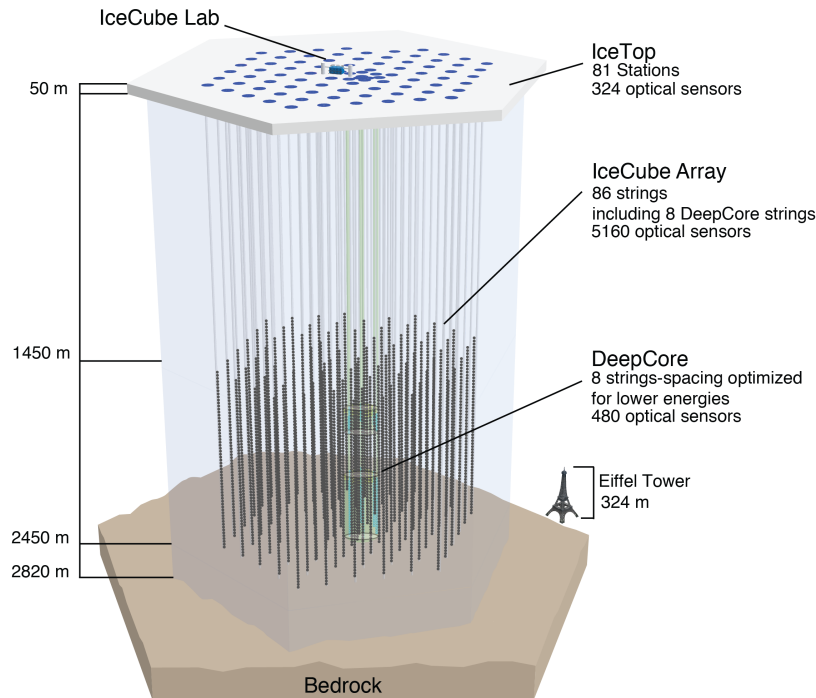


Figure 3.1: Overview of the IceCube detector showing the in-ice main- and sub-array IceCube and DeepCore, IceTop, and the IceCube Laboratory. From [6].

The full IceCube detector array consists of 86 vertical, in-ice strings and 81 surface stations as shown in Figure 3.1. The in-ice part is composed of 60 optical modules per string deployed at depths of 1450 m–2450 m below the ice, while the surface stations of the cosmic air-shower array, *IceTop*, are ice-filled tanks. The surface stations and the majority of the strings are arranged in a hexagonal grid with the operations building, the *IceCube Laboratory* (ICL), central to the grid on the surface. A top view

of the hexagonal arrangement is shown in Figure 3.4. The in-ice array is designed to detect neutrinos in the energy range from GeV to PeV.

3.1.1 Digital Optical Modules and the Antarctic Ice

[34]: Price et al. (2000), "Age vs depth of glacial ice at South Pole"

SB: there are more properties than just these. Somehow need a half sentence that explains why these are particularly important to single out (see ice papers for inspiration)

CL: maybe define that absorption and scattering lengths are? they are defined differently so this invites a comparison that is not so obvious

[35]: Abbasi et al. (2022), "In-situ estimation of ice crystal properties at the South Pole using LED calibration data from the IceCube Neutrino Observatory"

Add reference for the dust layer!

Figure 3.2: Side view of IceCube and DeepCore showing the depth dependent scattering and absorption length (left panel) and the DOM positions around the dust layer.

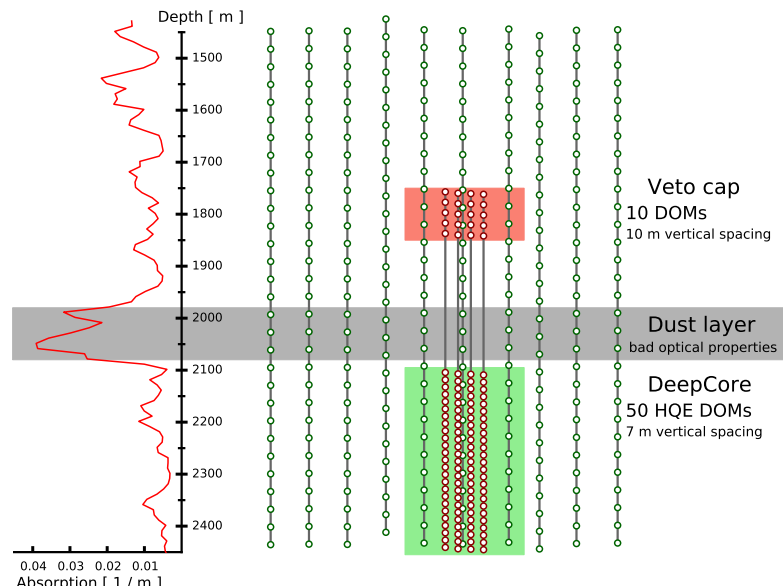
exchange for figure with scattering (check abs/sca is correct)

mention/cite dust logger paper/procedure?

[36]: Abbasi et al. (2009), "The IceCube data acquisition system: Signal capture, digitization, and timestamping"

[36]: Abbasi et al. (2009), "The IceCube data acquisition system: Signal capture, digitization, and timestamping"

The IceCube detection medium is the Antarctic glacial ice itself, which was formed over 100 000 years by accumulation of snow that was subsequently compressed by its own weight to form a dense crystal structure [34]. As a result of this formation process, the optical properties, scattering and absorption, primarily change with depth. Within the detector volume the absorption length ranges from 100 m-400 m, while the scattering length lies between 20 m and 100 m. They are correlated, with the absorption length being roughly four times the scattering length [35]. The vertical distribution of scattering and absorption length can be seen in Figure 3.2, where one dominant feature is the *dust layer* between 2000 m and 2100 m depth. This region has a higher concentration of dust particles that were deposited in a period of high volcanic activity, which leads to bad optical properties in form of larger scattering and absorption.



The ice is instrumented by 5160 optical sensors called *Digital Optical Modules* (DOMs) [36], which can detect the Cherenkov light produced by charged particles traveling through the ice. Each DOM is made of a spherical glass housing, containing a downward-facing Photomultiplier Tube (PMT), the main-board with control, readout, and processing-electronics, and a LED flasher-board for calibration purposes. The design and the individual components of a DOM can be seen in Figure 3.3.

The majority of PMTs are the 10" Hamamatsu R7081-02, which have a bialkali photocathode and are sensitive to wavelengths in the range of 300 nm to 650 nm, with a peak quantum efficiency of 25% at 390 nm. In the central part of the IceCube array the peak efficiency reaches 34%. The dark count rate in the temperature range of -40°C to -20°C is ~ 300 Hz. The DOM electronics measure the PMT voltage and control the gain. At a voltage crossing of the equivalent to 0.25 PE the waveform readout is activated [36]. Only when either one of the nearest or next to nearest

DOMs above or below also sees a voltage crossing within a 1 μ s time window¹, the voltages are digitized and sent to the ICL. Through the application of a waveform unfolding algorithm, called *WaveDeform* [37], the waveforms are compressed, and the results are the reconstructed times and charges of the photo-electrons. This is the basis for all further IceCube data processing.

The PMT is covered with a mu-metal grid (made from wire mesh), shielding the photocathode from Earth's magnetic field, and it is optically coupled to the glass sphere by RTV silicone gel. The glass sphere is a pressure vessel, designed to withstand both the constant ice pressure and the temporary pressure during the refreezing process of the water in the drill hole during deployment (peaking at around 690 bar). The sphere is held by a harness that connects the DOMs along a string and also guides the cable beside them.

The flasher-board controls 12 LEDs that produce optical pulses with a wavelength of 405 nm [6]. The LEDs can be pulsed separately or in combination with variable output levels and pulse lengths. Using the known information of the light source positions and times this can be used for in-situ calibration of the detector by measuring absorption and scattering properties of the ice. Calibrating the absolute efficiency of the DOMs itself is more accurately done using minimum ionizing muons [38, 39], since the total amplitude of the LED light is not well known.

3.1.2 IceCube

The 78 strings that are arranged in a hexagonal pattern from the main part of the in-ice array, which is called *IceCube*. With a ~125 m horizontal spacing between the strings and a ~17 m vertical spacing between DOMs, IceCube has a lower energy threshold of around 100 GeV. IceCube was designed to detect astrophysical neutrinos with energies above 1 TeV.

The coordinate system that is used in IceCube is centered at 46500'E, 52200'N at an elevation of 883.9 m [6]. Per definition, it's a right-handed coordinate system where the y-axis points along the Prime Meridian (Grid North) towards Greenwich, UK, and the x-axis points 90° clockwise from the y-axis (Grid East). The z-axis is normal to the ice surface, pointing upwards. For IceCube analyses depth is defined as the distance along the z axis from the ice surface, assumed to be at an elevation of 2832 m.

3.1.3 DeepCore

The additional 8 strings form a denser sub-array of IceCube called *DeepCore* [40]. It's located at the bottom-center of the in-ice array and its *fiducial volume* also includes the 7 surrounding IceCube strings as shown in Figure 3.4. The strings in this region have a closer average horizontal distance of about 70 m. The lower 50 DeepCore DOMs on each string are placed in the region of clear ice below the dust layer between 2100 m to 2450 m depth, where their vertical spacing is ~7 m. The remaining 10 modules on each string are placed above the dust layer to be used as veto against atmospheric muons as can be seen in Figure 3.2. Additionally, the

1: This is referred to as a *hard local coincidence* (HLC) [36].

[37]: Aartsen et al. (2014), "Energy Reconstruction Methods in the IceCube Neutrino Telescope"

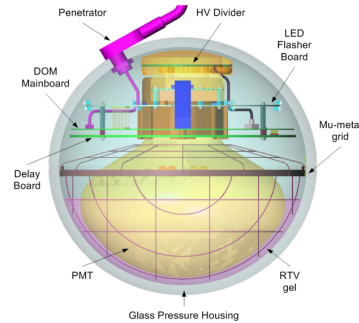


Figure 3.3: Design and components of a Digital Optical Module (DOM) [36]

[6]: Aartsen et al. (2017), "The IceCube Neutrino Observatory: instrumentation and online systems"

[38]: Feintzeig (2014), "Searches for Point-like Sources of Astrophysical Neutrinos with the IceCube Neutrino Observatory"

[39]: Kulacz (2019), "In Situ Measurement of the IceCube DOM Efficiency Factor Using Atmospheric Minimum Ionizing Muons"

Add accuracy of the efficiency calibration here.

[6]: Aartsen et al. (2017), "The IceCube Neutrino Observatory: instrumentation and online systems"

Maybe throw the coordinate system in a box on the side?

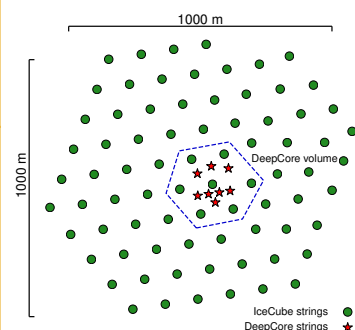


Figure 3.4: Top view of the IceCube array.

Blow up this image a bit, so it's better readable as marginfigure.

[40]: Abbasi et al. (2012), "The design and performance of IceCube DeepCore"

CL: value?

SB: this needs revision. the energy range you mention is particular for oscillations already (atmopsheric neutrinos are plentiful outside of this range you mentioned). If you rewrite the first part you'll have to revisit the second part. Also in general I'd suggest not to rank analyses like Main and Other - DeepCore was orginally intended as a dark matter detector, and there are probably more DM analyses unblinded / year than oscillations. Just keep it general, no need to rank.

[41]: Cherenkov (1937), "Visible Radiation Produced by Electrons Moving in a Medium with Velocities Exceeding that of Light"

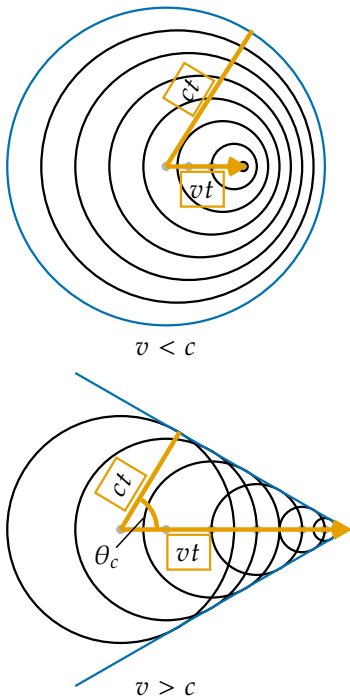


Figure 3.5: Schematic depiction of the spherical light front produced by a particle traveling slower than the speed of light in the medium (top) and the formation of the Cherenkov light front produced by a charged particle traveling faster than the speed of light in the medium (bottom). Blue is the resulting wavefront, while the black circles are spherically emitted light at each position and the orange arrows show the direction of the particle.

DeepCore DOMs are equipped with higher quantum efficiency PMTs. The combination of the denser spacing, the high quantum efficiency modules, and the most favorable ice properties below the dust layer leads to a lower energy detection threshold of around 5 GeV, allowing the more efficient observation of atmospheric neutrinos, which are mostly in the energy range of 10 GeV-100 GeV. The main analysis performed with DeepCore is an atmospheric neutrino oscillation measurement, but the large flux of atmospheric neutrinos allows for many other Beyond Standard Model searches, such as searches for dark matter, non-standard interactions, or sterile neutrinos.

3.2 Particle Propagation in Ice

Neutrinos interacting in the ice via DIS produce muons, electromagnetic showers, and hadronic showers, depending on their flavor and the interaction type. The particles produced in those processes mainly lose their energy through *ionization*, *bremsstrahlung*, *pair production*, and the *photo-nuclear interaction*. Electrically charged particles also emit Cherenkov light when traveling through the ice, which is the main observable in IceCube, but only contributes a small amount to the total energy loss. The Cherenkov effect and the energy losses of the particles are described in the following sections, followed by an overview of the different particle signatures in IceCube.

3.2.1 Cherenkov Effect

When a charged particle moves through a medium with a velocity that is greater than the speed of light in that medium, it emits Cherenkov radiation, losing a very small amount of energy ($\mathcal{O}(10^{-4})$ of the total energy loss). The detection principle of IceCube DeepCore, is based on the observation of resulting Cherenkov photons that are emitted by the charged secondary particles produced in the neutrino interactions that were introduced in Section ???. The Cherenkov effect was first observed by Pavel Cherenkov in 1934 [41] and occurs when the charged particle travels faster than the phase velocity of light, therefore polarizing the medium. Upon de-excitation the molecules emit the received energy as photons in a spherical wavefront. Since the particle moves past this wavefront, the superposition of the spherical light emissions forms a cone, which is shown in blue in the bottom panel of Figure 3.5.

Using trigonometry, the angle θ_c at which the Cherenkov light is emitted can be calculated as

$$\theta_c = \arccos\left(\frac{1}{\beta n}\right), \quad (3.1)$$

where β is the velocity of the particle in units of the speed of light and n is the refractive index of the medium. When the particle velocity is close to the speed of light, the equation holds and the angle is only dependent on the refractive index of the medium. For the Antarctic ice, the refractive index is $n \approx 1.3$ and as a result $\theta_c \approx 41^\circ$.

The frequency of the emission depends on the charge z and the wavelength-dependent index of refraction $n(\omega)$ and is given by the Frank-Tamm

formula [42, 43]

$$\frac{d^2N}{dx d\lambda} = \frac{2\pi\alpha z^2}{\lambda^2} \left(1 - \frac{1}{\beta^2 n(\omega)^2}\right), \quad (3.2)$$

with $\alpha \approx 1/137$ the fine structure constant, λ the wavelength of the emitted light, and x the path length traversed by the particle. Relativistic particles in ice produce roughly 250 photons per cm in the wavelength range of 300 nm-500 nm [44].

3.2.2 Energy Losses

Even though relativistic, charged particles traveling through matter produce Cherenkov radiation, their energy is mainly lost through other processes that are dependent on the particle type and energy. The exact principles of energy loss for the different types can broadly be categorized into the three groups: quasi-continuous energy loss by muons, electromagnetic cascades, and hadronic cascades.

Muons

Muons lose their energy by ionization, bremsstrahlung, pair production, and the photo-nuclear effect. The energy loss by ionization is the dominant process for muons above 1 GeV and has a weak energy dependence given by

$$\left\langle -\frac{dE}{dx} \right\rangle = a_I(E) + b_R(E) \cdot E, \quad (3.3)$$

where E is the energy and $a_I(E)$ and $b_R(E) \cdot E$ are the energy loss by ionization and the combined radiative losses, respectively. In the energy range relevant for this work (10 GeV-100 GeV), the parameters a_I and b_R only depend on energy very weakly and can be approximated by constants. The energy loss is then given by

$$\left\langle -\frac{dE}{dx} \right\rangle = a + b \cdot E. \quad (3.4)$$

Based on this description, there is a critical energy which divides the regimes where ionization and radiative losses dominate. The critical energy is given by $E_{\text{crit}} = a/b$ and for muons in ice it is ~ 713 GeV (using $a \approx 2.59 \text{ MeV cm}^{-1}$ and $b \approx 3.63 \times 10^{-6} \text{ cm}^{-1}$ [45]). Since the energy range of interest is well below this critical energy, the range of a muon can easily be related to its energy by

$$\langle L \rangle = \frac{E_0}{a}. \quad (3.5)$$

Measuring the length of a muon track therefore allows for an estimation of its energy if the full track is contained within the instrumented volume of IceCube. Using the given numbers a 30 GeV muon travels ~ 116 m. This approximate treatment does not take into account the stochastic nature of some energy losses. Bremsstrahlung and photo-nuclear interactions for example rarely occur, but when they do, they deposit a large chunk of energy. A thorough investigation of the energy losses of muons in ice can be found in [46].

Cite n and θ_c

[42]: Frank et al. (1937), "Coherent visible radiation from fast electrons passing through matter"

[43]: Tamm (1991), "Radiation Emitted by Uniformly Moving Electrons"

[44]: Rädel et al. (2012), "Calculation of the Cherenkov light yield from low energetic secondary particles accompanying high-energy muons in ice and water with Geant4 simulations"

SB: you already mentioned that Cher. Rad. doesn't lead to significant energy loss. I suggest to clean up the text a bit, you don't need to emphasize that so many times. Pick one place (probably here) and eliminate it elsewhere

Add reference (PDG or find original)

[45]: Chirkov et al. (2004), "Propagating leptons through matter with Muon Monte Carlo (MMC)"

SB: i like that you give a benchmark value here, for rule of thumb or so, but it should be related to the detector geometry somehow or else it feels too out of place. Give it some context

[46]: Raedel (2012), "Simulation Studies of the Cherenkov Light Yield from Relativistic Particles in High-Energy Neutrino Telescopes with Geant4"

Electromagnetic Showers

Photons as well as electrons and positrons are produced either directly in neutrino interactions or in secondary particle interactions. Above a critical energy E_c , they lose their energy through repeated pair production and bremsstrahlung emission forming an expanding, electromagnetic shower profile. The particles' energy reduces with every interaction and their number increases until they fall below the critical energy where ionization and excitation of surrounding atoms become the dominant energy loss processes for electrons and positrons. For photons the remaining energy is lost through the Compton effect and the photoelectric effect. Below the critical energy no new shower particles are produced. Electromagnetic cascades can be characterized by the radiation length, X_0 , after which electrons/positrons reduced their energy to $1/e$ of their initial energy. For photons, it's equivalent to $7/9$ of the mean free path of pair production. The critical energy for ice is $E_c \approx 78$ MeV, with a radiation length of $X_0 \approx 39.3$ cm [19].

Add reference for these processes.

[19]: Tanabashi et al. (2018), "Review of Particle Physics"

cite em shower distribution

The radiation length governs the longitudinal shower profile and using $t = x/X_0$, the shower intensity can be described by

$$\frac{dE}{dt} = E_0 b \frac{(bt)^{a-1} e^{-bt}}{\Gamma(a)}, \quad (3.6)$$

[46]: Raedel (2012), "Simulation Studies of the Cherenkov Light Yield from Relativistic Particles in High-Energy Neutrino Telescopes with Geant4"

[47]: Agostinelli et al. (2003), "Geant4—a simulation toolkit"

Add angular profile plot (Summer agrees!) (create one based on Leif Rädel as Alex did)

SB: rephrase gamma (from equation) is not defined

where a and b are parameters that have to be estimated from experiment. Based on the work from [46], performed with Geant4 [47], the parameters for electromagnetic showers in ice are

$$e^- : a \approx 2.01 + 1.45 \log_{10}(E_0/\text{GeV}), b \approx 0.63, \quad (3.7a)$$

$$e^+ : a \approx 2.00 + 1.46 \log_{10}(E_0/\text{GeV}), b \approx 0.63, \quad (3.7b)$$

$$\gamma : a \approx 2.84 + 1.34 \log_{10}(E_0/\text{GeV}), b \approx 0.65. \quad (3.7c)$$

The maximum of the shower is at $t_{max} = (a - 1)/b$ and the Cherenkov emission of the charged particles produced in the shower is peaked around the Cherenkov angle, since they are produced in the forward direction.

Hadronic Showers

The breaking nucleus or any hadronic decay products from the neutrino DIS interactions always create a hadronic cascade. It is a result of secondary particles produced in strong interactions between the hadrons and the traversed matter. The charged particles produced in the shower will emit Cherenkov radiation, while neutral particles will be invisible to the detector. There is also an electromagnetic component of the shower, due to for example the decay of neutral pions into photons. Hadronic showers of the same energy as electromagnetic showers have larger fluctuations in energy deposition and shape, since they depend on the produced particle types. Hadrons also have a higher energy threshold for Cherenkov light production, because of their higher mass. Based on [46, 48], the visible electromagnetic fraction of hadronic showers can be

[46]: Raedel (2012), "Simulation Studies of the Cherenkov Light Yield from Relativistic Particles in High-Energy Neutrino Telescopes with Geant4"

[48]: Gabriel et al. (1994), "Energy dependence of hadronic activity"

parameterized as

$$F(E_0) = \frac{T_{\text{hadron}}}{T_{\text{EM}}} = 1 - (1 - f_0) \left(\frac{E_0}{E_s} \right)^{-m}, \quad (3.8)$$

where $T_{\text{hadron/EM}}$ is the total track length of a hadronic/electromagnetic shower with the same energy, f_0 is the ratio of hadronic and electromagnetic light yield, E_0 is the initial energy, and E_s is an energy scale. The parameter m is an arbitrary parameter. The ratio $F(E_0)$ increases with energy, but is always smaller than 1. The variance of this distribution is given by

$$\sigma_F(E_0) = \sigma_0 \log(E_0)^{-\gamma}. \quad (3.9)$$

The parameters m , E_s , and f_0 are fit from simulation. Cherenkov light from hadronic showers also peaks around the Cherenkov angle, but the angular distribution is more smeared out, due to the variations in particle type and their energy depositions.

SB: Explain

3.3 Event Morphologies

The event morphologies produced by particles detected in IceCube are combinations of the three energy loss types described in Section 3.2.2, e.g. *cascades* from electromagnetic and hadronic showers and elongated *tracks* from muons traveling through the detector. Table 3.1 gives an overview of the possible event signatures.

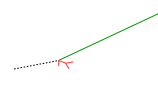
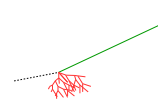
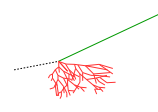
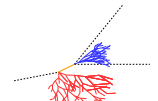
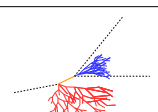
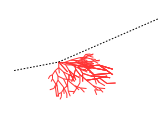
Interaction	Secondary particles	Signature
CC $\nu_\mu^{(-)}$	 μ^\pm track	Track-only
	 μ^\pm track and hadrons	Cascade + track
CC $\nu_\tau^{(-)}$	 τ^\pm decaying into μ^\pm (~17% BR), hadrons	
	 τ^\pm decaying into e^\pm or hadrons (~83% BR)	
CC $\nu_e^{(-)}$	 e^\pm , hadrons	Cascade-only
NC $\nu_\ell^{(-)}$	 hadrons	

Table 3.1: IceCube low energy event signatures, their underlying interaction type, and the particles that produce them. Also shown are the secondary particles produced in the interactions. Black dashed lines represent neutrinos, green lines muons, orange line leptons, and blue and red lines are particles in electromagnetic and hadronic cascades, respectively. Adapted from [17].

Neutrino interactions are observed as cascades, tracks, or a combination of both, depending on the initial flavor and the interaction type for the specific event.

In ν_μ - CC interactions, a muon is produced in addition to a hadronic shower from the breaking nucleus. If the interaction happens outside the detector, but the muon passes through the detector, this will create a track-like signature. The same happens if the interaction happens inside, but the energy transfer to the nucleus is small ($y \approx 0$). At energies relevant for this work, tracks have length at the same order of the distance between DOMs, so they can be observed as such.

Make sure I have this defined in the SM interaction chapter!

If the interaction happens inside the detector and the energy transfer to the hadronic part of the shower is larger, it will create a cascade with a track leaving it. A similar signature is observed after a ν_τ - CC interaction, in which a tau is produced that later decays into a muon, with a branching ratio of 17 %. In those cases the muon usually has a lower energy and the track will be fainter and harder to observe.

The other 83 % of ν_τ - CC interactions produce a tau that decays into an electron or hadrons, leaving a cascade-only signature through the electromagnetic or hadronic shower. All ν_e - CC interactions also produce pure cascades, since the electron quickly loses its energy in an electromagnetic shower. In all ν - NC interactions, the produced neutrino escapes and only the hadronic shower is observable. Since the size of the cascades at the energy range of interest is smaller than the spacing of the DOMs, they are approximately observed as point-like, spherical light sources. Considering the short effective scattering length (20 m-50 m), the light is almost isotropically emitted.

SB: Since your analysis depends on the ability to reconstruct cascade directions, it seems odd to emphasize that the light is nearly isotropically emitted. Of course that is true, but the emphasis should rather be on the fact that there remains some asymmetry to the light profile

Atmospheric muons also produce pure track like signatures, similar to ν_μ - CC interactions happening outside the detector. They are one of the main backgrounds for analyses using atmospheric neutrinos and are therefore the target of many filter steps described in Section 5.3.1.

Heavy Neutral Lepton Signal Simulation

4

After the SM simulation generation and the default low energy event selection and processing chain were introduced in the previous Chapter 5, the focus will now be on the central part of this thesis - the HNL signal simulation. Since this is the first search for HNLs with IceCube DeepCore, there was no prior knowledge of the number of events expected per year nor of the expected performance in terms of reconstruction and classification accuracy which governs the 90 % confidence level on estimateing the $|U_{\tau 4}|^2$ mixing matrix element. This is the first simulation developed for IceCube DeepCore. Two avenues of simulation generation were pursued in parallel. The physically accurate, model dependent simulation is described in Section 4.2 and a collection of model independent simulation sets was realized and is explained in Section 4.1. The latter is used for performance benchmarking and as a cross-check for the model dependent simulation

Adapt to reflect switched chapter order	
4.1 Model Independent Simulation	25
4.2 Model Dependent Simulation	28

4.1 Model Independent Simulation

To investigate the potential of IceCube to detect HNLs by identifying the unique double cascade morphology explained in Section 2.3.4, it is very valuable to have simulation sets where the double cascade kinematics can be controlled directly. In a realistic model the decay kinematics and the absolute event expectation all depend on the specific model parameters chosen (see Section ??). To decouple the simulation from a specific parameter choice, a model independent double cascade generator was developed. Using this generator a few simulation sets were produced to investigate the performance of IceCube DeepCore to detect low energetic double cascades, dependent on their properties. All simulation sets are produced using a collection of custom generator functions [49] that place two EM cascade vertices with variable energy and direction at choosable locations in the detector. The results of this study will be discussed in Chapter 6.

4.1.1 Simplistic Sets

To investigate some idealistic double cascade event scenarios, two sets are produced for straight up-going events that are centered on a string and horizontal events located inside DeepCore.

The first set is used to investigate one of the most promising scenarios to detect a double cascade, where both cascade centers are located on a DeepCore string (namely string 81) and the directions are directly up-going. The horizontal positions and distances of all DeepCore fiducial volume strings are shown in Figure 4.1 and string 81 is at a medium distance of ~ 70 m to its neighboring strings. As already mentioned in Section 3.1.3, DeepCore strings have higher quantum efficiency DOMs and a denser vertical spacing, making them better to detect low energetic

Make my own DC string positions/distances plot version.

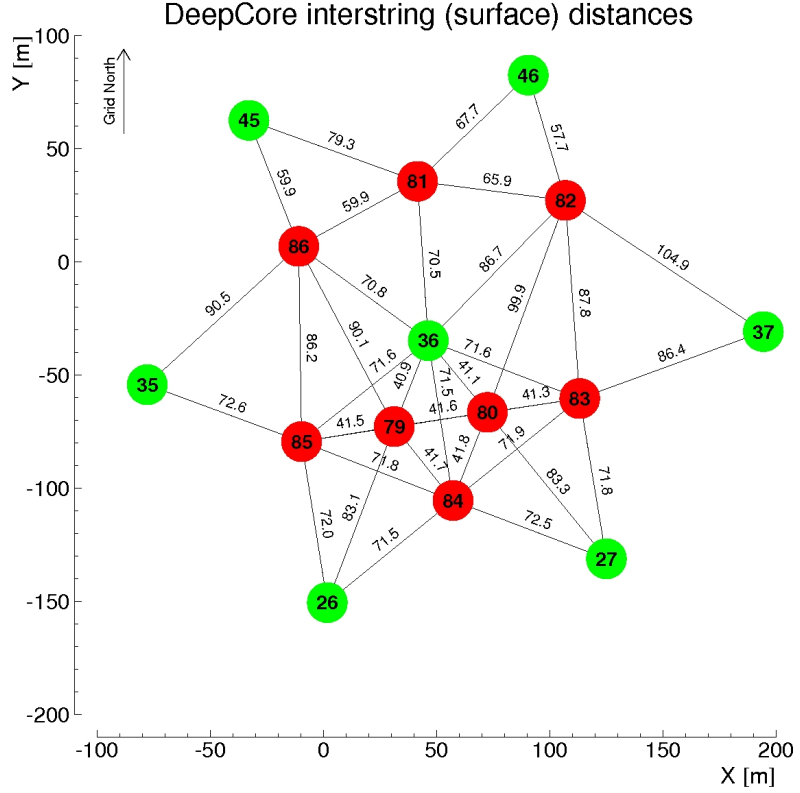


Figure 4.1: Horizontal positions and distances between DeepCore strings. Red strings are instrumented more densely (vertically) and partially have higher quantum efficiency (HQE) DOMs.

events that produce little light. To produce the events, the x, y position of the cascades is fixed to the center of string 81 while the z position is sampled uniformly along the axis of the string. The energies are sampled uniformly between 0.0 GeV and 60.0 GeV. The specific sampling distributions/values for the cascades are listed in Table 4.1. The order of the cascades is chosen such that the lower one is first ($t_0 = 0.0$ ns) and the upper one is second ($t_1 = L/c$), assuming the speed of light c as speed of the heavy mass state, traveling between the two cascades.

The second set is used to investigate the reconstruction performance for horizontal events, where the spacing between DOMs is much larger. The cascades are placed uniformly on a circle centered in DeepCore. The direction is always horizontal and azimuth is defined by the connecting vector of both cascade positions. The energies are again sampled uniformly between 0.0 GeV and 60.0 GeV and the detailed sampling distributions/-values are also listed in Table 4.1. Some examples of the generation level distributions of the simplified sets are shown in Figure 4.2, while further distributions can be found in Figure A.1. The variables that are uniformly sampled or fixed to a certain value are not presented.

Re-make plot with all energies (cascades and total, both sets (they are the same))

Re-make plot with all decay lengths (both sets)

4.1.2 Realistic Set

To thoroughly investigate the potential of IceCube DeepCore to detect double cascade events, a more realistic simulation set is produced that aims to be as close as possible to the expected signal simulation explained in Section 4.2, while still allowing some freedom to control the double cascade kinematics. For this purpose the total energy is sampled from an E^{-2} power law, mimicking the energy spectrum of the primary neutrinos

Set	Variable	Distribution	Range/Value
Up-going			
	energy	uniform	0.0 GeV to 60.0 GeV
	zenith	fixed	180.0°
	azimuth	fixed	0.0°
	x, y position	fixed	(41.6, 35.49) m
	z position	uniform	-480.0 m to -180.0 m
Horizontal			
	energy	uniform	0.0 GeV to 60.0 GeV
	zenith	fixed	90.0°
	azimuth	uniform	0.0° to 360.0°
	x, y position	uniform (circle)	c=(46.29, -34.88) m, r=150.0 m
	z position	fixed	-330.0 m

Table 4.1: Generation level sampling distributions and ranges/values of up-going and horizontal model independent simulation.

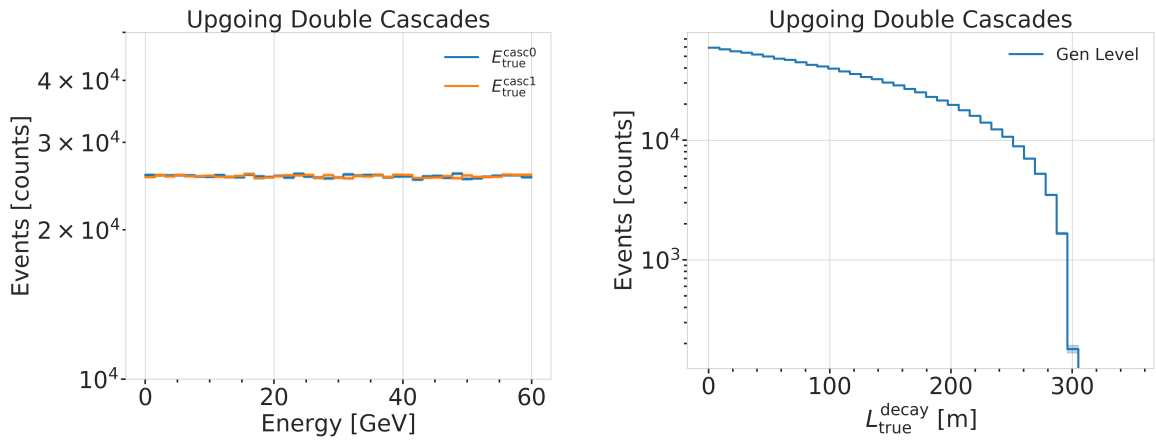


Figure 4.2: Generation level distributions of the simplistic simulation sets. Cascade and total energies (left) and decay lengths (right) of both sets are shown.

as stated in Section 5.1.1. Although in the realistic process described in Section 4.2 the energy is distributed in a more complex way into the two cascades and secondary particles, it is a good approximation to simply divide the total energy into two parts. This is done by randomly assigning a fraction between 0 % and 100 % to one cascade and the remaining part to the other cascade. In this way the whole sample covers various cases of energy distributions between the two cascades. To efficiently generate events in a way that produces distributions similar to what would be observed with DeepCore, one of the cascade positions is sampled inside the DeepCore volume by choosing its coordinates randomly on a cylinder that is centered in DeepCore. This is similar to a trigger condition of one cascade always being inside the DeepCore fiducial volume. By choosing the direction of the event sampling zenith and azimuth uniformly between 70° and 180° and 0° and 360°, respectively, the position of the other cascade can be inferred for a given decay length. The length is sampled from an exponential distribution, which would be expected for the decaying heavy mass state. Based on the direction and the decay length, the position of the other cascade is found, assuming a travel speed of c and randomly choosing whether the cascade position that was sampled is the first cascade or the second and then assigning the other cascade position accordingly. The sampling distributions/values are listed in Table 4.4. Example distributions of the generation level variables are shown in Figure 4.3, while further distributions can be

Table 4.2: Generation level sampling distributions and ranges/values of the realistic model independent simulation.

Variable	Distribution	Range/Value
energy (total)	power law E^{-2}	1 GeV to 1000 GeV
decay length	exponential $e^{-0.01L}$	0 m to 1000 m
zenith	uniform	70° to 180°
azimuth	uniform	0° to 360°
x, y (one cascade)	uniform (circle)	$c=(46.29, -34.88)$ m, $r=150$ m
z (one cascade)	uniform	-480.0 m to -180.0 m

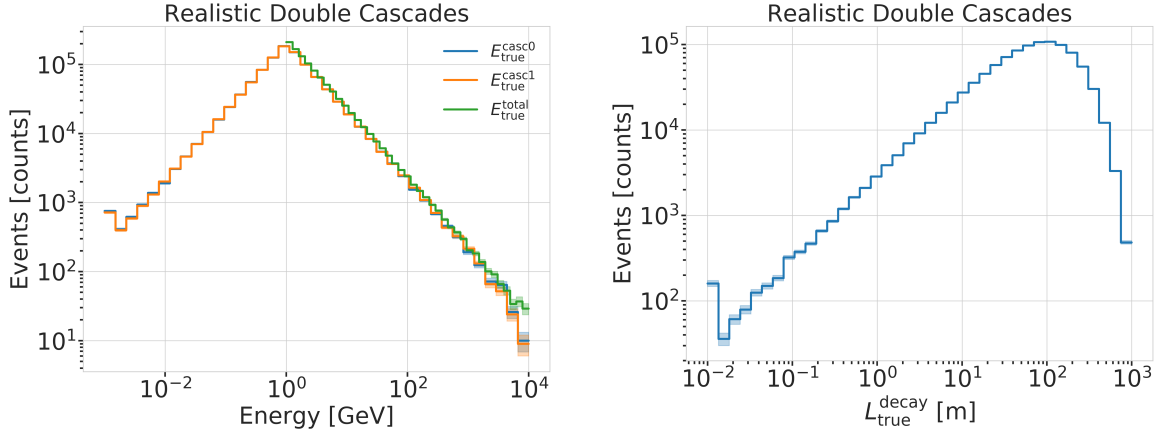


Figure 4.3: Generation level distributions of the simplistic realistic set. Shown are the cascade and total energies (left) and decay lengths (right).

found in Figure A.2.

4.2 Model Dependent Simulation

To estimate the HNL event expectation in IceCube DeepCore, depending on the specific model parameters, a generator was developed that is based on the HNL theory introduced in Section ???. For this work, only the interaction with the τ -sector was taken into account ($|U_{\alpha 4}^2| = 0$, $\alpha = e, \mu$), which reduces the physics parameters of interest and relevant for the simulation to the fourth heavy lepton mass, m_4 , and the mixing, $|U_{\tau 4}^2|$. The generator uses a customized *LEPTONINJECTOR* (LI) version to create the events and *LEPTONWEIGHTER* (LW) to weight them [50]. The modified LI and the essential components needed for the HNL simulation are described in the next sections, followed by the description of the weighting scheme and the sampling distributions chosen for the simulation generation.

[50]: Abbasi et al. (2021), “LeptonInjector and LeptonWeighter: A neutrino event generator and weighter for neutrino observatories”

4.2.1 Custom LeptonInjector

In its standard version, the LI generator produces neutrino interactions by injecting a lepton and a cascade¹ at the interaction vertex of the neutrino, where the lepton is the charged (neutral) particle produced in a CC (NC) interaction and the cascade is the hadronic cascade from the breaking nucleus. Both objects are injected with the same (x, y, z, t) coordinates and the kinematics are sampled from the differential and total cross-sections that are one of the inputs to LI.

1: The cascades are defined as icetray I3Particles with type *Hadrons*.

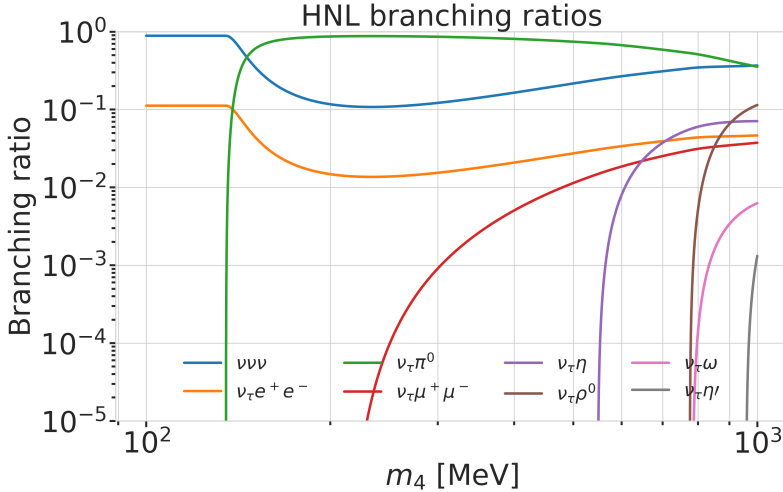


Figure 4.4: Branching ratios of the HNL within the mass range considered in this work, only considering $|U_{\tau 4}^2| \neq 0$, calculated based on the results from [20].

In the modified version, the SM lepton at the interaction vertex is replaced by the new HNL particle, where the interaction cross-sections are replaced by custom, mass dependent HNL cross-sections. The HNL is forced to decay after a chosen distance to produce secondary SM particles, where the decay mode is randomly chosen based on the mass dependent branching ratios from the kinematically accessible decay modes shown in Figure 4.4. The cross-section and decay width calculations were implemented for this purpose and will be explained in more detail in the following. Another needed addition to LI is that the decay products of the HNL are also added to the list of MC particles in each event. They are injected with the correctly displaced position and delayed time from the interaction vertex, given the HNL decay length. These HNL daughter particles form the second cascade, not as a single hadronic cascade object, but as the explicit particles forming the shower. The kinematics of the two-body decays are computed analytically, while the three-body decay kinematics are calculated with `MADGRAPH` [51], which will also be explained further below. Independent of the number of particles in the final state of the HNL decay, the kinematics are calculated/simulated at rest and then boosted along the HNL momentum.

The injection is done using the LI *volume mode*, for the injection of the primary particle on a cylindrical volume, adding 50 % of the events with ν_τ and the other half with $\bar{\nu}_\tau$ as primary particle types. The generator takes the custom double-differential/total cross-section splines described below and the parameters defining the sampling distributions as inputs.

[51]: Alwall et al. (2014), “The automated computation of tree-level and next-to-leading order differential cross sections, and their matching to parton shower simulations”

Cross-Sections

The cross-sections are calculated using the NuXSSPLMKR [52] software, which is a tool to calculate neutrino cross-sections from *parton distribution functions (PDFs)* and then produce splines that can be read and used with LI/LW. The tool was customized to produce the custom HNL cross-sections, where the main modification to calculate the cross-sections for the ν_τ -NC interaction into the new heavy mass state is the addition of a kinematic condition to ensure that there is sufficient energy to produce the heavy mass state. It is the same condition that needs to be fulfilled

[53]: Levy (2009), “Cross-section and polarization of neutrino-produced tau’s made simple”

for the CC case, where the outgoing charged lepton mass is non-zero. Following [53] (equation 7), the condition

$$(1 + x\delta_N)h^2 - (x + \delta_4)h + x\delta_4 \leq 0 \quad (4.1)$$

is implemented for the NC case in the NuXSSplMkr code. Here $\delta_4 = \frac{m_4^2}{s-M^2}$, $\delta_N = \frac{M^2}{s-M^2}$, and $h \stackrel{\text{def}}{=} xy + \delta_4$, with x, y being the Bjorken variables, m_4 and M the mass of the heavy state and the target nucleon, respectively, and s the center of mass energy squared.

Re-make plot with 3 target masses and better labels

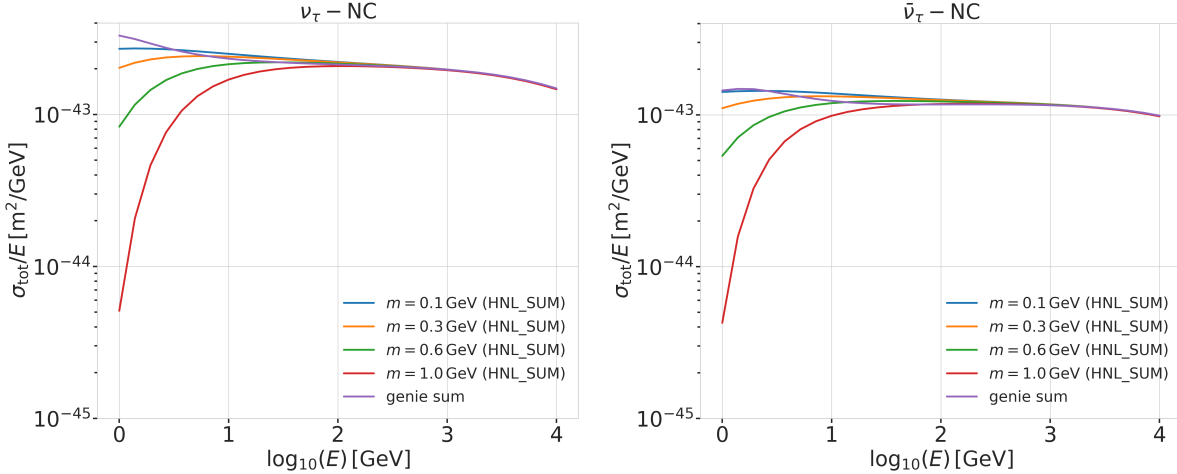


Figure 4.5: Custom HNL total cross-sections for the four target masses compared to the total ($\nu_\tau/\bar{\nu}_\tau$ NC) cross-section used for SM neutrino simulation production with GENIE.

Add comparisons of SM cross-sections between NuXSSplMkr and genie?

add varied total cross-section for a few background HNL events (for QE/RES variations?!)

[20]: Coloma et al. (2021), “GeV-scale neutrinos: interactions with mesons and DUNE sensitivity”

As already described in Section 5.1.1, the SM neutrino background simulation is created using the GRV98LO PDFs. These PDFs also had to be added to the cross-section spline maker, to ensure good agreement between the background and signal cross-sections. The double differential ($ds/dxdy$) and total (σ) cross-sections were produced for the chosen target HNL masses and then splined. The produced cross-section are added to the custom LI version and used for the simulation generation and weighting. Figure 4.5 shows the total cross-sections that were produced compared to the cross-section used for the production of the SM $\nu_\tau/\bar{\nu}_\tau$ NC background simulation. Above $\sim 2 \times 10^2$ GeV they match, which is the wanted result of using the identical input PDFs.

Channel	Opens	BR
$\nu_4 \rightarrow \nu_\tau \nu_\alpha \bar{\nu}_\alpha$	0 MeV	1.0
$\nu_4 \rightarrow \nu_\tau e^+ e^-$	1 MeV	?
$\nu_4 \rightarrow \nu_\tau \pi^0$	135 MeV	?
$\nu_4 \rightarrow \nu_\tau \mu^+ \mu^-$	211 MeV	?
$\nu_4 \rightarrow \nu_\tau \eta$	548 MeV	?
$\nu_4 \rightarrow \nu_\tau \rho^0$	770 MeV	?
$\nu_4 \rightarrow \nu_\tau \omega$	783 MeV	?
$\nu_4 \rightarrow \nu_\tau \eta'$	958 MeV	?

Table 4.3: Possible decay channels of the HNL, considering only $|U_{\tau 4}|^2 \neq 0$. Listed is the mass at which each channel opens and the maximum branching ratio.

Decay Channels

The accessible decay channels are dependent on the mass of the HNL and the allowed mixing. For this analysis, where only $|U_{\tau 4}|^2 \neq 0$, the considered decay channels are listed in Table 4.3 and the corresponding branching ratios are shown in Figure 4.4. The individual branching ratio for a specific mass is calculated as $\text{BR}_i(m_4) = \Gamma_i(m_4)/\Gamma_{\text{total}}(m_4)$, where $\Gamma_{\text{total}}(m_4) = \sum \Gamma_i(m_4)$. The formulas to calculate the decay widths show up in multiple references, but we chose to match them to [20], which also discusses the discrepancies in previous literature.

Calculate max BRs

2-Body Decay Widths The decay to a neutral pseudoscalar meson is

$$\Gamma_{\nu_4 \rightarrow \nu_\tau P} = |U_{\tau 4}|^2 \frac{G_F^2 m_4^3}{32\pi} f_P^2 (1 - x_P^2)^2, \quad (4.2)$$

with $x_P = m_P/m_4$ and the *effective decay constants* given by

$$f_{\pi^0} = 0.130 \text{ GeV}, \quad f_\eta = 0.0816 \text{ GeV}, \quad f_{\eta'} = -0.0946 \text{ GeV}, \quad (4.3)$$

while the decay to a neutral vector meson is given by

$$\Gamma_{\nu_4 \rightarrow \nu_\tau V} = |U_{\tau 4}|^2 \frac{G_F^2 m_4^3}{32\pi} \left(\frac{f_V}{m_V} \right)^2 g_V^2 (1 + 2x_V^2)(1 - x_V^2)^2, \quad (4.4)$$

with $x_V = m_V/m_4$,

$$f_{\rho^0} = 0.171 \text{ GeV}^2, \quad f_\omega = 0.155 \text{ GeV}^2, \quad (4.5)$$

and

$$g_{\rho^0} = 1 - 2 \sin^2 \theta_w, \quad g_\omega = \frac{-2 \sin^2 \theta_w}{3}, \quad \sin^2 \theta_w = 0.2229 \quad (4.6)$$

[54].

[54]: Tiesinga et al. (2021), “CODATA recommended values of the fundamental physical constants: 2018”

3-Body Decay Widths The (invisible) decay to three neutrinos is

$$\Gamma_{\nu_4 \rightarrow \nu_\tau \nu_\alpha \bar{\nu}_\alpha} = |U_{\tau 4}|^2 \frac{G_F^2 m_4^5}{192\pi^3}, \quad (4.7)$$

while the decay to two charged leptons (using $x_\alpha = (m_\alpha/m_4)^2$) of the same flavor reads

$$\Gamma_{\nu_4 \rightarrow \nu_\tau l_\alpha^+ l_\alpha^-} = |U_{\tau 4}|^2 \frac{G_F^2 m_4^5}{192\pi^3} [C_1 f_1(x_\alpha) + C_2 f_2(x_\alpha)], \quad (4.8)$$

with the constants defined as

$$C_1 = \frac{1}{4}(1 - 4s_w^2 + 8s_w^4), \quad C_2 = \frac{1}{2}(-s_w^2 + 2s_w^4), \quad (4.9)$$

the functions as

$$f_1(x_\alpha) = (1 - 14x_\alpha - 2x_\alpha^2 - 12x_\alpha^3)\sqrt{1 - 4x_\alpha} + 12x_\alpha^2(x_\alpha^2 - 1)L(x_\alpha), \quad (4.10)$$

$$f_2(x_\alpha) = 4[x_\alpha(2 + 10x_\alpha - 12x_\alpha^2)\sqrt{1 - 4x_\alpha} + 6x_\alpha^2(1 - 2x_\alpha + 2x_\alpha^2)L(x_\alpha)], \quad (4.11)$$

and

$$L(x) = \ln \left(\frac{1 - 3x_\alpha - (1 - x_\alpha)\sqrt{1 - 4x_\alpha}}{x_\alpha(1 + \sqrt{1 - 4x_\alpha})} \right). \quad (4.12)$$

3-Body Decay Kinematics with MadGraph

The specific MadGraph version used to produce the 3-body decay kinematics is [MadGraph4 v3.4.0](#). As input, the decay diagrams calculated

JVS: consider also writing down the (trivial) 2-body decay kinematics for completeness and consistency. This transition is a bit jarring as it is

[20]: Coloma et al. (2021), “GeV-scale neutrinos: interactions with mesons and DUNE sensitivity”

with FeynRules 2.0 using the Lagrangians derived in [20]. The Universal FeynRules Output (UFO) from EFFECTIVE_HEAVY_N_MAJORANA_v103 were used for our calculation. For each mass and corresponding decay channels, we produce 1×10^6 decay kinematic variations in the rest frame and store those in a text file. During event generation, we uniformly select an event from that list, to simulate the decay kinematics of a 3-body decay.

4.2.2 Sampling Distributions

In principle, the generation level sampling distributions should be chosen such that at final level of the selection chain the phase space relevant for the analysis is covered with sufficient statistics to make a reasonable estimate of the event expectation. Insufficiently large initial distributions lead to an underestimate of the expected rates, because part of the events that would pass the selection are not produced. This would still be correct as in being the more conservative estimate, but it would limit the analysis potential. Three discrete simulation sets were produced with HNL masses of 0.3 GeV, 0.6 GeV and 1.0 GeV. Each set consist of a part that is generated for very short decay lengths and one for long decay lengths, because during development it became clear that the low lengths component is crucial to get a reasonable event estimate. The remaining sampling distributions are identical for all sets and are listed in Table 4.4. The target number of events for each set was 2.5×10^9

Table 4.4: Generation level sampling distributions and ranges/values of the model dependent simulation sets.

Variable	Distribution	Range/Value
energy	E^{-2}	[2 GeV, 1×10^4 GeV]
zenith	uniform (in $\cos(\theta)$)	[80° , 180°]
azimuth	uniform	[0° , 360°]
vertex x, y	uniform	$r=600$ m
vertex z	uniform	-600 m to 0 m
m_4	fixed	[0.3, 0.6, 1.0] GeV
L_{decay}	L^{-1}	[0.0004, 1] m / [1, 1000] m

4.2.3 Weighting Scheme

To produce physically correct event distributions based on the arbitrary generation sampling distributions for the HNL simulation, the forward folding method that was already introduced for the SM simulation in Section ?? is used again. How this will be applied in the analysis is discussed in Section 7.2. The weighting scheme that will be explained in the following is implemented in the IceCube low energy analysis framework PISA, which will be discussed in Section 7.2.1. The custom weighting scheme is implemented in this custom stage. The only needed input is the mixing strength $|U_{e4}|^2$, which is the variable physics parameter in this analysis. This weighting is needed to go from the used decay length sampling distribution (inverse $1/L$ with fixed range in lab frame) to the target distribution (exponential defined by proper lifetime of the HNL). For each event the additional weight is calculated using the gamma factor

$$\gamma = \frac{\sqrt{E_{\text{kin}}^2 + m_4^2}}{m_4}, \quad (4.13)$$

with the HNL mass m_4 and it's kinetic energy E_{kin} . The speed of the HNL is calculated as

$$v = c \cdot \sqrt{1 - \frac{1}{\gamma^2}}, \quad (4.14)$$

where c is the speed of light. With these the lab frame decay length range $[s_{\min}, s_{\max}]$ can be converted into the rest frame lifetime range $[\tau_{\min}, \tau_{\max}]$ for each event

$$\tau_{\min/\max} = \frac{s_{\min/\max}}{v \cdot \gamma}. \quad (4.15)$$

The proper lifetime of each HNL event can be calculated using the total decay width Γ_{total} from Section 1 and the chosen mixing strength $|U_{\tau 4}|^2$ as

$$\tau_{\text{proper}} = \frac{\hbar}{\Gamma_{\text{total}}(m_4) \cdot |U_{\tau 4}|^2}, \quad (4.16)$$

where \hbar is the reduced Planck constant. Since the decay lengths or lifetimes of the events are sampled from an inverse distribution instead of an exponential, as it would be expected from a particle decay, we have to re-weight accordingly to achieve the correct decay lengths or lifetimes distribution. This is done by using the wanted exponential distribution

$$\text{PDF}_{\text{exp}} = \frac{1}{\tau_{\text{proper}}} \cdot e^{\frac{-\tau}{\tau_{\text{proper}}}}, \quad (4.17)$$

and the inverse distribution that was sampled from

$$\text{PDF}_{\text{inv}} = \frac{1}{\tau \cdot (\ln(\tau_{\max}) - \ln(\tau_{\min}))}. \quad (4.18)$$

This re-weighting factor is then calculated as

$$w_{\text{lifetime}} = \frac{\text{PDF}_{\text{exp}}}{\text{PDF}_{\text{inv}}} = \frac{\Gamma_{\text{total}}(m_4) \cdot |U_{\tau 4}|^2}{\hbar} \cdot \tau \cdot (\ln(\tau_{\max}) - \ln(\tau_{\min})) \cdot e^{\frac{-\tau}{\tau_{\text{proper}}}}. \quad (4.19)$$

Adding another factor of $|U_{\tau 4}|^2$ to account for the mixing at the interaction vertex the total re-weighting factor becomes

$$w_{\text{total}} = |U_{\tau 4}|^2 \cdot w_{\text{lifetime}}. \quad (4.20)$$

If this additional weighting factor is multiplied to a generation weight (like in Equation 5.1), the livetime, and the oscillated primary neutrino flux, it results in the number of expected events in the detector for this particular MC event for a chosen mixing (and mass).

add table with number of gen level files? mention the event number is smaller because of kinematic condition?

4.2.4 Generation Level Distributions

Figure 4.6 shows some selected generation level distributions. Additional distributions can be found in Figure A.3.

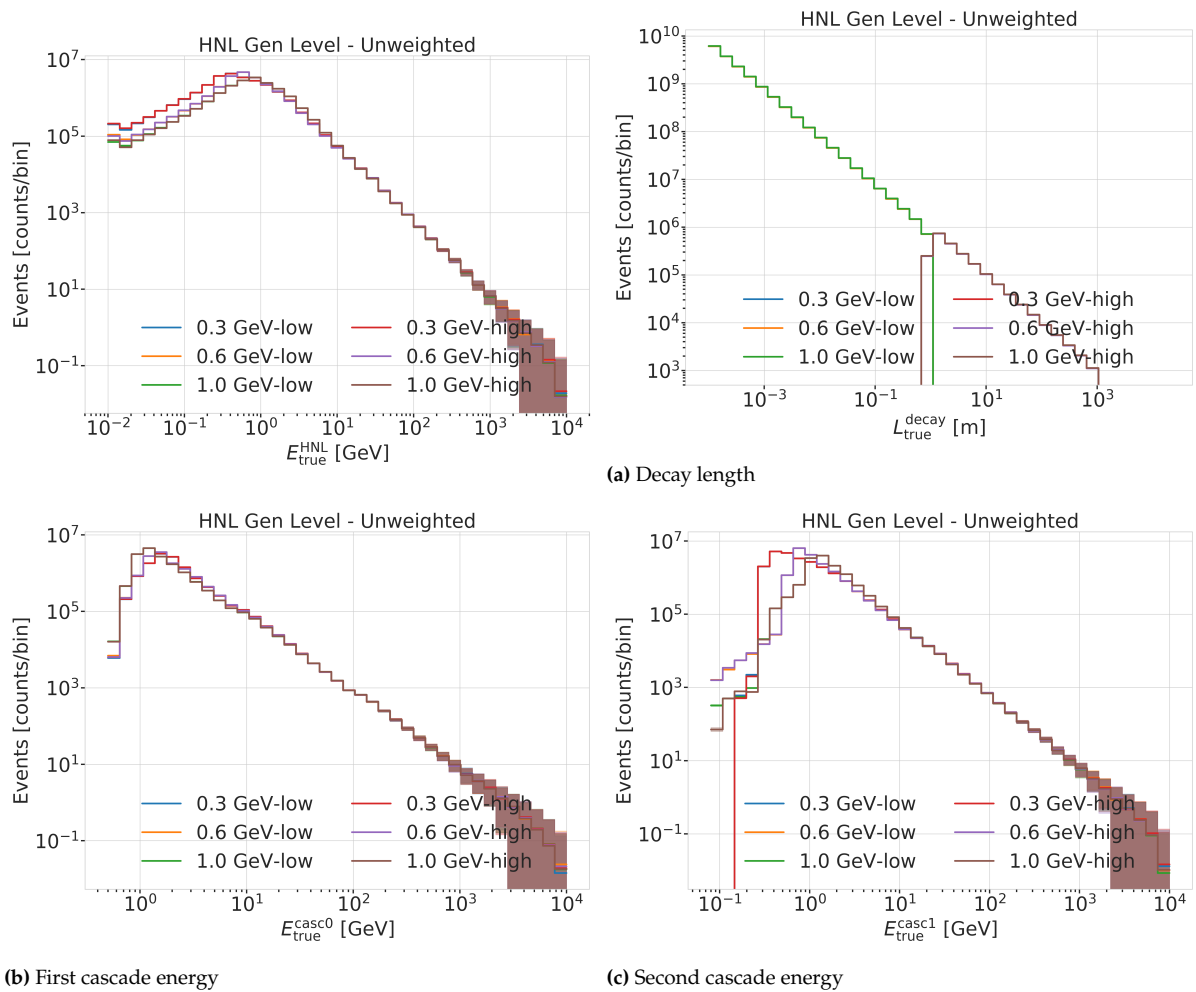


Figure 4.6: Generation level distributions of the model dependent simulation.

maybe increase main text width? (read in kao docu)

Adapt to reflect switched chapter order

Standard Model Background Simulation and Data Processing

5

The analysis presented in this thesis is highly dependent on an efficient event selection to reduce the raw IceCube trigger data to a usable atmospheric neutrino sample. Based on this selection, a precise estimation of both expected SM background and expected BSM signal events can be made using MC simulations. This chapter describes the current simulation and event selection chain used for state-of-the-art IceCube neutrino oscillation measurements like [55]. The whole chain can be broadly split into 4 steps:

Step 1 Event Generation: The initial step for all particle (non-noise) simulation is the generation of events from selected initial distributions and fluxes. Events are the primary particle and the particles produced in the interaction with the ice.

Step 2 Detector Simulation: The particles from the first step are propagated through the ice, producing Cherenkov photons, which are then propagated further until they reach a DOM or are absorbed. If they hit a DOM the detector response (acceptance and PMT) is simulated.

Step 3 Processing: Starting from the PMT output, both real data and simulation are processed through the in-ice trigger, the online filter and processing, and the low energy event selection to produce a neutrino dominated sample.

Step 4 Reconstruction: Once the sample is small enough for more sophisticated reconstruction techniques to be feasible to run, the events are reconstructed using a CNN and some high level variables are computed. Based on these variables the final event selection is applied.

This chapter only describes the event generation for the SM background simulation (neutrinos and muons), while the signal simulation is described in Chapter 4. The detector simulation is identical for both signal and background events while processing and reconstruction are applied to all simulation and data in the same way. Splitting the simulation steps has the advantage of reusing the outputs of for example the generation step to propagate the particles with different ice model, in order to estimate the systematic impacts of uncertainties of the ice properties. Similar approach can be taken for varying detector response and through this a more efficient (reduced) use of computing resources can be achieved. The following sections describe the different steps in more detail and the last section, Section 5.5, describes the related systematic uncertainties considered for this work.

5.1 Event Generation

The MC is used in the analysis by applying a method called *forward folding*, where a very large number of events (signal and background) is produced using sampling distribution that are tuned to have a large selection efficiency. Those distributions don't have to be physically correct

5.1	Event Generation	37
5.2	Detector Simulation	39
5.3	Processing	41
5.4	Reconstruction	45
5.5	Systematic Uncertainties	47

[55]: Abbasi et al. (2023), "Measurement of atmospheric neutrino mixing with improved IceCube DeepCore calibration and data processing"

Table 5.1: Cylinder volumes used for GENIE neutrino simulation generation. Cylinder is always centered in DeepCore at $(x, y, z) = (46.29, -34.88, -330.00)$ m.

Flavor	Energy [GeV]	Radius [m]	Length [m]	Events/File	Files
$\nu_e + \bar{\nu}_e$	1-4	250	500	450000	
	4-12				
	12-100	350	600	100000	650
	100-10000	550	1000	57500	
$\nu_\mu + \bar{\nu}_\mu$	1-5	250	500	408000	
	5-80	400	900	440000	
	80-1000	450		57500	1550
	1000-10000	550	1500	6700	
$\nu_\tau + \bar{\nu}_\tau$	1-4	250	500	1500000	
	4-10			300000	
	10-50	350	600	375000	350
	50-1000	450	800	200000	
	1000-10000	550	1500	26000	

distributions, but they need to cover the full parameter space of interest for the analysis. To produce a physical distribution, the events are weighted given a specific choice of physics and nuisance parameters. The large number of raw MC events ensures a good estimation of the expected numbers and weighted distributions.

The analysis itself is then performed by comparing the weighted MC distributions to the observed data. This is done by binning them as described in Chapter 7 and calculating a loss function comparing the bin expectations to the data. The physics and nuisance parameters that best correspond to the observed data are estimated by minimizing this loss function. In order to achieve a reliable result with this method the MC needs to be precise and as close to the data as possible (at least at the final event selection).

5.1.1 Neutrinos

Due to the very low interaction rate of neutrinos, the event generation is performed in a way that forces every event to interact in a chosen sampling volume. The weight of each event is then calculated as the inverse of the simulated neutrino fluence

$$w = \frac{1}{F_{\text{sim}}} \frac{1}{N_{\text{sim}}}, \quad (5.1)$$

where F_{sim} is the number of neutrino events per energy, time, area, and solid angle and N_{sim} is the number of simulated events. If this weight is multiplied by the livetime and the theoretically expected neutrino flux for a given physical model, it results in the number of expected events in the detector for this particular MC event. The baseline neutrino flux used in this thesis, computed for the South Pole, is taken from Honda *et al.* [21].

The simulation volume is a cylinder centered in DeepCore with radius and height chosen such that all events possibly producing a signal are contained. The different sizes, chosen depending on energy and neutrino flavor, are shown in Table 5.1. The directions of the neutrinos are sampled

[21]: Honda et al. (2015), “Atmospheric neutrino flux calculation using the NRLMSISE-00 atmospheric model”

isotropically and the energies are sampled from an E^{-2} power law. The number of simulated events is chosen such that the livetime is more than 70 years for each flavor. Neutrinos and antineutrinos are simulated with ratios of 70% and 30%, respectively.

To simulate the neutrino interaction with the ice, the GENIE event generator [56] (version 2.12.8) is used, resulting in the secondary particles and the kinematic and cross-section parameters. As input, the outdated GRV98LO [57] *parton distribution functions (PDFs)* was used, because it was the only option that could incorporate extrapolations to lower Q^2 [58]. Muons produced in these interactions are propagated using PROPOSAL [59], also simulating their Cherenkov light output. The shower development of gamma rays, electrons, and positrons below 100 MeV and hadronic showers below 30 GeV is simulated using Geant4 [47] while for higher energies an analytical approximation from [44] is used.

5.1.2 Muons

Atmospheric muons are generated on a cylinder surface enclosing the full IceCube detector array. The cylinder has a height of 1600 m and a radius of 800 m. The energy is sampled from an E^{-3} power law while the other sampling distributions (position, direction) are found from parameterizations based on [60]. This work uses full CORSIKA [61] simulations of muons to tailor the parameterizations, starting from *cosmic ray (CR)* interactions with atmospheric nuclei using the CR flux model from [62] and producing the muons applying the *hadronic interaction (HI)* model SIBYLL 2.1 [63]. After the generation, they are propagated through the ice with PROPOSAL producing photons, treating them exactly like the muons produced in neutrino interactions.

Since the offline processing and selection steps described in Section 5.3.2 and Section 5.4 reduce the muon contamination to an almost negligible level, the statistical uncertainty on the number of expected muon events at the final selection level is large and therefore two separate sets of muon simulation are produced. A **first set** including all events resulting from the above described generation to tune the lower level selection (up to L4) and a **second set** to estimate the muon contamination at higher levels (above L5), which only accepts muon events if they pass through a smaller cylinder centered in DeepCore (height of 400 m and radius of 180 m) and rejects events based on a KDE estimated muon density at L5 (in energy and zenith) increasing the simulation efficiency at L5 significantly.

[56]: Andreopoulos et al. (2015), “The GENIE Neutrino Monte Carlo Generator: Physics and User Manual”

[57]: Glück et al. (1998), “Dynamical parton distributions revisited”

[58]: Bodek et al. (2003), “Higher twist, xi(omega) scaling, and effective LO PDFs for lepton scattering in the few GeV region”

[59]: Koehne et al. (2013), “PROPOSAL: A tool for propagation of charged leptons”

[47]: Agostinelli et al. (2003), “Geant4—a simulation toolkit”

[44]: Rädel et al. (2012), “Calculation of the Cherenkov light yield from low energetic secondary particles accompanying high-energy muons in ice and water with Geant4 simulations”

[60]: Becherini et al. (2006), “A parameterisation of single and multiple muons in the deep water or ice”

[61]: Heck et al. (1998), “CORSIKA: A Monte Carlo code to simulate extensive air showers”

[62]: Gaisser (2012), “Spectrum of cosmic-ray nucleons, kaon production, and the atmospheric muon charge ratio”

[63]: Engel et al. (2017), “The hadronic interaction model Sibyll – past, present and future”

put a number on this significant increase?

5.2 Detector Simulation

The detector simulation is performed after the event generation, where the initial particles and the resulting photons and secondary particles from their propagation were produced. This part of the simulation chain is applied to all muon and neutrino simulation as well as the HNL signal simulation explained in detail in Chapter 4. The detector simulation can be split into two parts, the propagation of the photons and the simulation of the detector response (including internal noise).

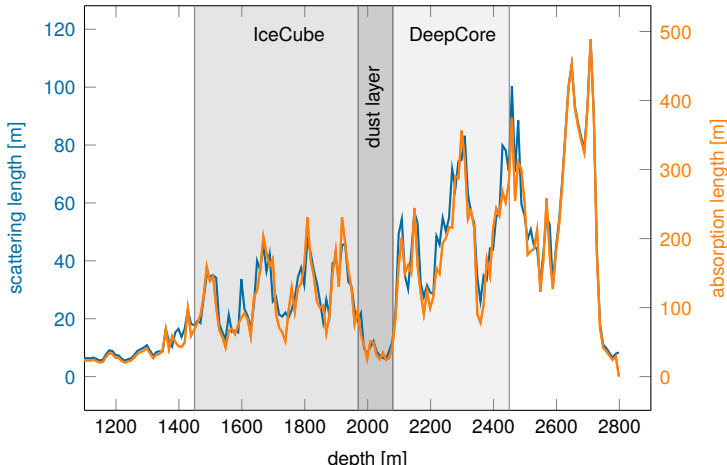


Figure 5.1: Scattering and absorption lengths in the SPICE model used for simulation production as a function of depth, modified from [67].

5.2.1 Photon Propagation

Any photon that was produced in the event generation is individually traced through the ice, simulating scattering and absorption processes. The propagation is done using `CLSIM` [64] which is an implementation of the *Photon Propagation Code (PPC)* [65] in OPENCL. It is optimized to be run very efficiently on GPUs, which is what is done for IceCube simulation production. The ice is modeled as a set of 10 m thick, almost horizontal layers with specific absorption and scattering lengths. The *South Pole ice (SPICE)* model [66] accounts for the layers being tilted by a small amount () and the absorption and scattering lengths having a non-uniformity with respect to the azimuth direction. Figure 5.1 shows the values of this model for the different depths, indicating the location of IceCube, DeepCore, and the dust layer.

In an initial step, each photon's absorption length is sampled from an exponential distribution with the expectation value at the current layer's absorption length. The following propagation steps are performed in parallel for all photons. In each of those steps, corresponding to a single scattering event, the photon travels a length that is sampled from an exponential distribution with the expectation value at the scattering length of the current layer and the scattering angle chosen based on a combination of a simplified Mie scattering distribution [68] and a Henyey-Greenstein distribution [69]. The parameters defining the shape of these distributions were calibrated using data from *in-situ* LED calibration runs. These steps are continuously repeated until each photon reached a DOM or was absorbed¹. After all photons have been propagated in that manner, the final step is to output the photons that reached a DOM for further processing.

5.2.2 Detector Responses

The second part of simulating the IceCube detector is the DOM response. Whether a photon that reached a DOM produces a signal depends on the total efficiency and the angular acceptance curve of the specific DOM. The total efficiency includes effects of the DOM glass, PMT quantum and photo-electron collection efficiencies, and it is wavelength dependent. Additionally, there is another angle dependent effect called *hole ice* [70].

[65]: Chirkin et al. (2019), "Photon Propagation using GPUs by the IceCube Neutrino Observatory"

[66]: Aartsen et al. (2013), "Measurement of South Pole ice transparency with the IceCube LED calibration system"

put a number on the tilt angle?

[68]: Mie (1908), "Beiträge zur Optik trüber Medien, speziell kolloidaler Metallösungen"

[69]: Henyey et al. (1941), "Diffuse radiation in the Galaxy."

1: A photon is absorbed, when it traveled its full absorption length, sampled in the initial step of the photon propagation.

[70]: Fiedlschuster (2019), "The Effect of Hole Ice on the Propagation and Detection of Light in IceCube"

This effect is due to varied ice properties resulting from the re-freezing process of the water column inside the borehole after deployment of the string. Accepted photons are converted into a so-called *Monte Carlo photo-electron (MCPE)*. The amount of charge measured for each MCPE is determined by sampling from a mixture of two exponential distributions and a normal distribution. This *single photo-electron (SPE)* distribution was tuned to match the observed distribution in each DOM in an *in-situ* calibration study [71]. Figure ?? shows the distribution compared to a lab measurement. Based on the sampled charges and times of MCPEs, the voltage waveforms for the (two) different readout channels are simulated and passed on to the trigger simulation starting with *WaveDeform*, which was already mentioned in Section 3.1.1.

Besides the Cherenkov photons, IceCube also observes photons that are produced in radioactive decays inside the DOMs, both in the glass housing sphere and the PMT glass itself. To simulate this internal noise, the *Vuvuzela* module [72, 73] is used to create additional MCPEs that are fed into the same simulation chain described above. This module takes into account thermal and non-thermal components and their times are sampled using parameterizations of the measured distributions, where the thermal noise component is uncorrelated photons and the non-thermal component is from burst of photons. The noise hits are simulated by drawing the times from a constant rate Poisson process and the number of photons from a Poisson distribution. Then the time differences between the individual photons per hit is found, based on a Log-Normal distribution. The simulation is defined by 5 parameters that are calibrated for each DOM individually. Table 5.2 shows the average values for these parameters.

[71]: Aartsen et al. (2020), "In-situ calibration of the single-photoelectron charge response of the IceCube photomultiplier tubes"

Add SPE distribution plot

Parameter	Value
Therm. rate λ_{th}	180 Hz
Decay rate λ_{dec}	80 Hz
Decay hits η	8.5
Decay μ	$4.3 \log_{10}(\text{ns})$
Decay σ	$1.8 \log_{10}(\text{ns})$

Table 5.2: Typical parameter values used in the vuvuzela noise simulation. Averaged over all DOMs.

[72]: Larson (2013), "Simulation and Identification of Non-Poissonian Noise Triggers in the IceCube Neutrino Detector"

[73]: Larson (2018), "A Search for Tau Neutrino Appearance with IceCube-DeepCore"

5.3 Processing

After the detector simulation is performed, all MC and data are processed in exactly the same way. This section explains the trigger and event selection that is applied starting from the raw voltage measured by the PMTs. Most parts of this processing are identical to the procedure already described in [67, 74]. It is split in different steps run inside the ice, at the South Pole, and after the data was transferred to the North. The complexity and computational cost of the processing increases with each step, while the total number of events reduces, making it feasible and reducing the use of computational resources on events that are not of interest for the analysis.

[67]: Trettin (2023), "Search for eV-scale sterile neutrinos with IceCube DeepCore"

[74]: Lohfink (2023), "Testing nonstandard neutrino interaction parameters with IceCube-DeepCore"

5.3.1 Trigger and Filter

Before the data can be sent to the North, the initial signal coming from the PMT (for data) or from the detector response simulation (for MC) is a voltage waveform, which has to be digitized and information of photon hits has to be extracted. The trigger and filter explained here are tailored to select events that passed through the DeepCore volume, while rejecting background events (either from atmospheric muons or from random noise). There are other filters used in IceCube which will not be explained here, since they are not relevant for this work. A full

AT: Das klingt so, als würde die MC Simulation ein analoges Signal erzeugen, was auch digitalisiert wird. Vllt kann man das nochmal nachforschen, aber zumindest in meiner Arbeit habe ich geschrieben, dass die MCPEs direkt in ATWD und fADC Readouts umgewandelt werden.

[75]: Aartsen et al. (2017), “The IceCube Neutrino Observatory: Instrumentation and Online Systems”

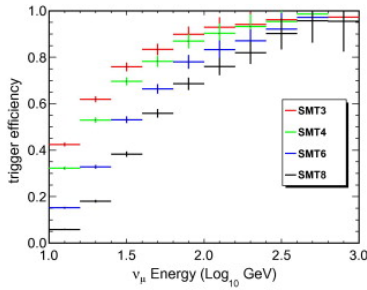


Figure 5.2: Efficiencies of different IceCube and DeepCore triggers, taken from [40].

[36]: Abbasi et al. (2009), “The IceCube data acquisition system: Signal capture, digitization, and timestamping”

[6]: Aartsen et al. (2017), “The IceCube Neutrino Observatory: instrumentation and online systems”

[40]: Abbasi et al. (2012), “The design and performance of IceCube DeepCore”

description of the instrumentation and the online systems can be found in [75].

In-ice Trigger

The trigger is applied inside the DOM in the ice before sending the information to the ICL on the surface. The time dependent voltage curves are captured if a pre-defined threshold value is exceeded. Once the threshold set to the equivalent of 0.25 PE is crossed, 6.4 μ s of the waveform are coarsely digitized by a *Fast Analog-to-Digital Converter* (*FADC*) with a sampling rate of 40 MHz. Additionally, the first 427 ns are digitized using an *Analog Transient Waveform Recorder* (*ATWD*) with a sampling rate of 300 MHz [36], but only if some trigger condition is met, because this readout frequency is too high to be sampled directly and requires some buffering. For DeepCore, the HLC condition already mentioned in Section 3.1.1 has to be met for three DOMs inside the fiducial volume within a time window of 5 μ s. If this is the case, all waveforms that crossed the threshold within a 20 μ s time window around the trigger are digitized and sent to the ICL for further processing. This trigger is called *Simple Multiplicity Trigger 3* (*SMT-3*). The DOM hits that are read out in this process, but do not meet the HLC condition, are called *soft local coincidence* (*SLC*) hits. The rate of the DeepCore SMT-3 trigger is \sim 250 Hz [6], accepting \sim 70 % of ν_μ -CC events at 10 GeV and \sim 90 % at 100 GeV [40]. The trigger efficiencies for different SMT triggers, including the DeepCore SMT-3, are shown in Figure 5.2.

Online Filter

2: Where *online* means running on hardware at the South Pole.

The digitized waveforms are sent to the ICL, where a further filter is applied *online*². First, the WaveDeform algorithm is run to extract photon arrival times and charge from the waveforms, then the DeepCore filter is applied, which is an iterative hit cleaning starting from HLC hits and removing any hits outside a 125 m radius and a 500 ns time window (called *radius-time cleaning* (*RT-cleaning*)) of the initial hit. This mainly rejects unphysical SLC hits, which are potentially caused by random noise. The following selection steps are done using the resulting cleaned pulses.

Next, an additional cut is applied to reject events that are likely to be caused by atmospheric muons. This is done by splitting the hits depending on whether they were inside the DeepCore fiducial volume or outside and then calculating the speed of each hit outside the fiducial volume towards the *center of gravity* (*COG*) of the hits inside. If one of them has a speed close to the speed of light, the whole event is rejected, because this is a strong indication for a muon event.

As input for the further selection levels, a few event properties, like vertex position and direction, are determined using fast and simple event reconstructions. After the DeepCore online filter, the rate is about 15 Hz, which can be sent to the North via satellite for further processing.

5.3.2 Event Selection

After the data was sent to the North, the *offline* filters and selection are applied to further reduce the background of atmospheric muons and noise. The selection is split into three levels referred to as *Level 3-5* (*L3-L5*), which bring down the neutrino and muon rate to ~ 1 mHz, while the remaining fraction of random noise is below 1 %.

Level 3

At the first offline filtering level, Level 3, 1D cuts are used to reduce atmospheric muons, pure noise, and coincident muons. These cuts are targeting regions where the data/MC agreement is poor, so that more sophisticated *machine learning* (ML) techniques can be applied at later levels. The cuts are made using 12 control variables, that are inexpensive to compute for the very large sample at this stage. The variables are related to position, time, and overall number of hits in the event.

Pure noise hits, that are temporally uncorrelated, are cleaned by applying a 300 ns sliding window, requiring the containment of more than 2 hits at its maximum. Additionally, an algorithm is run to check whether the hits show some directionality, accepting them only if they do.

To reduce the amount of muons a series of cuts is applied using spatial and temporal information. Events that have more than 9 hits observed above -200 m or the first HLC hit above -120 m are rejected as well as events where the fraction of hits in the first 600 ns of the event is above 0.37, ignoring the first two hit DOMs. Additionally, the ratio between hits in the veto region and the DeepCore fiducial volume is required to be below 1.5.

If a muon enters the detector after the data acquisition was already triggered, it causes events that span over a much larger time range. To reduce those coincident events, the time difference between first and last pulse cannot be above 5000 ns. This cut mainly affects a region of very poor data to MC agreement, because coincident events are not simulated at all.

The L3 cuts remove 95 % of the atmospheric muons and >99 % of pure noise hits, while keeping >60 % of the neutrino events. The sample now roughly contains muons/neutrinos/noise at a ratio of 100:10:1 with a total rate of ~ 0.5 Hz.

add example plots (?) for L3 cut variables and applied cuts

Level 4

After the total rate was reduced by the simple cuts of L3 and the overall agreement between data and MC is established, ML techniques can be applied to further reduce the background. For Level 4, two *Boosted Decision Trees* (BDTs) [76] classifier are trained to separate neutrino events from atmospheric muons and noise hits, separately. The output of each classifier, a probability score, can be seen in Figure 5.3. The noise filter is applied first and an event passes the score if it is larger than 0.7, reducing the noise hits by a factor of 100, while keeping 96 % of neutrinos. Then the second BDT classifier is applied to reject muons. It was trained partly

[76]: Friedman (2002), “Stochastic gradient boosting”

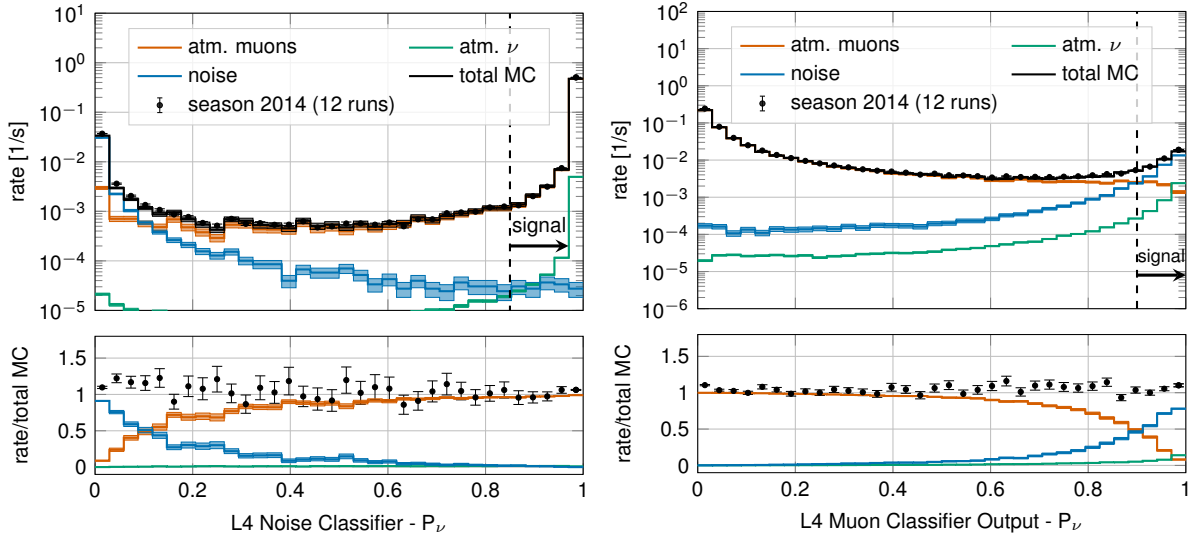


Figure 5.3: Distributions of Level 4 noise classifier output (left) and muon classifier output (right), where larger values indicate more neutrino-like and lower values more noise-like/muon-like. Taken from [55].

on unfiltered data, which consists of >99 % atmospheric muons, to reject the data and keeping the neutrinos from the simulation. Rejecting events with a score smaller than 0.65 removes 94 % of atmospheric muons while keeping 87 % of neutrinos. This fraction varies depending on the flavor and interaction type, ν_μ -CC events for example, which have a muon in the final state, are therefore reduced to 82.5 %. After applying the L4 cuts based on the BDT classifier outputs, the sample is still dominated by atmospheric muons, while the noise rate dropped to below most neutrino types.

Level 5

add some figure showing the corridors?

Level 5 is the final selection level, before event reconstructions are applied. This level aims to reduce the remaining atmospheric muon rate below the rate of neutrinos. Muons not rejected by the earlier levels are those that produced little or no light in the veto regions. One possible reason is that they passed through one of the un-instrumented regions between the strings called *corridors*. To reject those, special corridor cuts, based on the number of hits they produced close to a potential corridor they passed through. The potential corridor in question is identified based on a simple infinite track fit. In addition to the corridor cuts, starting containment cuts are applied to reject events that start at the edge of the fiducial volume. Events with more than seven hits in the outermost strings of the detector or those that have a down going direction in the uppermost region are rejected. This further reduces the fraction of muons by 96 % while keeping 48 % of neutrinos. The rates after this level are 1 mHz and 2 mHz for neutrinos and muons, respectively, making it a neutrino dominated sample.

add table with rates per level (split in flavor) - maybe better in analysis chapter to also show signal?

5.4 Reconstruction

In the energy range most relevant for this work, between 10 GeV and 100 GeV, the light deposition is very low and only a few DOMs detect light, making the reconstructions difficult. In [77] two classical methods are described, which have partly been applied in one recent IceCube atmospheric neutrino oscillation measurement using a sub-sample of the DeepCore sample [55]. The algorithm used in this work on the other hand, is a newer method that applies a *convolutional neural network (CNN)* to reconstruct the events and determine some discriminating quantities. The latest muon neutrino disappearance result from IceCube [78] is based on this reconstruction.

[77]: Abbasi et al. (2022), “Low energy event reconstruction in IceCube DeepCore”

[55]: Abbasi et al. (2023), “Measurement of atmospheric neutrino mixing with improved IceCube DeepCore calibration and data processing”

[78]: Yu et al. (2023), “Recent neutrino oscillation result with the IceCube experiment”

5.4.1 Fast Low Energy Reconstruction using Convolutional Neural Networks

As the name *Fast Low Energy Reconstruction using Convolutional Neural Networks (FLERCNN)* already indicates, the FLERCNN reconstruction [79, 80] is a CNN optimized to reconstruct IceCube events at low energies (<100 GeV) in a fast and efficient manner, by leveraging the approximate translational invariance of event patterns within the detector. The architecture of the network is very similar to the preexisting IceCube CNN event reconstruction [81], but optimized on low energy events and specifically tailored to include the DeepCore sub-array. Only the eight DeepCore strings and the central 19 IceCube strings are used for the reconstruction (compare to Figure 3.4). Because of the different z-positions of the DeepCore and IceCube DOMs, they are divided into two networks that are combined in the final layer of the network. The full architecture is shown in Figure 5.4. The first dimension of the network is the string index, while the second dimension is the order of the DOMs along the vertical axis. The horizontal position of the DOMs is not used, since the strings are arranged in an irregular pattern. The information from the DOM hits is summarized into five charge and time variables, which make up the last dimension of the input layer. The variables are the total summed charge, the time of the first hit, the charge weighted mean time of the hits, the time of the last hit, and the charge weighted standard deviation of the hit times.

[79]: Yu et al. (2021), “Direction reconstruction using a CNN for GeV-scale neutrinos in IceCube”

[80]: Micallef ()

[81]: Huenefeld (2017), “Deep Learning in Physics exemplified by the Reconstruction of Muon-Neutrino Events in IceCube”

add image with selected strings used for flercnn IC and DC

add some performance plots of the FLERCNN reconstruction

There is more information on pre-processing the samples and preparing the input features, and training each cnn, but I'm not sure if that might be too much detail?

Five different networks are trained using this architecture. Three networks do the regression of the events’ energy, zenith angle, and the starting vertex (x, y, z position), while two of them are used for classification. One is trained to predict the probability of the event being a track (used as PID) and the other to predict the probability of the event being a muon. Each network is trained with an MC sample modified to have a flat distribution in the target variable, to be unbiased for that variable and ideally extending outside the target reconstruction region. For the classification tasks the loss function is the *binary cross entropy* and the activation function is a *sigmoid*. To perform the regression of zenith and vertex position, the loss function is the *mean squared error (MSE)*, while for the energy it is the *mean absolute percentage error*. The activation for all regression tasks is *linear*.

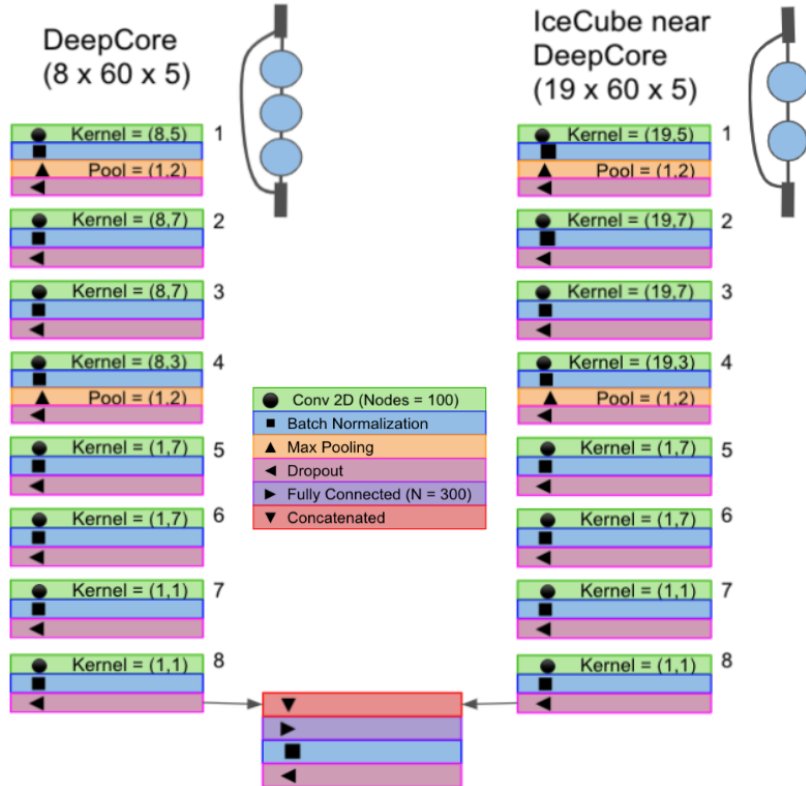


Figure 5.4: Architecture of the FLERCNN neural networks, taken from [79].

5.4.2 Analysis Selection

Before the reconstruction is applied a few additional high level variables are computed, which are from fast and inexpensive algorithms. Then the reconstruction is performed by applying the trained FLERCNN networks to get the output quantities. After that, another BDT classifier is trained to further reduce the muon background for the final sample. The BDT is trained on five high level variables, where three are FLERCNN reconstruction variables (vertex z , ρ_{36}^3 , and muon probability) and two are lower level variables (L4 muon classifier output and L5 corridor cut variable). To train the BDT, the FLERCNN nominal simulation set is used, only using events with $\cos(\theta_{\text{zenith}}) \leq 0.3$. The output of the BDT is the neutrino probability and a cut at 0.8 is applied to reject events with a high probability of being a muon. Figure 5.5 shows the output of the BDT classifier, where the neutrinos in both training and testing sets are gathered at 1 and muons are around 0, which shows great classification power.

To get the final, pure sample of well reconstructed neutrinos another set of cuts is applied. The first cuts are meant to reject events with poor reconstruction quality, by requiring the events to fall into the DeepCore volume, where the denser, better instrumented detector leads to enhanced resolution. The cuts are applied on the vertex z and ρ_{36} and are listed in Table 5.3. The FLERCNN reconstruction was optimized for atmospheric neutrino analyses which are mainly in the region below 100 GeV and there are very few events with energies below 5 GeV, so the reconstructed energy is required to be in that range. Additionally, rejecting events with fewer than seven hits in the selected DOMs used for FLERCNN showed to increase the resolution.

add reference for flercnn analysis internal note

3: A radial variable that is often used in IceCube, is the horizontal distance to string 36 called ρ_{36} , which is basically the distance to the center of IceCube.

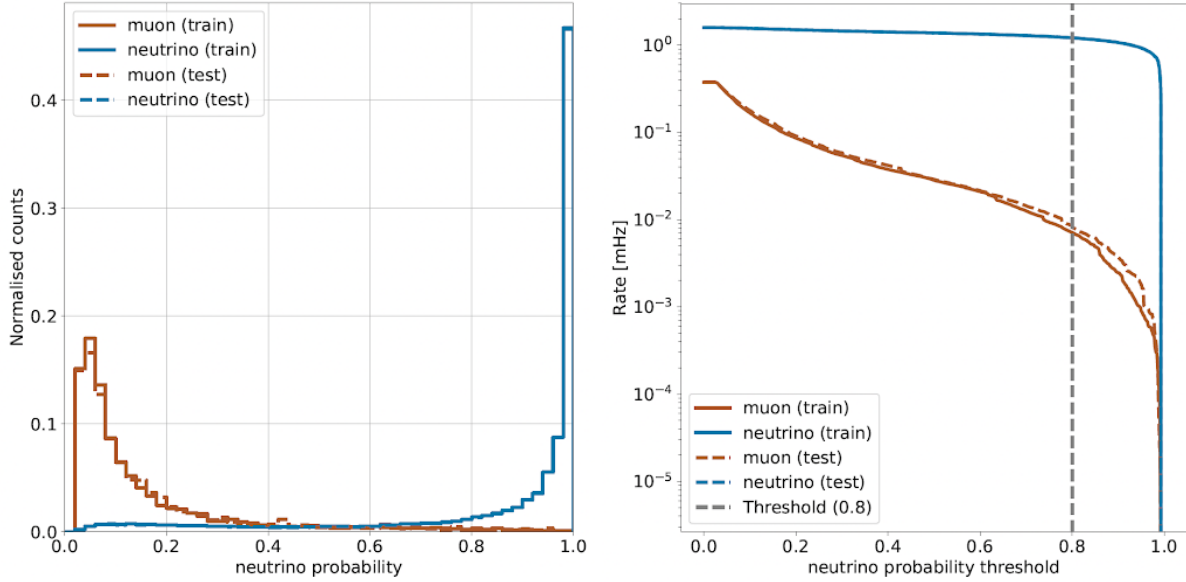


Figure 5.5: FLERCNN muon classifier output score (left) and rate of neutrinos and muons as function of muon classifier cut (right). Taken from [\[flercnn_analysis_internal_note\]](#)

Variable	Threshold	Removed
Number of hit DOMs	≥ 7	1.05 %
Radial distance	$< 200 \text{ m}$	0.09 %
Vertical position	$-495 \text{ m} < z < -225 \text{ m}$	5.48 %
Energy	$5 \text{ GeV} < E < 100 \text{ GeV}$	20.70 %
Cosine of zenith angle	< 0.04	19.66 %
Number of direct hits	> 2.5	10.50 %
Number of hits in top layers	< 0.5	0.03 %
Number of hits in outer layer	< 7.5	0.001 %
Muon classifier score	≥ 0.8	23.90 %

Table 5.3: Cuts performed to select the final analysis sample. Parts of the cuts are meant to increase the data/MC agreement, while others are meant to reject events with poor reconstruction quality.

Another set of cuts is applied to make sure the agreement between data and MC is good. To remove coincident muon and neutrino events, cuts are applied to the number of hits in the top 15 layers of IceCube DOMs and the number of hits in the outermost IceCube strings. Coincident random noise events are removed by requiring more than three hit DOMs from direct photons⁴. Neither of the two coincident event types are simulated, which can be seen as bad agreement between data and MC. The last cut is on the reconstructed cosine zenith, which is required to be smaller than 0.04 to reject down-going muons.

4: Direct photons are photons that were not scattered on their way from the interaction vertex to the DOM.

add final sample composition, but maybe also in analysis chapter to show signal and background?

at some place I will want a selection efficiency plot for SM BG and HNL signal, but I'm not sure where to put it yet

5.5 Systematic Uncertainties

There are multiple sources of systematic uncertainties related to the event generation and processing explained in this chapter. All uncertainties considered in this work are implemented with parameters that can be varied continuously so that a simultaneous fit of the physics and systematic parameters can be performed. Where possible, a correct model of the effect is used, but in many cases the variations are captured by effective parameters. Uncertainties that solely scale the total event rate are not included individually, since the analysis only uses the relative

distribution of events. A single scaling parameter A_{eff} is used to scale the total neutrino rate instead.

5.5.1 Atmospheric Flux Uncertainties

The flux of atmospheric neutrinos is influenced by multiple factors, the spectrum and composition of CRs, the assumed atmospheric conditions, and the HI model used to describe the air showers development. Uncertainties of the neutrino flux are therefore dictated by the uncertainties on these components, where the variations in atmospheric conditions were found to have negligible effect [55].

[55]: Abbasi et al. (2023), "Measurement of atmospheric neutrino mixing with improved IceCube DeepCore calibration and data processing"

[82]: Dembinski et al. (2017), "Data-driven model of the cosmic-ray flux and mass composition from 10 GeV to 10^{11} GeV"

[83]: Barr et al. (2006), "Uncertainties in atmospheric neutrino fluxes"

[84]: Evans et al. (2017), "Uncertainties in atmospheric muon-neutrino fluxes arising from cosmic-ray primaries"

[55]: Abbasi et al. (2023), "Measurement of atmospheric neutrino mixing with improved IceCube DeepCore calibration and data processing"

[86]: Barr et al. (2006), "Uncertainties in Atmospheric Neutrino Fluxes"

add figure with Barr blocks?

[87]: Riehn et al. (2020), "Hadronic interaction model sibyll 2.3d and extensive air showers"

[82]: Dembinski et al. (2017), "Data-driven model of the cosmic-ray flux and mass composition from 10 GeV to 10^{11} GeV"

5: The choice of flux and HI model have minor impact on the variations.

Cosmic ray flux: The selected sample of atmospheric neutrinos lies around energies of up to 100 GeV. The initial primary particles in the CR flux can have 100 times larger energies and therefore the CR flux between 10 GeV and 10 TeV is important, which dominantly consists of hydrogen and helium nuclei [82]. The uncertainty in this CR flux component can be described as a power law correction [83, 84]

$$\Phi'_\nu = \Phi_\nu \left(\frac{E}{E^*} \right)^{\Delta\gamma}, \quad (5.2)$$

where E^* is the pivot energy and $\Delta\gamma$ is the correction to the power law exponent. This modification propagates into the neutrino flux, which is therefore corrected in the same way. E^* was chosen to be 24 GeV as to minimize the dependence of the overall flux scale on $\Delta\gamma$ [55].

Hadronic interaction model: Neutrinos are produced in the decaying hadrons in CR air showers, spanning a large parameter space that is sparsely evaluated by experimental data. To include uncertainties based on energy, direction, and neutrino flavor, the MCEq package [85] is used to compute the distribution of atmospheric leptons and to estimate the impact of varying their contributions. The calculations result in the change in flux $d\Phi_1/dB$ for a variation dB of some parameter B . Scaling this variation by some value b , the modified total flux, s is then given by

$$\Phi'_1 = \Phi_1 + \left(b \cdot \frac{d\Phi_1}{dB} \right). \quad (5.3)$$

Matching the work in [86], the parameter space is divided in regions of the primary energy E_i and the energy fraction of the secondary meson x_{lab} , with varying uncertainties, derived from fixed target experiment data. The Sibyll2.3c [87] HI model and the GSF CR flux [82] were used to calculate the related flux changes⁵ for the different regions in E_i and x_{lab} , resulting in 17 variables, encoding the possible changes.

5.5.2 Cross-Section Uncertainties

The uncertainties related to the cross-sections are split into low and high energy components, since there is no coherent model to explain both DIS interactions, which are the dominant processes above 20 GeV, and *charged current resonance production* (CCRES) and *charged current*

quasi elastic scattering CCQE, which are relevant below 20 GeV where interactions with the nucleons as a whole are important. Three parameters are included to account for all relevant cross-sections uncertainties.

At low energies two parameters are included accounting for uncertainties in form factors of CCQE and CCRES events. These uncertainties are due to uncertainties in the *axial mass* M_A , which enters the form factor as in

$$F(Q^2) \sim \frac{1}{(1 - (\frac{Q}{M_A})^2)^2}, \quad (5.4)$$

where Q^2 is the momentum transfer squared. The axial mass can be determined experimentally and to include uncertainties on the values of M_A^{CCQE} and M_A^{CCRES} , the cross-sections are computed with GENIE, where the form factors are calculated varying the axial mass by $\pm 20\%(1\sigma)/\pm 40\%(1\sigma)$ around the nominal value. This is an approximation of the recommended uncertainties by the GENIE collaboration, which are -15% , $+25\%$ for M_A^{CCQE} and $\pm 20\%$ for M_A^{CCRES} [56]. To apply a continuous uncertainty variation of the axial mass in a fit, the total cross-section is fit with a quadratic function to interpolate between the cross-sections computed with the different axial masses.

which experiments measure the axial mass?

Even though the DIS interactions can be calculated very precisely, there are still uncertainties in the input PDF, describing the probability of finding a specific parton (quark) with a specific momentum fraction x inside a nucleon. To account for differences between the used method and more sophisticated methods using newer PDFs seen at high energies, an uncertainty parameter is introduced. The parameter is based on the discrepancy between the cross-sections computed with GENIE and the ones computed with CSMS [88] above 100 GeV. The included parameter scales the cross-section from the GENIE values to the CSMS values, which are considered more accurate above 100 GeV. The scaling is done as a function of energy and inelasticity and to guarantee continuity, the scaling is extrapolated linearly below 100 GeV. The parameter is designed such that a value of 0.0 corresponds to the GENIE cross-sections and a value of 1.0 gives an approximation of the CSMS cross-sections. A comparison of the total cross-sections GENIE (scaled/unscaled) with the data is shown in Figure 5.6.

[88]: Cooper-Sarkar et al. (2011), “The high energy neutrino cross-section in the Standard Model and its uncertainty”

5.5.3 Detector Calibration Uncertainties

There are multiple sources of systematic uncertainties related to the detection process of neutrinos in IceCube. Dominant for this analysis are the effects of the properties of the ice itself and the optical efficiency of the DOMs. None of these uncertainties can be described by an analytic expression, so they have to be estimated using MC simulation. The method used to derive the continuous variations based on the MC simulation is described in Section ???. The five relevant uncertainty parameters are the absolute efficiency of the DOMs, a global scaling of bulk ice scattering and absorption lengths, and variations of the relative angular acceptance due to hole ice variations in two parameters.

DOM efficiency: As was already mentioned in Section 3.1.1, the absolute efficiency of the DOMs, ϵ_{DOM} is calibrated using minimum ionizing

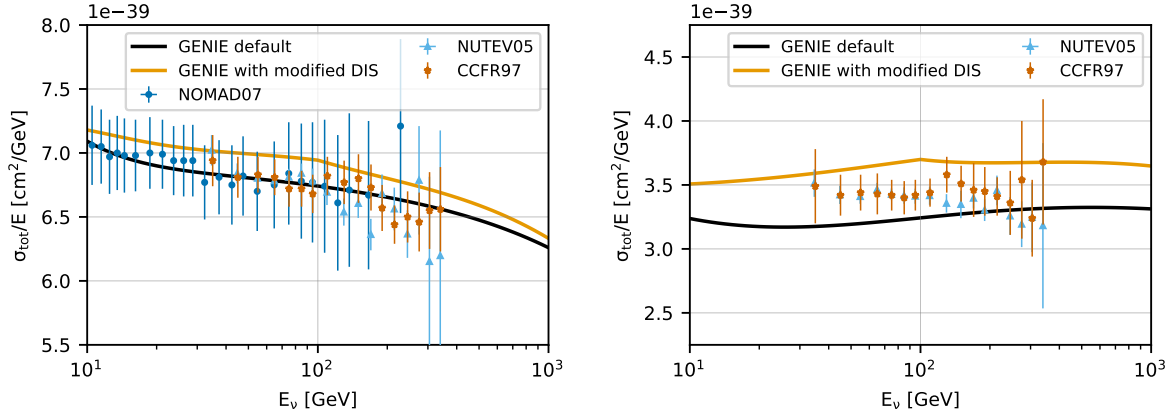


Figure 5.6: Inclusive total neutrino-nucleon cross-sections on an isoscalar target (black) for neutrinos (left) and antineutrinos (right) calculated with GENIE, comparing to measurements from NOMAD [89], NUTEV [90], and CCFR [91]. The scaled GENIE cross-section (orange) is also shown. Taken from [55].

[38]: Feintzeig (2014), “Searches for Point-like Sources of Astrophysical Neutrinos with the IceCube Neutrino Observatory”
[39]: Kulacz (2019), “In Situ Measurement of the IceCube DOM Efficiency Factor Using Atmospheric Minimum Ionizing Muons”

[92]: Rongen, Martin (2016), “Measuring the optical properties of IceCube drill holes”

6: The hole ice angular acceptance modification is normalized so that it does not affect the total charge.

muons from air showers, due to the lack of a calibrated light source in the detector. Using the muons as a steady, controlled source of light, the efficiency can be estimated by comparing simulated muon data sets with varied DOM response to the measured data. Since the uncertainties found in multiple iterations of this study [38, 39] are at the order of 10 %, this systematic is highly relevant and has to be included in the analysis.

Bulk ice scattering and absorption: Absorption and scattering length are the most important properties that govern the propagation of photons through the ice. The simulation principle and how the depth dependent absorption and scattering coefficients are used was already explained in Section 5.2.1. To account for uncertainties on this model of the bulk ice coefficients, a global scaling for each of the two parameters (global absorption, global scattering) is applied.

Hole ice angular acceptance: Due to bubble formation in the re-freezing process of the boreholes, the hole ice seems to be less transparent in the center of the columns [92]. This effectively decreases the chance of photons hitting the DOMs directly from below, which can be described as an additional angular modification of the DOM acceptance. The modification is parameterized by a two dimensional, normalized⁶ function, where the two dominant of the parameters (p_0, p_1), dictating its form, are enough to describe all past and the current hole ice models from both *in-situ* and laboratory measurements. Figure 5.7 shows the acceptance modification as a function of the incident photon angle $\cos(\eta)$. The current baseline model, the variations achieved through modifying p_0 and p_1 , and a laboratory measurement can be seen.

5.5.4 Muon Uncertainties

The muon fraction in the final level selection (see Section 5.4.2) is below 1 %, therefore additional muon systematic uncertainties apart from the spectral index are not implemented, but rather a total muon scaling parameter is added. This total scale is somewhat degenerate with the

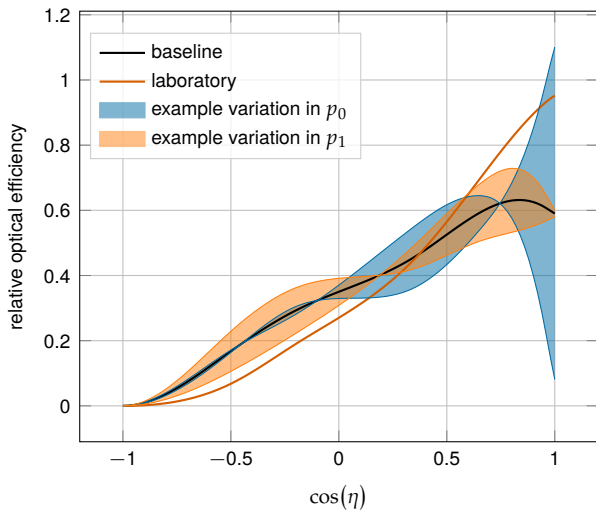


Figure 5.7: Relative angular acceptance modification due to hole ice. Shown is the current baseline model, the variations from changing p_0 and p_1 , and a laboratory measurement. Modified from [67].

DOM efficiency, since an increased DOM efficiency leads to better muon rejection. Both the total muon scaling and the muon spectral index have a very small impact on the analysis as will be shown in Section ??.

cite this?

Detecting Low Energetic Double Cascades

6

6.1 Reconstruction

6.1.1 Table-Based Minimum Likelihood Algorithms

6.1	Reconstruction	53
6.2	Cross Checks	53
6.3	Performance	54

6.1.2 Double Cascade Hypothesis

6.1.3 Modification to Low Energy Events

6.2 Cross Checks

6.2.1 Simplistic Sets

After generation the events are processed with standard Photon, Detector, L1, and L2 processing and then Taupede+MuMillipede is run on top of the L2 files. Multiple versions with different parameters were produced, some with the OscNext baseline parameters, some without detector noise (in Det level) and some with h2-50cm holeice model, to match the holeice model that was used to generate the photonics tables.

BrightDom Cleaning To investigate the effect of the BrightDom cleaning cut the 194601 set without detector noise (and baseline hole ice model) is used. The BrightDom cleaning is needed to stop a few DOMs with many photon hits to drive the reconstruction because this leads to large biases in the energy estimations. Historically, the BrightDom cleaning was removing all DOMs that had a charge larger than 10 times the mean charge. After quickly checking some charge distributions and how the mean behaves it was clear that the cut should better be defined based on a metric that is less affected by outliers, like the median. Figure ?? shows where the mean and the median are located for an example event. The cut was re-defined to use the median instead of the mean and 10% of the simulation were processed with [Taupede](#) using 30x and 100x the median as BrightDom cutoff. Figure ?? shows where these values fall for the same example event.

As a quick check of the performance of both cuts the decay length resolution/bias and the resolutions/biases of all energies were checked. The reconstructed decay length is almost not affected by applying this cut, which is as expected, because it is mostly dependent on the arrival time of the photons. The effect on the reconstructed energy is much stronger, where a looser cut (100x) shows a significantly larger bias than the tighter cut at (30x). Even though this was not a highly sophisticated optimization of the BrightDom cut, an improvement was achieved by changing from mean to median and selecting the tighter cut (of the two tested). It's hard to tell how this would perform for high energy events, but I'm quite certain that a definition based on the median would be more reliable than on the mean.

6.3 Performance

6.3.1 Energy/Decay Length Resolution

6.3.2 Double Cascade Classification

Search for an Excess of Heavy Neutral Lepton Events

7

The measurement performed in this thesis is the search for an excess of HNL events in the 10 years of IceCube DeepCore data. In principle the two physics parameters to be probed are the mass of the HNL, m_4 , and the mixing between the fourth heavy mass state and the SM τ sector, $|U_{\tau 4}|^2$. Since the mass itself influences the production and decay kinematics of the event and the accessible decay modes, individual mass sets were produced as described in Section 4.2. The mass slightly influences the energy distribution, while the mixing both changes the overall scale of the HNL events and the shape in energy and PID. IceCube DeepCore is suited to measure the excess which appears around and below 20 GeV, due to its production from the atmospheric tau neutrinos, although a reduced lower energy threshold could improve the analysis. The measurement will be performed for the three mass sets individually, while the mixing is the parameter that can be varied continuously and will be measured in the fit.

7.1 Final Level Sample

The final level sample of this analysis always consists of the neutrino and muon MC introduced in Section ?? and one of the three HNL samples explained in Section 4.2. All of those simulation sets and the 10 years of IceCube DeepCore data are processed through the full processing and event selection chain described in Section ?? leading to the final level sample. Since applying the last cuts from Section 5.4.2 leaves an insignificant amount of pure noise events in the sample, the noise simulation is not included in the analysis and won't be listed here.

7.1.1 Expected Rates/Events

The rates and the expected number of events for the SM background are shown in Table 7.1. The explicit detector livetime in the 10 years data taking period is 9.28 years. The rates are calculated by summing the weights of all events in the final level sample, while the uncertainties are calculated by taking the square root of the sum of the weights squared. The expected number of events is calculated by multiplying the rate with the livetime. The individual fractions show that this sample is neutrino dominated where the majority of events are ν_μ -CC events.

7.1	Final Level Sample	55
7.2	Statistical Analysis	57
7.3	Analysis Checks	57
7.4	Results	59

add information about the matter profile used

add information about the oscillation probability calculation and the software used for it

Should I adapt the total numbers to match the sum of the rounded individual parts?

Type	Rate [mHz]	Events (in 9.28 years)	Fraction [%]
ν_μ^{CC}	0.3531	103321 ± 113	58.9
ν_e^{CC}	0.1418	41490 ± 69	23.7
ν_{NC}	0.0666	19491 ± 47	11.1
ν_τ^{CC}	0.0345	10094 ± 22	5.8
μ	0.0032	936 ± 15	0.5
total	0.5991	175336 ± 143	100.0

Table 7.1: Final level rates and event expectation of the SM background particle types.

Table 7.2 shows the rates and expected number of events for the HNL signal simulation. The expectation depends on the mass and the mixing and shown here are two example mixings for all the three masses that are being tested in this work. A mixing of 0.0 would result in no HNL events at all. It can already be seen that for the smaller mixing of $|U_{\tau 4}|^2 = 10^{-3}$ the expected number of events is very low, while at the larger mixing of $|U_{\tau 4}|^2 = 10^{-1}$ the number is comparable to the amount of muons in the background sample.

Table 7.2: Final level rates and event expectations of the HNL signal for all three masses and two example mixing values.

HNL mass	Rate [μHz]	Events (in 9.28 years)
$ U_{\tau 4} ^2 = 10^{-1}$		
0.3 GeV	3.3298 ± 0.0053	974.5 ± 1.6
0.6 GeV	3.0583 ± 0.0058	895.0 ± 1.7
1.0 GeV	2.4988 ± 0.0059	731.3 ± 1.7
$ U_{\tau 4} ^2 = 10^{-3}$		
0.3 GeV	0.0057	1.67 ± 0.01
0.6 GeV	0.0220	6.44 ± 0.01
1.0 GeV	0.0248	7.27 ± 0.01

7.1.2 Analysis Binning

[78]: Yu et al. (2023), “Recent neutrino oscillation result with the IceCube experiment”

The identical binning to the analysis performed in [78] is used. It was chosen such that the track-like bin has the largest ν_μ -CC fraction. Extend the binning towards lower energies or increasing the number of bins did not improve the HNL sensitivities significantly. It also has to be considered that sufficient data events need to end up in the individual bins to result in a good fit, which was already investigated in the previous analysis. To mitigate the low data statistics, a few bins were not taken into account in the analysis. There are three bins in PID (cascade-like, mixed and track-like), 12 bins in reconstructed energy, and 8 bins in cosine of the reconstructed zenith angle as specified in Table 7.3. Originally, there were two more bins in $\cos(\theta)$, which were removed to reduce muons coming from the horizon and some low energy bins in the cascade-like bin are removed due to the low event statistics.

- add 3D expectation and/or S/sqrt(B) plots
- Add fractions of the different particle types in the bins for benchmark mass/mixing (another table?)

Table 7.3: Three dimensional binning used in the analysis. All variables are from the FLERCNN reconstruction explained in Section 5.4.

Variable	N_{bins}	Edges	Step
P_ν	3	[0.00, 0.25, 0.55, 1.00]	linear
E	12	[5.00, 100.00]	logarithmic
$\cos(\theta)$	8	[-1.00, 0.04]	linear

7.2 Statistical Analysis

7.2.1 Low Energy Analysis Framework

The analysis is performed using the PISA [93] [94] software framework, which was developed to perform analyses "of small signals in high-statistics neutrino oscillation experiments". It is used to generate the expected event distributions from several MC sets, which can then be compared to the observed data. The expectation for each set is calculated in parallel, applying physics and nuisance parameter effects in a stage-wise manner, before combining the final expectation from all the sets.

[93]: Aartsen et al. (2020), "Computational techniques for the analysis of small signals in high-statistics neutrino oscillation experiments"

7.2.2 Test Statistic

The measurements are performed by comparing the weighted MC to the data. Through variation of the nuisance and physics parameters that govern the weights, the best matching set of parameters can be found. The comparison is done using a modified χ^2 defined as

$$\chi^2_{\text{mod}} = \sum_{i \in \text{bins}} \frac{(N_i^{\text{exp}} - N_i^{\text{obs}})^2}{N_i^{\text{exp}} + (\sigma_i^{\nu})^2 + (\sigma_i^{\mu})^2 + (\sigma_i^{\text{HNL}})^2} + \sum_{j \in \text{syst}} \frac{(s_j - \hat{s}_j)^2}{\sigma_{s_j}^2}, \quad (7.1)$$

as the *test statistic (TS)*. The total even expectation is $N_i^{\text{exp}} = N_i^{\nu} + N_i^{\mu} + N_i^{\text{HNL}}$, where N_i^{ν} , N_i^{μ} , and N_i^{HNL} are the expected number of events in bin i from neutrinos, atmospheric muons, and HNLs, while N_i^{obs} is the observed number of events in bin i . The expected number of events from each particle type is calculated by summing the weights of all events in the bin $N_i^{\text{type}} = \sum_i^{\text{type}} \omega_i$, with the statistical uncertainty being $(\sigma_i^{\text{type}})^2 = \sum_i^{\text{type}} \omega_i^2$. The additional term in Equation 7.1 is included to apply a penalty term for prior knowledge of the systematic uncertainties of the parameters where they are known. s_j are the systematic parameters that are varied in the fit, while \hat{s}_j are their nominal values and σ_{s_j} are the known uncertainties.

Do I want/need to include the description of the KDE muon estimation?

Add table with all systematic uncertainties used in this analysis (in the analysis chapter).

add final level effects of varying the axial mass parameters (or example of one)

add final level effects of varying the DIS parameter (or example of one)

7.2.3 Systematic Uncertainties

7.3 Analysis Checks

Fitting to data will be performed in a *blind* manner, where the analyzer does not immediately see the fitted physics and nuisance parameter values, but first checks that a set of pre-defined *goodness of fit (GOF)* criteria are fulfilled. If those criteria are met to satisfaction the fit results are unblinded and the full result can be revealed. Before these blind fits to data are run, the robustness of the analysis method is tested using pseudo-data that is generated using the MC sets.

7.3.1 Minimization Robustness

1: There is a degeneracy between the lower octant ($\theta_{23} < 45^\circ$) and the upper octant ($\theta_{23} > 45^\circ$), which can lead to TS minima (local and global) at two positions that are mirrored around 45° in θ_{23} .

[95]: Dembinski et al. (2022), *scikit-hep/iminuit*: v2.17.0

[96]: James et al. (1975), “Minuit: A System for Function Minimization and Analysis of the Parameter Errors and Correlations”

Fit	Err.	Prec.	Tol.
Coarse	1e-1	1e-8	1e-1
Fine	1e-5	1e-14	1e-5

Table 7.4: Migrad settings for the two stages in the minimization routine. *Err.* are the step size for the numerical gradient estimation, *Prec.* is the precision with which the LLH is calculated, and *Tol.* is the tolerance for the minimization.

2: A pseudo-data set without statistical fluctuations is called Asimov data set.

Do I want additional plots for this (fit diff, LLH distr, minim. stats, param. fits)?

To find the set of parameters that describes the data best, a staged minimization routine is used. In the first stage, a fit with coarse minimizer settings is performed to find a rough estimate of the *best fit point* (*BFP*). In the second stage, the fit is performed again in both octants¹ of θ_{23} , starting from the BFP of the coarse fit. For each individual fit the *MIGRAD* routine of *iminuit* [95] is used to minimize the χ^2 TS defined in Equation 7.1. *Iminuit* is a fast, python compatible minimizer based on the *MNUTR2* C++ library [96]. The individual minimizer settings are shown in Table 7.4.

To test the minimization routine and to make sure it consistently recovers any injected physics parameters, pseudo-data sets are produced from the MC by choosing the nominal nuisance parameters and specific physics parameters, without adding any statistical or systematic fluctuations to it. These so-called *Asimov*² data sets are then fit back with the full analysis chain. This type of test is called *Asimov inject/recover test*. A set of mixing values between 10^{-3} and 10^0 is injected and fit back. Even though this range is well within the excluded regions by other experiments, discussed in Section 2.2.3, this covers the current sensitive region of the analysis in IceCube DeepCore. Without fluctuations the fit is expected to always recover the injected parameters (both physics and nuisance parameters). The fitted mixing values from the Asimov inject/recover tests are compared to the true injected values in Figure 7.1 for the 0.6 GeV set. As expected, the fit is always able to recover the injected physcis parameter and the nuisance paramters. Additional plots for the other mass sets can be found in Section B.1.

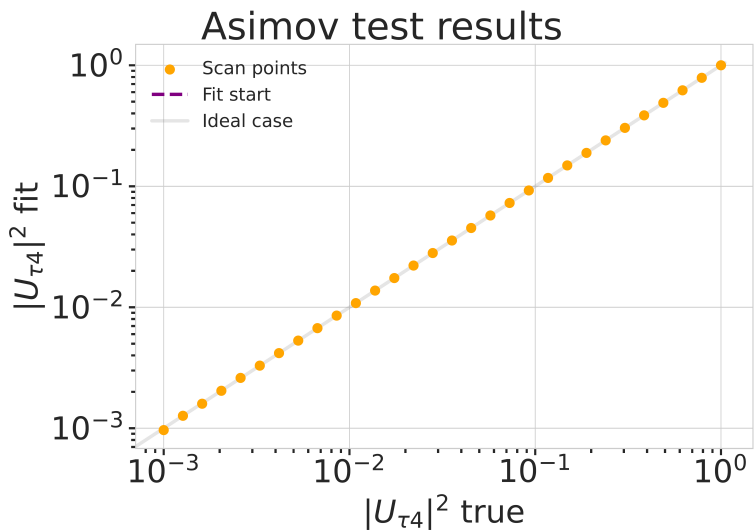


Figure 7.1: Asimov inject/recover test for the 0.6 GeV mass set. Mixing values between 10^{-3} and 10^0 are injected and fit back with the full analysis chain. The injected parameter is always recovered within the statistical uncertainty.

7.3.2 Ensemble Tests

To estimate the goodness of fit, pseudo-data is generated from the MC by injecting the BFP parameters as true parameters and then fluctuating the expected bin counts using Poisson fluctuation. The resulting pseudo-data sets are then fit back with the analysis chain. By comparing the

distribution of TS values from this *ensemble* of pseudo-data trials to the TS of the fit to real data, a p-value can be calculated. The p-value is the probability of finding a TS value at least as large as the one from the data fit. Figure 7.2 shows the TS distribution from the ensemble tests for the 0.6 GeV mass set and the observed TS value from the fit, resulting in a p-value of 28.5 %³. Plots for the addition two mass sets are shown in Section B.1.1.

Add bin-wise TS distribution? Add 3D TS maps?

3: The p-values for the 0.3 GeV and 1.0 GeV are 28.3 % and 26.0 %, respectively.

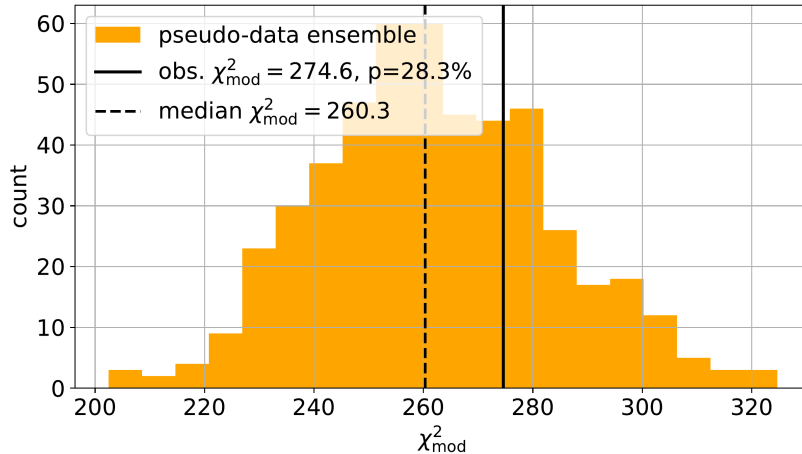


Figure 7.2: Observed fit TS and TS distribution from pseudo-data trials for the 0.6 GeV mass set.

7.4 Results

7.4.1 Best Fit Parameters

7.4.2 Upper Limits

7.4.3 Post-Fit Data/MC Agreement

7.4.4 Likelihood Coverage

8

Summary and Outlook

8.1 Summary

8.1	Summary	61
8.2	Outlook	61

8.1.1 Three-Flavor Oscillation Measurement

8.1.2 Heavy Neutral Lepton Search

Double Cascade Sensitivity

Shape Excess Search

8.2 Outlook

8.2.1 Shape Analysis Improvements

- ▶ estimate full contribution from cascade only events (underestimated due to limited sampling distributions)
- ▶ include double cascade classifier into Binning
- ▶ further optimize binning

8.2.2 Test Coupling to Electron/Muon Flavor

8.2.3 IceCube Upgrade

Conclusion

9

Write conclusion

APPENDIX

A

Heavy Neutral Lepton Signal Simulation

A.1 Model Independent Simulation Distributions

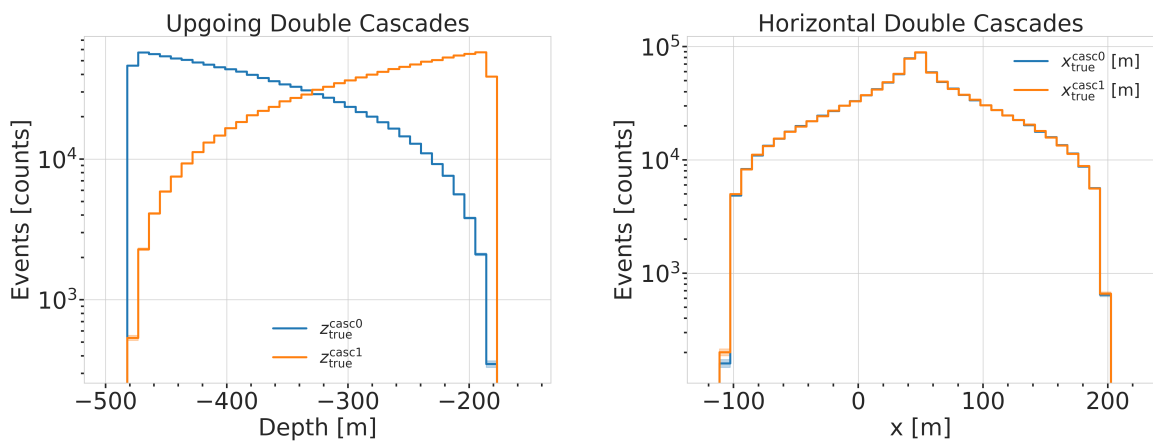


Figure A.1: Generation level distributions of the simplistic simulation sets. Vertical positions (left) and horizontal positions (right) of both sets are shown.

- Re-make plot with x,y for horizontal set one plot!
- Re-make plot with x, y, z for both cascades in one.
- Re-arrange plots in a more sensible way.

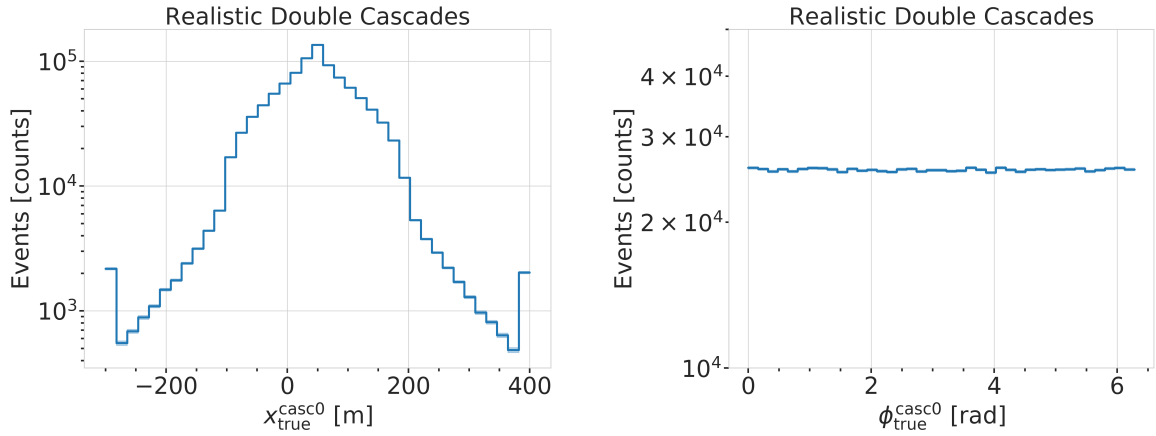


Figure A.2: Generation level distributions of the realistic simulation set. Shown are the cascade x, y, z positions (left) and direction angles (right).

A.2 Model Dependent Simulation Distributions

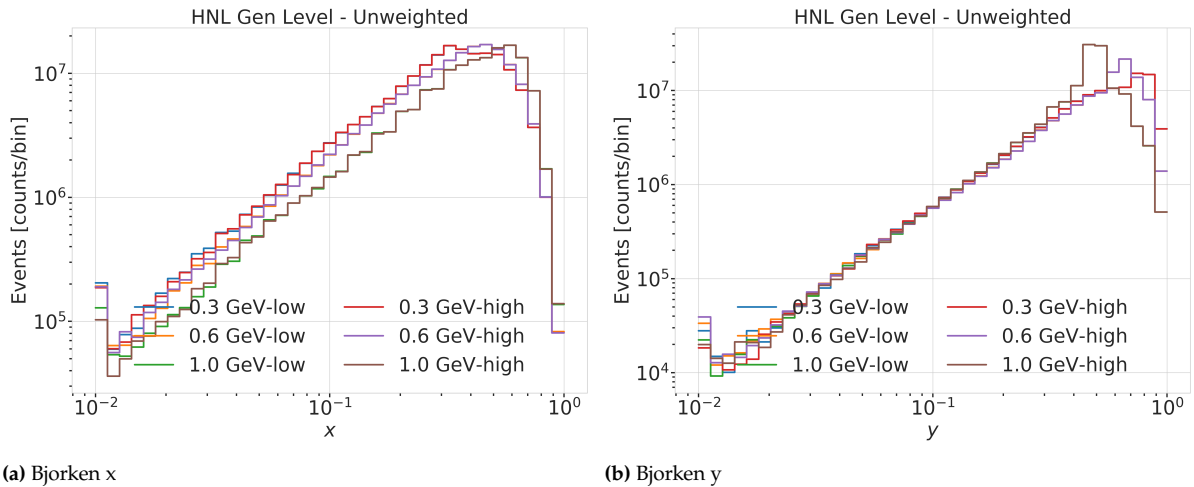


Figure A.3: Generation level distributions of the model dependent simulation.

B

Analysis Checks

B.1 Minimization Robustness

Figure B.1 shows additional Asimov inject/recover tests for the 0.3 GeV and the 1.0 GeV mass sets. The tests were described in Section 7.3.1.

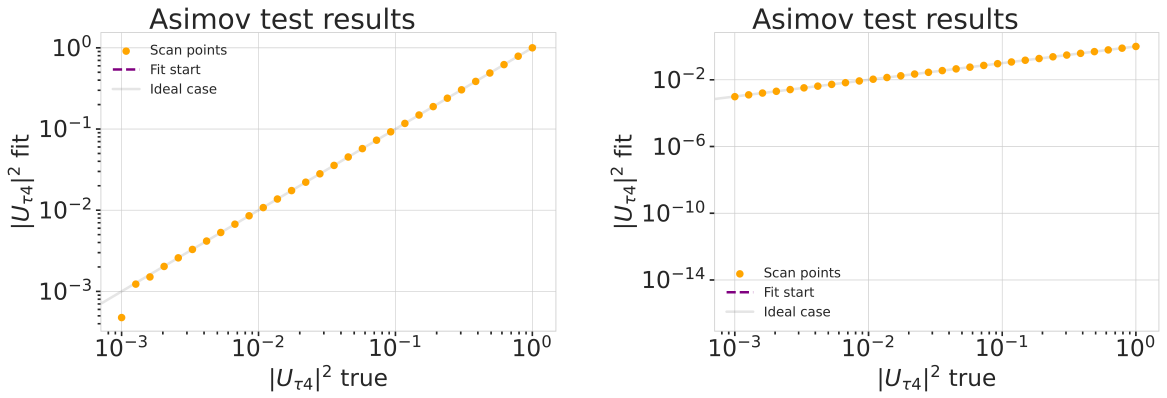


Figure B.1: Asimov inject/recover test for the 0.3 GeV (left) and the 1.0 GeV (right) mass sets. Mixing values between 10^{-3} and 10^0 are injected and fit back with the full analysis chain. The injected parameter is always recovered within the statistical uncertainty.

B.1.1 Ensemble Tests

Figure B.2 shows additional TS distributions from pseudo-data trials and the observed TS from the fit to the data for the ensemble for the 0.3 GeV and the 1.0 GeV mass sets. The tests were described in Section 7.3.2.

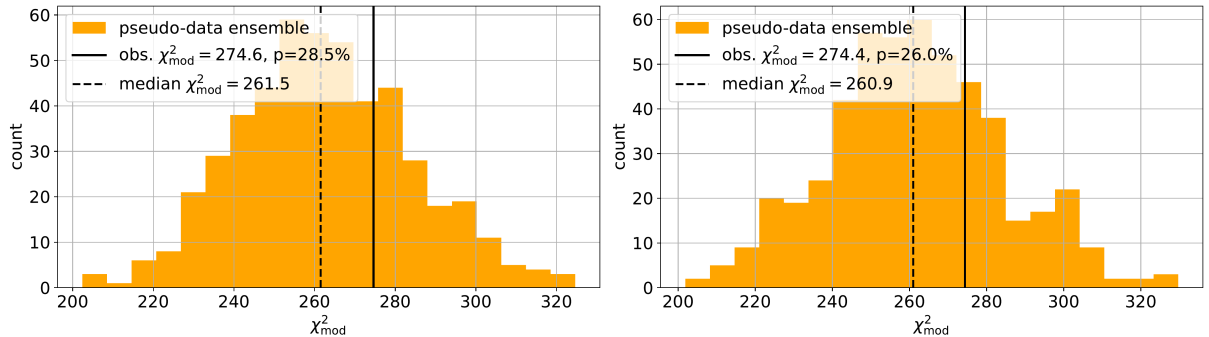


Figure B.2: Observed fit TS and TS distribution from pseudo-data trials for the 0.3 GeV (left) and the 1.0 GeV (right) mass set.

Bibliography

Here are the references in citation order.

- [1] W. Pauli. "Dear radioactive ladies and gentlemen". In: *Phys. Today* 31N9 (1978), p. 27 (cited on page 1).
- [2] C. L. Cowan et al. "Detection of the Free Neutrino: a Confirmation". In: *Science* 124.3212 (1956), pp. 103–104. doi: [10.1126/science.124.3212.103](https://doi.org/10.1126/science.124.3212.103) (cited on page 1).
- [3] G. Danby et al. "Observation of High-Energy Neutrino Reactions and the Existence of Two Kinds of Neutrinos". In: *Phys. Rev. Lett.* 9 (1 July 1962), pp. 36–44. doi: [10.1103/PhysRevLett.9.36](https://doi.org/10.1103/PhysRevLett.9.36) (cited on page 1).
- [4] K. Kodama et al. "Observation of tau neutrino interactions". In: *Physics Letters B* 504.3 (2001), pp. 218–224. doi: [https://doi.org/10.1016/S0370-2693\(01\)00307-0](https://doi.org/10.1016/S0370-2693(01)00307-0) (cited on page 1).
- [5] R. Davis et al. *Proceedings of the Neutrino '72 Europhysics Conference*. Vol. 1. Balatonfured, Hungary, 1972, p. 29 (cited on page 1).
- [6] M. G. Aartsen et al. "The IceCube Neutrino Observatory: instrumentation and online systems". In: *Journal of Instrumentation* 12.3 (Mar. 2017), P03012. doi: [10.1088/1748-0221/12/03/P03012](https://doi.org/10.1088/1748-0221/12/03/P03012) (cited on pages 1, 17, 19, 42).
- [7] C. N. Yang and R. L. Mills. "Conservation of Isotopic Spin and Isotopic Gauge Invariance". In: *Physical Review* 96.1 (Oct. 1954), pp. 191–195. doi: [10.1103/PhysRev.96.191](https://doi.org/10.1103/PhysRev.96.191) (cited on page 3).
- [8] S. Weinberg. "A Model of Leptons". In: *Phys. Rev. Lett.* 19 (21 Nov. 1967), pp. 1264–1266. doi: [10.1103/PhysRevLett.19.1264](https://doi.org/10.1103/PhysRevLett.19.1264) (cited on page 3).
- [9] S. L. Glashow. "Partial-symmetries of weak interactions". In: *Nuclear Physics* 22.4 (Feb. 1961), pp. 579–588. doi: [10.1016/0029-5582\(61\)90469-2](https://doi.org/10.1016/0029-5582(61)90469-2) (cited on page 3).
- [10] R. Jackiw. "Physical Formulations: Elementary Particle Theory. Relativistic Groups and Analyticity. Proceedings of the eighth Nobel Symposium, Aspenäsgården, Lerum, Sweden, May 1968. Nils Svartholm, Ed. Interscience (Wiley), New York, and Almqvist and Wiksell, Stockholm, 1969. 400 pp., illus. \$31.75." In: *Science* 168.3936 (1970), pp. 1196–1197. doi: [10.1126/science.168.3936.1196.b](https://doi.org/10.1126/science.168.3936.1196.b) (cited on page 3).
- [11] P. Higgs. "Broken symmetries, massless particles and gauge fields". In: *Physics Letters* 12.2 (1964), pp. 132–133. doi: [https://doi.org/10.1016/0031-9163\(64\)91136-9](https://doi.org/10.1016/0031-9163(64)91136-9) (cited on page 3).
- [12] M. Gell-Mann. "A Schematic Model of Baryons and Mesons". In: *Resonance* 24 (1964), pp. 923–925 (cited on page 3).
- [13] G. Zweig. "An SU(3) model for strong interaction symmetry and its breaking. Version 2". In: *DEVELOPMENTS IN THE QUARK THEORY OF HADRONS. VOL. 1. 1964 - 1978*. Ed. by D. B. Lichtenberg and S. P. Rosen. Feb. 1964, pp. 22–101 (cited on page 3).
- [14] D. J. Gross and F. Wilczek. "Ultraviolet Behavior of Non-Abelian Gauge Theories". In: *PRL* 30.26 (June 1973), pp. 1343–1346. doi: [10.1103/PhysRevLett.30.1343](https://doi.org/10.1103/PhysRevLett.30.1343) (cited on page 3).
- [15] C. Giunti and C. W. Kim. *Fundamentals of Neutrino Physics and Astrophysics*. Oxford University Press, Mar. 2007 (cited on page 3).
- [16] M. D. Schwartz. *Quantum Field Theory and the Standard Model*. Cambridge University Press, 2013 (cited on page 3).
- [17] A. Terliuk. "Measurement of atmospheric neutrino oscillations and search for sterile neutrino mixing with IceCube DeepCore". PhD thesis. Berlin, Germany: Humboldt-Universität zu Berlin, Mathematisch-Naturwissenschaftliche Fakultät, 2018. doi: [10.18452/19304](https://doi.org/10.18452/19304) (cited on pages 5, 10, 23).

- [18] M. Thomson. *Modern particle physics*. Cambridge [u.a.]: Cambridge University Press, 2013, XVI, 554 S. (Cited on page 5).
- [19] M. Tanabashi et al. "Review of Particle Physics". In: *Phys. Rev. D* 98 (3 Aug. 2018), p. 030001. doi: [10.1103/PhysRevD.98.030001](https://doi.org/10.1103/PhysRevD.98.030001) (cited on pages 6, 8, 11, 22).
- [20] P. Coloma et al. "GeV-scale neutrinos: interactions with mesons and DUNE sensitivity". In: *Eur. Phys. J. C* 81.1 (2021), p. 78. doi: [10.1140/epjc/s10052-021-08861-y](https://doi.org/10.1140/epjc/s10052-021-08861-y) (cited on pages 8, 13, 15, 29, 30, 32).
- [21] M. Honda et al. "Atmospheric neutrino flux calculation using the NRLMSISE-00 atmospheric model". In: *Phys. Rev. D* 92 (2 July 2015), p. 023004. doi: [10.1103/PhysRevD.92.023004](https://doi.org/10.1103/PhysRevD.92.023004) (cited on pages 8, 38).
- [22] A. Fedynitch et al. "Calculation of conventional and prompt lepton fluxes at very high energy". In: *European Physical Journal Web of Conferences*. Vol. 99. European Physical Journal Web of Conferences. Aug. 2015, p. 08001. doi: [10.1051/epjconf/20159908001](https://doi.org/10.1051/epjconf/20159908001) (cited on page 9).
- [23] J. A. Formaggio and G. P. Zeller. "From eV to EeV: Neutrino cross sections across energy scales". In: *Rev. Mod. Phys.* 84 (3 Sept. 2012), pp. 1307–1341. doi: [10.1103/RevModPhys.84.1307](https://doi.org/10.1103/RevModPhys.84.1307) (cited on page 9).
- [24] S. Bilenky and B. Pontecorvo. "Lepton mixing and neutrino oscillations". In: *Physics Reports* 41.4 (1978), pp. 225–261. doi: [10.1016/0370-1573\(78\)90095-9](https://doi.org/10.1016/0370-1573(78)90095-9) (cited on page 11).
- [25] P. A. M. Dirac. "The Quantum Theory of the Emission and Absorption of Radiation". In: *Proceedings of the Royal Society of London Series A* 114.767 (Mar. 1927), pp. 243–265. doi: [10.1098/rspa.1927.0039](https://doi.org/10.1098/rspa.1927.0039) (cited on page 11).
- [26] T. Yanagida. "Horizontal Symmetry and Masses of Neutrinos". In: *Progress of Theoretical Physics* 64.3 (Sept. 1980), pp. 1103–1105. doi: [PTP.64.1103](https://doi.org/10.1103/PTP.64.1103) (cited on page 12).
- [27] P. Astier et al. "Search for heavy neutrinos mixing with tau neutrinos". In: *Phys. Lett. B* 506 (2001), pp. 27–38. doi: [10.1016/S0370-2693\(01\)00362-8](https://doi.org/10.1016/S0370-2693(01)00362-8) (cited on page 12).
- [28] R. Acciari et al. "New Constraints on Tau-Coupled Heavy Neutral Leptons with Masses mN=280–970 MeV". In: *Phys. Rev. Lett.* 127.12 (2021), p. 121801. doi: [10.1103/PhysRevLett.127.121801](https://doi.org/10.1103/PhysRevLett.127.121801) (cited on page 12).
- [29] J. Orloff, A. N. Rozanov, and C. Santoni. "Limits on the mixing of tau neutrino to heavy neutrinos". In: *Phys. Lett. B* 550 (2002), pp. 8–15. doi: [10.1016/S0370-2693\(02\)02769-7](https://doi.org/10.1016/S0370-2693(02)02769-7) (cited on page 12).
- [30] I. Boiarska et al. "Blast from the past: constraints from the CHARM experiment on Heavy Neutral Leptons with tau mixing". In: (July 2021) (cited on page 12).
- [31] P. Abreu et al. "Search for neutral heavy leptons produced in Z decays". In: *Z. Phys. C* 74 (1997). [Erratum: *Z.Phys.C* 75, 580 (1997)], pp. 57–71. doi: [10.1007/s002880050370](https://doi.org/10.1007/s002880050370) (cited on page 12).
- [32] P. Coloma et al. "Double-Cascade Events from New Physics in Icecube". In: *Phys. Rev. Lett.* 119.20 (2017), p. 201804. doi: [10.1103/PhysRevLett.119.201804](https://doi.org/10.1103/PhysRevLett.119.201804) (cited on page 13).
- [33] P. Coloma. "Icecube/DeepCore tests for novel explanations of the MiniBooNE anomaly". In: *Eur. Phys. J. C* 79.9 (2019), p. 748. doi: [10.1140/epjc/s10052-019-7256-8](https://doi.org/10.1140/epjc/s10052-019-7256-8) (cited on page 13).
- [34] P. B. Price, K. Woschnagg, and D. Chirkin. "Age vs depth of glacial ice at South Pole". In: *Geophysical Research Letters* 27.14 (2000), pp. 2129–2132. doi: <https://doi.org/10.1029/2000GL011351> (cited on page 18).
- [35] R. Abbasi et al. "In-situ estimation of ice crystal properties at the South Pole using LED calibration data from the IceCube Neutrino Observatory". In: *The Cryosphere Discussions* 2022 (2022), pp. 1–48. doi: [10.5194/tc-2022-174](https://doi.org/10.5194/tc-2022-174) (cited on page 18).
- [36] R. Abbasi et al. "The IceCube data acquisition system: Signal capture, digitization, and timestamping". In: *Nuclear Instruments and Methods in Physics Research Section A: Accelerators, Spectrometers, Detectors and Associated Equipment* 601.3 (2009), pp. 294–316. doi: <https://doi.org/10.1016/j.nima.2009.01.001> (cited on pages 18, 19, 42).
- [37] M. G. Aartsen et al. "Energy Reconstruction Methods in the IceCube Neutrino Telescope". In: *JINST* 9 (2014), P03009. doi: [10.1088/1748-0221/9/03/P03009](https://doi.org/10.1088/1748-0221/9/03/P03009) (cited on page 19).
- [38] J. Feintzeig. "Searches for Point-like Sources of Astrophysical Neutrinos with the IceCube Neutrino Observatory". PhD thesis. University of Wisconsin, Madison, Jan. 2014 (cited on pages 19, 50).

- [39] N. Kulacz. "In Situ Measurement of the IceCube DOM Efficiency Factor Using Atmospheric Minimum Ionizing Muons". MA thesis. University of Alberta, 2019 (cited on pages 19, 50).
- [40] R. Abbasi et al. "The design and performance of IceCube DeepCore". In: *Astropart. Phys.* 35.10 (2012), pp. 615–624. doi: [10.1016/j.astropartphys.2012.01.004](https://doi.org/10.1016/j.astropartphys.2012.01.004) (cited on pages 19, 42).
- [41] P. A. Cherenkov. "Visible Radiation Produced by Electrons Moving in a Medium with Velocities Exceeding that of Light". In: *Phys. Rev.* 52 (4 Aug. 1937), pp. 378–379. doi: [10.1103/PhysRev.52.378](https://doi.org/10.1103/PhysRev.52.378) (cited on page 20).
- [42] I. Frank and I. Tamm. "Coherent visible radiation from fast electrons passing through matter". In: *C. R. Acad. Sci. USSR* 14 (1937), pp. 109–114 (cited on page 21).
- [43] I. Tamm. "Radiation Emitted by Uniformly Moving Electrons". In: *Selected Papers*. Ed. by B. M. Bolotovskii, V. Y. Frenkel, and R. Peierls. Berlin, Heidelberg: Springer Berlin Heidelberg, 1991, pp. 37–53. doi: [10.1007/978-3-642-74626-0_3](https://doi.org/10.1007/978-3-642-74626-0_3) (cited on page 21).
- [44] L. Rädel and C. Wiebusch. "Calculation of the Cherenkov light yield from low energetic secondary particles accompanying high-energy muons in ice and water with Geant4 simulations". In: *Astroparticle Physics* 38 (Oct. 2012), pp. 53–67. doi: [10.1016/j.astropartphys.2012.09.008](https://doi.org/10.1016/j.astropartphys.2012.09.008) (cited on pages 21, 39).
- [45] D. Chirkin and W. Rhode. "Propagating leptons through matter with Muon Monte Carlo (MMC)". In: (July 2004) (cited on page 21).
- [46] L. Raedel. "Simulation Studies of the Cherenkov Light Yield from Relativistic Particles in High-Energy Neutrino Telescopes with Geant4". MA thesis. Aachen, Germany: Rheinisch-Westfälischen Technischen Hochschule, 2012 (cited on pages 21, 22).
- [47] S. Agostinelli et al. "Geant4—a simulation toolkit". In: *Nucl. Instr. Meth. Phys. Res.* 506.3 (July 2003), pp. 250–303. doi: [10.1016/s0168-9002\(03\)01368-8](https://doi.org/10.1016/s0168-9002(03)01368-8) (cited on pages 22, 39).
- [48] T. Gabriel et al. "Energy dependence of hadronic activity". In: *Nuclear Instruments and Methods in Physics Research Section A: Accelerators, Spectrometers, Detectors and Associated Equipment* 338.2 (1994), pp. 336–347. doi: [https://doi.org/10.1016/0168-9002\(94\)91317-X](https://doi.org/10.1016/0168-9002(94)91317-X) (cited on page 22).
- [49] L. Fischer. https://github.com/LeanderFischer/icetray_double_cascade_generator_functions (cited on page 25).
- [50] R. Abbasi et al. "LeptonInjector and LeptonWeighter: A neutrino event generator and weighter for neutrino observatories". In: *Comput. Phys. Commun.* 266 (2021), p. 108018. doi: [10.1016/j.cpc.2021.108018](https://doi.org/10.1016/j.cpc.2021.108018) (cited on page 28).
- [51] J. Alwall et al. "The automated computation of tree-level and next-to-leading order differential cross sections, and their matching to parton shower simulations". In: *JHEP* 07 (2014), p. 079. doi: [10.1007/JHEP07\(2014\)079](https://doi.org/10.1007/JHEP07(2014)079) (cited on page 29).
- [52] C. Argüelles. <https://github.com/arguelles/NuXSp1Mkr> (cited on page 29).
- [53] J.-M. Levy. "Cross-section and polarization of neutrino-produced tau's made simple". In: *J. Phys. G* 36 (2009), p. 055002. doi: [10.1088/0954-3899/36/5/055002](https://doi.org/10.1088/0954-3899/36/5/055002) (cited on page 30).
- [54] E. Tiesinga et al. "CODATA recommended values of the fundamental physical constants: 2018". In: *Rev. Mod. Phys.* 93 (2 July 2021), p. 025010. doi: [10.1103/RevModPhys.93.025010](https://doi.org/10.1103/RevModPhys.93.025010) (cited on page 31).
- [55] R. Abbasi et al. "Measurement of atmospheric neutrino mixing with improved IceCube DeepCore calibration and data processing". In: *Phys. Rev. D* 108 (1 July 2023), p. 012014. doi: [10.1103/PhysRevD.108.012014](https://doi.org/10.1103/PhysRevD.108.012014) (cited on pages 37, 44, 45, 48, 50).
- [56] C. Andreopoulos et al. "The GENIE Neutrino Monte Carlo Generator: Physics and User Manual". In: (2015) (cited on pages 39, 49).
- [57] M. Glück, E. Reya, and A. Vogt. "Dynamical parton distributions revisited". In: *The European Physical Journal C* 5 (Sept. 1998), pp. 461–470. doi: [10.1007/s100529800978](https://doi.org/10.1007/s100529800978) (cited on page 39).
- [58] A. Bodek and U. K. Yang. "Higher twist, xi(omega) scaling, and effective LO PDFs for lepton scattering in the few GeV region". In: *Journal of Physics G: Nuclear and Particle Physics* 29.8 (2003), p. 1899. doi: [10.1088/0954-3899/29/8/369](https://doi.org/10.1088/0954-3899/29/8/369) (cited on page 39).

- [59] J.-H. Koehne et al. "PROPOSAL: A tool for propagation of charged leptons". In: *Computer Physics Communications* 184.9 (2013), pp. 2070–2090. doi: <https://doi.org/10.1016/j.cpc.2013.04.001> (cited on page 39).
- [60] Y. Becherini et al. "A parameterisation of single and multiple muons in the deep water or ice". In: *Astroparticle Physics* 25.1 (2006), pp. 1–13. doi: <https://doi.org/10.1016/j.astropartphys.2005.10.005> (cited on page 39).
- [61] D. Heck et al. "CORSIKA: A Monte Carlo code to simulate extensive air showers". In: (Feb. 1998) (cited on page 39).
- [62] T. K. Gaisser. "Spectrum of cosmic-ray nucleons, kaon production, and the atmospheric muon charge ratio". In: *Astropart. Phys.* 35 (2012), pp. 801–806. doi: [10.1016/j.astropartphys.2012.02.010](https://doi.org/10.1016/j.astropartphys.2012.02.010) (cited on page 39).
- [63] R. Engel et al. "The hadronic interaction model Sibyll – past, present and future". In: *EPJ Web Conf.* 145 (2017). Ed. by B. Pattison, p. 08001. doi: [10.1051/epjconf/201614508001](https://doi.org/10.1051/epjconf/201614508001) (cited on page 39).
- [64] C. Kopper et al. <https://github.com/claudiok/clsim> (cited on page 40).
- [65] D. Chirkin et al. "Photon Propagation using GPUs by the IceCube Neutrino Observatory". In: *2019 15th International Conference on eScience (eScience)*. 2019, pp. 388–393. doi: [10.1109/eScience.2019.00050](https://doi.org/10.1109/eScience.2019.00050) (cited on page 40).
- [66] M. G. Aartsen et al. "Measurement of South Pole ice transparency with the IceCube LED calibration system". In: *Nucl. Instrum. Meth. A* 711 (2013), pp. 73–89. doi: [10.1016/j.nima.2013.01.054](https://doi.org/10.1016/j.nima.2013.01.054) (cited on page 40).
- [67] A. Trettin. "Search for eV-scale sterile neutrinos with IceCube DeepCore". PhD thesis. Berlin, Germany: Humboldt-Universität zu Berlin, Mathematisch-Naturwissenschaftliche Fakultät, 2023. doi: <https://github.com/atrettin/PhD-Thesis> (cited on pages 40, 41, 51).
- [68] G. Mie. "Beiträge zur Optik trüber Medien, speziell kolloidaler Metallösungen". In: *Annalen der Physik* 330.3 (1908), pp. 377–445. doi: <https://doi.org/10.1002/andp.19083300302> (cited on page 40).
- [69] L. G. Henyey and J. L. Greenstein. "Diffuse radiation in the Galaxy." In: *apj* 93 (Jan. 1941), pp. 70–83. doi: [10.1086/144246](https://doi.org/10.1086/144246) (cited on page 40).
- [70] S. Fiedlschuster. "The Effect of Hole Ice on the Propagation and Detection of Light in IceCube". In: (Apr. 2019) (cited on page 40).
- [71] M. G. Aartsen et al. "In-situ calibration of the single-photoelectron charge response of the IceCube photomultiplier tubes". In: *Journal of Instrumentation* 15.6 (June 2020), P06032. doi: [10.1088/1748-0221/15/06/P06032](https://doi.org/10.1088/1748-0221/15/06/P06032) (cited on page 41).
- [72] M. Larson. "Simulation and Identification of Non-Poissonian Noise Triggers in the IceCube Neutrino Detector". Available at <https://ir.ua.edu/handle/123456789/1927>. MA thesis. University of Alabama, Tuscaloosa, AL, USA, 2013 (cited on page 41).
- [73] M. Larson. "A Search for Tau Neutrino Appearance with IceCube-DeepCore". available at https://discoverycenter.nbi.ku.dk/teaching/thesis_page/mjlarson_thesis.pdf. PhD thesis. University of Copenhagen, Denmark, 2018 (cited on page 41).
- [74] E. Lohfink. "Testing nonstandard neutrino interaction parameters with IceCube-DeepCore". PhD thesis. Mainz, Germany: Johannes Gutenberg-Universität Mainz, Fachbereich für Physik, Mathematik und Informatik, 2023. doi: <http://doi.org/10.25358/openscience-9288> (cited on page 41).
- [75] M. G. Aartsen et al. "The IceCube Neutrino Observatory: Instrumentation and Online Systems". In: *JINST* 12.03 (2017), P03012. doi: [10.1088/1748-0221/12/03/P03012](https://doi.org/10.1088/1748-0221/12/03/P03012) (cited on page 42).
- [76] J. H. Friedman. "Stochastic gradient boosting". In: *Computational Statistics & Data Analysis* 38 (2002), pp. 367–378 (cited on page 43).
- [77] R. Abbasi et al. "Low energy event reconstruction in IceCube DeepCore". In: *Eur. Phys. J. C* 82.9 (2022), p. 807. doi: [10.1140/epjc/s10052-022-10721-2](https://doi.org/10.1140/epjc/s10052-022-10721-2) (cited on page 45).

- [78] S. Yu and J. Micallef. "Recent neutrino oscillation result with the IceCube experiment". In: *38th International Cosmic Ray Conference*. July 2023 (cited on pages 45, 56).
- [79] S. Yu and on behalf of the IceCube collaboration. "Direction reconstruction using a CNN for GeV-scale neutrinos in IceCube". In: *Journal of Instrumentation* 16.11 (2021), p. C11001. doi: [10.1088/1748-0221/16/11/C11001](https://doi.org/10.1088/1748-0221/16/11/C11001) (cited on pages 45, 46).
- [80] J. Micallef. <https://github.com/jessimic/LowEnergyNeuralNetwork> (cited on page 45).
- [81] M. Huennefeld. "Deep Learning in Physics exemplified by the Reconstruction of Muon-Neutrino Events in IceCube". In: *PoS ICRC2017* (2017), p. 1057. doi: [10.22323/1.301.1057](https://doi.org/10.22323/1.301.1057) (cited on page 45).
- [82] H. Dembinski et al. "Data-driven model of the cosmic-ray flux and mass composition from 10 GeV to 10^{11} GeV". In: *PoS ICRC2017* (2017), p. 533. doi: [10.22323/1.301.0533](https://doi.org/10.22323/1.301.0533) (cited on page 48).
- [83] G. D. Barr et al. "Uncertainties in atmospheric neutrino fluxes". In: *Phys. Rev. D* 74 (9 Nov. 2006), p. 094009. doi: [10.1103/PhysRevD.74.094009](https://doi.org/10.1103/PhysRevD.74.094009) (cited on page 48).
- [84] J. Evans et al. "Uncertainties in atmospheric muon-neutrino fluxes arising from cosmic-ray primaries". In: *Phys. Rev. D* 95 (2 Jan. 2017), p. 023012. doi: [10.1103/PhysRevD.95.023012](https://doi.org/10.1103/PhysRevD.95.023012) (cited on page 48).
- [85] A. Fedynitch et al. <https://github.com/afedynitch/MCEq> (cited on page 48).
- [86] G. D. Barr et al. "Uncertainties in Atmospheric Neutrino Fluxes". In: *Phys. Rev. D* 74 (2006), p. 094009. doi: [10.1103/PhysRevD.74.094009](https://doi.org/10.1103/PhysRevD.74.094009) (cited on page 48).
- [87] F. Riehn et al. "Hadronic interaction model sibyll 2.3d and extensive air showers". In: *Phys. Rev. D* 102 (6 Sept. 2020), p. 063002. doi: [10.1103/PhysRevD.102.063002](https://doi.org/10.1103/PhysRevD.102.063002) (cited on page 48).
- [88] A. Cooper-Sarkar, P. Mertsch, and S. Sarkar. "The high energy neutrino cross-section in the Standard Model and its uncertainty". In: *JHEP* 08 (2011), p. 042. doi: [10.1007/JHEP08\(2011\)042](https://doi.org/10.1007/JHEP08(2011)042) (cited on page 49).
- [89] Q. Wu et al. "A precise measurement of the muon neutrino–nucleon inclusive charged current cross section off an isoscalar target in the energy range $2.5 < E < 40$ GeV by NOMAD". In: *Physics Letters B* 660.1 (2008), pp. 19–25. doi: <https://doi.org/10.1016/j.physletb.2007.12.027> (cited on page 50).
- [90] M. M. Tzanov. "Precise measurement of neutrino and anti-neutrino differential cross sections on iron". PhD thesis. University of Pittsburgh, Pennsylvania, Jan. 2005 (cited on page 50).
- [91] W. G. Seligman. "A next-to-leading-order QCD analysis of neutrino-iron structure functions at the Tevatron". PhD thesis. Columbia University, New York, Aug. 1997 (cited on page 50).
- [92] Rongen, Martin. "Measuring the optical properties of IceCube drill holes". In: *EPJ Web of Conferences* 116 (2016), p. 06011. doi: [10.1051/epjconf/201611606011](https://doi.org/10.1051/epjconf/201611606011) (cited on page 50).
- [93] M. G. Aartsen et al. "Computational techniques for the analysis of small signals in high-statistics neutrino oscillation experiments". In: *Nucl. Instrum. Meth. A* 977 (2020), p. 164332. doi: [10.1016/j.nima.2020.164332](https://doi.org/10.1016/j.nima.2020.164332) (cited on page 57).
- [94] I. Collaboration. <https://github.com/icecube/pisa> (cited on page 57).
- [95] H. Dembinski et al. *scikit-hep/minuit: v2.17.0*. Version v2.17.0. Sept. 2022. doi: [10.5281/zenodo.7115916](https://doi.org/10.5281/zenodo.7115916) (cited on page 58).
- [96] F. James and M. Roos. "Minuit: A System for Function Minimization and Analysis of the Parameter Errors and Correlations". In: *Comput. Phys. Commun.* 10 (1975), pp. 343–367. doi: [10.1016/0010-4655\(75\)90039-9](https://doi.org/10.1016/0010-4655(75)90039-9) (cited on page 58).